Reducing Computational Costs for Many-Body Physics Problems

Thesis by
Erika Ye

In Partial Fulfillment of the Requirements for the
Degree of
Doctor of Philosophy

CALIFORNIA INSTITUTE OF TECHNOLOGY
Pasadena, California

2021
Defended March 22, 2021

ACKNOWLEDGEMENTS

I would like to thank my advisors Garnet Chan and Austin Minnich for their time and support throughout my time here at Caltech. While my path has been non-linear, to say the least, I am thankful for their patience and guidance as I grew as a researcher and a scientist.

To my family, friends, lab mates, and the Caltech Frisbee team: thanks for helping me keep my sanity over the years.

ABSTRACT

Three different computational physics problems are discussed. The first project is solving the semi-classical Boltzmann transport equation (BTE) to compute the thermal conductivity of 1-D superlattices. We consider various spectral scattering models at each interface. This computation requires the inversion of a matrix whose size scales with the number of points used in the discretization of the Brillouin zone. We use spatial symmetries to reduce the size of data points and make the computation manageable. The other two projects involve quantum systems. Simulating quantum systems can potentially require exponential resources because of the exponential scaling of Hilbert space with system size. However, it has been observed that many physical systems, which typically exhibit locality in space or time, require much fewer resources to accurately simulate within some small error tolerance. The second project in the thesis is a two-step factorization of the electronic structure Hamiltonian that allows for efficient implementation on a quantum computer and also systematic truncation of small contributions. By using truncations that only incur errors below chemical accuracy, one is able to reduce the number of terms in the Hamiltonian from $O(N^4)$ to $O(N^3)$, where N is the number of molecular orbitals in the system. The third project is a tensor network algorithm based on the concept of influence functionals (IFs) to compute long-time dynamics of single-site observables. IFs are high-dimensional objects that describe the influence of the bath on the dynamics of the subsystem of interest over all times, and we are interested in their low-rank approximations. We study two numerical models, the spin-boson model and a model of interacting hard-core bosons in a 1D harmonic trap, and find that the IFs can be efficiently computed and represented using tensor network methods. Consistent with physical intuition, the correlations in the IFs appear to decrease with increased bath sizes, suggesting that the low-rank nature of the IF is due to nontrivial cancellations in the bath.

PUBLISHED CONTENT AND CONTRIBUTIONS

[1] M. Motta, E. Ye, J. McClean, Z. Li, A. J. Minnich, R. Babbush, and G. K.-L. Chan, “Low rank representations for quantum simulation of electronic structure,” arXiv preprint comp-ph/1808.02625 (2018),
E.Y. contributed to the numerical analysis and gates counts for the electronic structure calculations.

[2] E. Ye and A. J. Minnich, “Ab initio based investigation of thermal transport in superlattices using the Boltzmann equation: Assessing the role of phonon coherence,” J. Appl. Phys. **125**, 055107 (2019),
E.Y. contributed to all parts of the project.

[3] E. Ye and G. K.-L. Chan, “Constructing tensor network influence functionals for general quantum dynamics,” arXiv preprint quant-ph/2101.05466 (2021),
E.Y. contributed to all parts of the project.

TABLE OF CONTENTS

LIST OF ILLUSTRATIONS

Chapter 1

INTRODUCTION

Computers have provided scientists with incredible insight into a variety of problems. However, while computers are becoming ever more powerful, their resources are not infinite (and neither is the amount of time we are willing to wait for), so physicists cannot blindly task them with arbitrarily large or complex problems. Rather, one must find ways to effectively reduce the problem to be more manageable. In this thesis, we consider three different computational physics problems introduced below. Due to the disparate nature of the topics in this thesis, the bulk of the necessary background will be included within each topical chapter.

1.1 Cross-plane Thermal Conductivity of 1-D Superlattices

The first topical chapter will discuss solving the colored Boltzmann transport equation (BTE) for 1-D superlattices to verify that recent experimental observations of a thermal conductivity minimum with respect to superlattice period at room temperature [1] cannot be explained using the particle description of phonons.

1-D superlattices are heterostructures consisting of many layers of different materials stacked upon each other in a periodic fashion. The simplest example is one with alternating layers of two different materials. To compute its thermal conductivity, one needs to consider the different phonon band structures of the materials (and the resulting different phonon transport properties), as well as interfaces in between the layers whose transmission properties depend not only on the adjacent materials but also on the quality of the interface.

One goal for computing the thermal conductivity of such structures is to find ultra-low thermal conductivity materials for thermoelectric devices. Prior experimental works have observed that the thermal conductivity can be reduced significantly by using nanostructures and and nanocomposities, due to the increased boundary scattering. Thus, studying a simple system to understand the physics and developing a predictive model to compute its thermal conductivity can aid in the search for even lower thermal conductivity materials.

However, it is unclear how to best approach the problem while obtaining accurate results. For example, nanoscale features would suggest that wave-like properties of phonons are important. On the other hand, heat transfer is typically associated with higher frequency phonons that scatter quickly and are often described as particles.

In this work, we consider a semi-classical approach, and compute the thermal conductivity using the Boltzmann transport equation (which treats phonons classically as particles) but use phonon properties obtained from ab initio methods without any averaging.

The Boltzmann transport equation describes the time evolution of local populations of a particular phonon mode, which are subject to diffusion and decays with some lifetime due to scattering off other phonons. However, because of energy conservation, the populations of all phonon modes are related to each other, and the BTE for phonon transport can be interpreted as a series of coupled differential equations. Computing the local phonon populations requires knowing the local temperature, which requires solving an integral equation involving all phonon modes. Previously, solving the BTE to compute cross-plane thermal conductivities of 1-D superlattices has typically required using various simplifying assumptions such as the gray approximation, in which one assumes that all phonons have the same lifetime or mean free path (MFP) [2, 3]. The problem can be simplified further by assuming the layer thickness is much smaller than the chosen MFP, resulting in ballistic cross-plane heat transport. However, recently, Hua et al. described how to compute the cross-plane thermal conductivity across a thin slab of arbitrary thickness, while also using ab-initio phonon properties [4]. We expand on this work to compute thermal conductivities of 1-D superlattices with spectral interface scattering models.

We find that the BTE can predict a minimum thermal conductivity plateau with respect to varied superlattice period, but it cannot predict the non-monotonic behavior observed in recent experiments. This is consistent with the classical interpretation that interfaces act as thermal resistors, but we highlight that some phonons may experience no resistance when passing through the interfaces, resulting in a reduced but finite thermal conductivity. In contrast, lattice dynamical models predict that there can be increase in thermal conductivity at even smaller superlattice periods after reaching a minimum [5]. This suggests that the observed minimum in thermal conductivity with respect to superlattice period is indicative of the crossover in the phonon's wave and particle behavior.

1.2 Low-rank Representation of the Electronic Structure Hamiltonian

The second chapter will present work done with others on approximating the electronic structure Hamiltonian to reduce costs of quantum chemistry algorithms on quantum computers. Quantum computation relies on performing operations on N qubits (quantum bits) that can be entangled with each other and thus can represent any state in the 2^N-dimensional Hilbert space. (In contrast, N classical bits can only represent states along the axes of the space.) Thus, it is believed that there exist problems for which quantum computers can provide exponential speed-ups over their classical counterparts.

However, quantum computers are fundamentally sensitive to noise and limited by decoherence times (they lose their information through coupling to the environment). To counter the issue of noise, error-correction and fault-tolerant schemes have been developed. However, such schemes require orders of magnitude more qubits, larger connectivities, and even lower noise rates than are available on current devices (though the hardware is continuing to improve). Despite that, there has been a push to look for near-term applications of these noisy, intermediate scale quantum (NISQ) computers.

Quantum chemistry is one potential application for NISQ devices. Here, we are interested in finding an efficient implementation of a single Trotter step of the electronic structure Hamiltonian, as well as the unitary coupled cluster operator (with single and doubles excitations). Both of these operators only include up to 2-electron interactions. The Trotter step operation appears when evolving the system in time, and as a potential ansatz for the variational quantum eigensolver method. While these Trotter steps can be broken down into a polynomial ($O(N^4)$) number of gates, where N is the number of orbitals in the chemical system, the actual implementation of the gate is difficult because the active operators are not necessarily acting on neighboring qubits (which is a problem for most NISQ devices which only exhibit nearest neighbor connectivities), and requires operating on many qubits at once (potentially exacerbated if the fermionic anticommutation relations are not encoded in the prepared quantum state and instead must be included via Jordan-Wigner strings).

We present a decomposition that writes the 2-electron quantum chemistry operators in second quantization as a series of basis rotations, one-body operators, and diagonal two-body operators, thus allowing it to be efficiently implemented on a quantum computer with only linear connectivity. Additionally, the decomposition allows one to systematically truncate less important terms. For the chemical systems, which exhibit spatial locality, the number of terms in the sum is reduced from $O(N^4)$ to $O(N^3)$. The utility of this low-rank decomposition can be realized in a variety of quantum algorithms, ranging from the intended near-terms algorithms to fault-tolerant schemes (qubitization [6, 7]) to state measurement [8, 9], and even classical algorithms such as quantum Monte Carlo [10].

1.3 Long-time Dynamics Using Tensor Networks

The third and last chapter will present a tensor network algorithm to compute long-time dynamics of single-site observables (or dynamical correlation functions, if desired) for general (1-D) quantum systems. Our proposed algorithm is inspired by influence functionals.

The tensor network formalism uses a network of high-dimensional tensors to efficiently represent quantum many-body systems by exploiting the low-rank properties that arise if correlations are predominantly local. 1-D tensor networks (Matrix Product States) have seen widespread use in a variety of quantum physics and chemistry problems. However, it is known that tensor networks can only efficiently represent states with relatively low entanglement. Thus, while tensor networks are suitable for finding and representing ground states and even low-lying excited states, they tend to face difficulties when representing time-evolved states, particularly those far-from-equilibrium. An introduction to tensor networks is provided in the Appendix.

Influence functionals are high-dimensional objects that describe the influence of the bath on the dynamics of the subsystem of interest as a function of time. Prior work on the influence functional is largely limited to harmonic baths with linear coupling, for which the exact analytical solution is known [11, 12]. However, the influence functional is expected to generally be relatively low-rank (ie. compressible) if the system exhibits time locality, the property that the dynamics is more strongly affected by the state at recent times than the state at much earlier times, as is the case in thermalizing dynamics. As such, 1-D tensor networks may be able to efficiently represent the influence functional, as several recent works have pointed out [13–19]. However, all existing methods either assume that the system has some particular structure (such as linear coupling to a harmonic bath, a star geometry, or a 1-D geometry with translational invariance), or they depend on learning the influence functional from the observed subsystem dynamics.

We present an algorithm to efficiently compute and represent influence functionals for arbitrary 1-D quantum systems. We benchmark our algorithm using the spin-boson model and also investigate a hardcore-boson model with nearest neighbor interactions and a harmonic trap. We find that our proposed algorithm can compete with or outperform traditional time evolution methods for large systems. We also measure time-like entanglement in the influence functionals and find that it is more compressible with increased bath size, consistent with physical intuition, suggesting that the compressibility of the influence functional arises from non-trivial cancellations in the bath that correspond to information dissipation.

References

[1] J. Ravichandran, A. K. Yadav, R. Cheaito, P. B. Rossen, A. Soukiassian, S. J. Suresha, J. C. Duda, B. M. Foley, C.-H. Lee, Y. Zhu, A. W. Lichtenberger, J. E. Moore, D. A. Muller, D. G. Schlom, P. E. Hopkins, A. Majumdar, R. Ramesh, and M. A. Zurbuchen, "Crossover from incoherent to coherent phonon scattering in epitaxial oxide superlattices," Nature Mater. **13**, 168–172 (2014).

[2] G. Chen, "Thermal conductivity and ballistic-phonon transport in superlattices," Appl. Phys. Lett. **71**, 2761 (1997).

[3] G. Chen, "Thermal conductivity and ballistic-phonon transport in the cross-plane direction of superlattices," Phys. Rev. B **57**, 14958 (1998).

[4] C. Hua and A. J. Minnich, "Semi-analytical solution to the frequency-dependent boltzmann transport equation for cross-plane heat conduction in thin films," J. Appl. Phys. **117**, 175306 (2015).

[5] M. V. Simkin and G. D. Mahan, "Minimum thermal conductivity of superlattices," Phys. Rev. Lett. **84**, 927–930 (2000).

[6] D. W. Berry, C. Gidney, M. Motta, J. R. McClean, and R. Babbush, "Qubitization of arbitrary basis quantum chemistry leveraging sparsity and low rank factorization," Quantum **3**, 208 (2019).

[7] V. von Burg, G. H. Low, T. Häner, D. S. Steiger, M. Reiher, M. Roetteler, and M. Troyer, "Quantum computing enhanced computational catalysis," arXiv preprint quant-ph/2007.14460 (2020).

[8] W. J. Huggins, J. McClean, N. Rubin, Z. Jiang, N. Wiebe, K. B. Whaley, and R. Babbush, "Efficient and noise resilient measurements for quantum chemistry on near-term quantum computers," arXiv quant-ph , 1907.13117 (2020).

[9] T.-C. Yen and A. F. Izmaylov, "Cartan sub-algebra approach to efficient measurements of quantum observables," arXiv preprint quant-ph/2007.01234 (2020).

[10] M. Motta, J. Shee, S. Zhang, and G. K.-L. Chan, "Efficient ab initio auxiliary-field quantum Monte Carlo calculations in Gaussian bases via low-rank tensor decomposition," Journal of Chemical Theory and Computation (2019).

[11] R. P. Feynman, "Space-time approach to non-relativistic quantum mechanics," Rev. Mod. Phys. **20**, 367–387 (1948).

[12] R. P. Feynman and F. L. Vernon, "The theory of a general quantum system interacting with a linear dissipative system," Annals Phys. **24**, 118–173 (1963).

[13] A. Strathearn, P. Kirton, D. Kilda, J. Keeling, and B. W. Lovett, "Efficient non-Markovian quantum dynamics using time-evolving matrix product operators," Nature Communications **9**, 3322 (2018).

[14] M. R. Jorgensen and F. A. Pollock, "Exploiting the causal tensor network structure of quantum processes to efficiently simulate non-Markovian path integrals," Phys. Rev. Lett. **123**, 240602 (2019).

[15] A. Lerose, M. Sonner, and D. A. Abanin, "Influence matrix approach to many-body Floquet dynamics," arXiv cond-mat , 2009.10105 (2020).

[16] M. Cygorek, M. Cosacchi, A. Vagov, V. M. Axt, B. W. Lovett, J. Keeling, and E. M. Gauger, "Numerically-exact simulations of arbitrary open quantum systems using automated compression of environments," arXiv quant-ph , 2101.01653 (2021).

[17] I. A. Luchnikov, S. V. Vintskevich, H. Ouerdane, and S. N. Filippov, "Simulation complexity of open quantum dynamics: Connections with tensor networks," Phys. Rev. Lett. **122**, 160401 (2019).

[18] F. A. Pollock, C. Rodriguez-Rosario, T. Frauenheim, M. Paternostro, and K. Modi, "Non-Markovian processes: Complete framework and efficient characterization," Phys. Rev. A **97**, 012127 (2018).

[19] I. A. Luchnikov, S. V. Vintskevich, D. A. Grigoriev, and S. N. Filippov, "Machine learning non-Markovian dynamics," Phys. Rev. Lett. **124**, 140502 (2020).

Chapter 2

THERMAL TRANSPORT IN 1-D SUPERLATTICES VIA THE BOLTZMANN TRANSPORT EQUATION

In this work, we investigate the thermal conductivity of 1-D superlattices in the incoherent scattering limit using the Boltzmann transport equation (BTE) under the relaxation time approximation (RTA). The ab-initio phonon dispersions and lifetimes of each superlattice layer provided to us is obtained from density functional perturbation theory (DFPT) calculations on the bulk material [1, 2]. Reflection and transmission coefficients at the interfaces are modeled based on angle of incidence, phonon frequency, and specularity one might expect given an interface roughness. We find that the BTE, and thus incoherent phonon scattering, is unable to recreate experimentally observed trends of non-monotonic behavior of thermal conductivity with respect to superlattice period.

The expensive step of the calculation is the inversion of a matrix that scales in size with respect to the number of phonon modes needed to accurately represent the material's phonon band structure. We utilize symmetries to reduce the size of this matrix to make our calculations manageable.

The work presented in this chapter is adapted from

E. Ye and A. J. Minnich "Ab-initio based investigation of thermal transport in superlattices using the Boltzmann equation: Assessing the role of phonon coherence," J. Appl. Phys. **125**, 055107 (2019). DOI: `10.1063/1.5075481`.

We thank Dr. Lucas Lindsay for providing the ab initio phonon dispersions and scattering lifetime data for crystalline silicon, which can be found in the appendix of Ref. [2].

2.1 Introduction

The thermal properties of crystalline solids are determined by atomistic matter waves, dubbed phonons, that can propagate through the material. The phonon dispersion of the material describes how the phonon frequency is related to its direction of propagation in the crystal, and is determined by the crystal structure and the harmonic force constants between the atoms. These relations provide most of the information required to describe the thermal properties of the materials, except for the scattering rates of the different phonons. In a defect-less crystal, the scattering is dominated by phonon-phonon scattering, which can be computed approximately from third-order anharmonic interatomic force constants. These force constants can be determined using ab initio methods such as density functional perturbation theory, assuming some interaction potential between the atoms [1, 3].

In reality, extrinsic scattering mechanisms, such as scattering at crystal grain boundaries and atomic defects, also play a role in a material's thermal conducting. This provides a means for one to engineer a material's thermal transport properties. For example, several reviews discuss the potential of using nanostructures or nanocomposites for thermoelectric devices, since they exhibit low thermal conductivity due to the increased boundary scattering [4–7].

Alternatively, since phonons are lattice waves, one can potentially alter a material's phonon dispersion by introducing an artificial periodicity. (This idea is analogous to the theory behind photonic crystals, in which an artificial periodicity is used to alter a material's optical dispersion.) The simplest example of such a structure is a 1-D binary superlattice (SL), which is constructed from two distinct layers placed one after another in an alternating fashion. There exist several works on acoustic metamaterials [8–10] and phononic crystals for phonons with frequencies of a few hundred gigahertz [11–14]. However, it was unclear if such techniques would still remain relevant at room temperature, where higher frequency phonons (within the terahertz range) start to exist with increased probability. It is expected that these phonons are more prone to extrinsic scattering effects due to their shorter wavelengths and they tend to exhibit shorter mean free paths (the expected distance a phonon travels before scattering). Thus, these phonons may decohere too quickly for wave behavior to affect macroscopic thermal transport behaviors.

Within the past decade, due to improved fabrication and growth techniques, many experimental works investigated the thermal conductivity of 1-D binary superlattices (SLs) with layers only a few nanometers thick, in an attempt to observe the crossover between regimes where either wave-like or particle-like properties of phonons are dominant [15–21]. One indicator, proposed by Simkin and Mahan, is the existence of a minimum with respect to superlattice period [22]. Clear proof of the existence of the minimum was elusive until recently clearly observed in metal/semiconductor nitride superlattices [16] and perovskite superlattices [17].

There also have been a host of computational investigations to understand phonon transport in superlattices, performed using a variety of computational methods such as density functional perturbation theory (DFPT) [23, 24], atomistic Green's functions (AGF) [21, 25, 26], or molecular dynamics (MD) [27–33], However, the conclusions of what systems exhibit a thermal conductivity minimum are varied and sometimes appear to be contradictory. For example, Garg et al. found that DFPT predicts a decrease in thermal conductivity for increasing SL period for Si/Ge structures. This is contradictory to classical intuition as well as MD calculations. In order to capture the expected trend of increasing thermal conductivity with increasing SL period, additional scattering from imperfect interfaces (eg. interfaces with surface roughness) must be included [23]. In contrast, Frieling et al. and Chen et al. used molecular dynamics and find that smooth interfaces are required to observe a minimum [27, 29].

However, it has never been verified that the Boltzmann transport equation (BTE), which by construction describes phonons as particles, cannot realize a thermal conductivity minimum in 1-D superlattices with respect to superlattice period. This is largely because the BTE is an integro-differential equation that couples together all phonon modes, and the cross-plane conductivity of SLs is expensive to compute exactly. In previous works, the BTE is solved using a gray approximation, in which one fixes some parameter (usually the mean free path or relaxation time) over all phonon frequencies [34–38]. However, phonons of different frequencies can have significantly different mean free paths and can also exhibit very different scattering behaviors at each interface. It has been shown that the gray model yields inaccurate results compared to calculations incorporating spectral phonon properties [39, 40]. This is exacerbated when the cross-plane thickness of the system of interest is on the order of the mean free paths, and some modes exhibit ballistic transport while others exhibit diffusive transport. Hua et al. proposed a solution to the BTE based on a cosine expansion integration scheme, which allows one to efficiently compute the cross-plane thermal conductivity of slabs of arbitrary thickness without using the gray approximation [41]. In this work, we expand on their work and solve the BTE to compute the thermal conductivities of 1-D superlattices with minimal approximations, and verify that the thermal conductivity minimum cannot be obtained in the incoherent particle picture.

This chapter is organized as follows. First will be a review of the Boltzmann transport equation for cross-plane phonon transport and its solution. Then will be a short discussion of existing literature for computing the thermal conductivity of

1-D superlattices. Afterwards, we introduce our algorithm for solving the thermal conductivity for 1-D superlattices while incorporating spectral phonon properties and considering more general interfaces. We present our results for thermal conductivities with respect to superlattice period and temperature for various toy models.

2.2 Review of Phonon Band Structure in Crystals

In the following section, we will review the derivation of a crystal's phonon band structure from lattice harmonics. More in depth discussions can be found in many textbooks such as Chapter 4 (Phonons 1. Crystal Vibrations) of Kittel [42].

Consider a 1-D chain of atoms with lattice spacing a. We assume a harmonic energy potential V between two neighboring atoms, meaning that the energy is quadratic in the relative displacement of an atoms with its neighbors. Neglecting higher order terms in the energy potential is valid for small relative displacements. This statement is equivalent to assuming that the forces acting on the atoms is linear in the deviations of the spacing from their neighbors from a, and that the total force on atom s can be obtained from Hooke's law as

$$F_s = C(u_{s+1} - u_s) + C(u_{s-1} - u_s)$$

where C is the force constant and u_i is the displacement of the ith atom from its equilibrium position.

The equation of motion for atom s is thus

$$m\frac{d^2u_s}{dt^2} = C(u_{s+1} + u_{s-1} - 2u_s)$$

where m is the mass of the atom.

Assuming time-harmonic solutions such that the solution for u has a time dependence $\exp(-i\omega t)$, then

$$-m\omega^2 u_s = C(u_{s+1} + u_{s-1} - 2u_s) \ .$$

Then, assuming that u has the form $u_s = u\exp(iska)$, where k is the wavevector, we arrive at the **dispersion relation** $\omega(k)$ for a 1-D monatomic chain

$$\omega^2 = -\frac{C}{m}(\exp(ika) + \exp(-ika) - 2) = \frac{2C}{m}(1 - \cos(ka)) \ .$$

Phonons are these matter waves propagating through the lattice with wavevector k at a frequency ω.

To consider crystals built from more complex unit cells that are also typically of higher dimensions, one needs to consider the equation of motions for all atoms in the unit cell, eventually arriving at the dispersion relation

$$-m\omega^2 = \sum_j \left(\frac{\partial^2 V}{\partial u_i \partial u_j} \right) \exp(i\vec{k} \cdot (\vec{r}_i - \vec{r}_j)) \ ,$$

where V is the potential energy of the system, which we previously assumed to be the harmonic potential energy between nearest neighbor atoms connected by springs with some force constant. The second derivative terms are often referred to as the harmonic matrix.

In general, for a d-dimensional unit cell with p atoms, there are a total of dp phonon modes. The factor of d arises from the different polarizations possible for each propagating wave. In 3-D, there are two transversely polarized modes (for which the atomic displacements are perpendicular to the direction of propagation) and one longitudinally polarized mode (for which the atomic displacements are parallel to the direction of propagation). For a given polarization, the p phonon branches are separated by energy gaps that arise from differences in mass or force constants within the unit cell. The d modes for which $\omega \to 0$ when $k \to 0$ are called acoustic modes, and typically also show a linear dispersion relation at small k. The remaining modes are referred to as optical modes.

Definition of phonon properties

The **phonon energy** is given by $\hbar\omega$, and the **phonon momentum** is defined as $\hbar\vec{k}$, where $\hbar$ is the reduced Planck's constant. However, note that even though one can define a momentum from the wavevector, the matter waves don't actually carry any momentum.

The **group velocity** is defined as

$$\vec{v}_g(k) = \nabla_k \omega(\vec{k}) \tag{2.1}$$

and describes the velocity at which a wave packet centered about wavevector $\vec{k}$ propagates through the crystal.

The phonon **density of states** is the density of phonon modes at a given frequency within $d\omega$, and is given by $dN/d\omega$, where N is the total number of phonon modes. For example, in 1-D, the density of states is

$$D_1(\omega) = \frac{dN}{d\omega} = \frac{dN}{dk}\frac{dk}{d\omega} = \frac{L}{\pi}\frac{dk}{d\omega} \tag{2.2}$$

where dN/dk is found by noting that allowed values of wavevector k of a chain of M atoms with periodic boundary conditions is $k = 0, \pm 2\pi/L, \pm 4\pi/L, \ldots, \pm M\pi/L$. Thus, we have $2M$ modes within $\Delta k = 2M\pi/L$.

Similarly, in three dimensions, assuming an isotropic crystal, we find that

$$D_3(\omega) = \frac{V|k|^2}{2\pi^2}\frac{d|k|}{d\omega}$$

where V is the volume of the crystal, because the number of modes N contained in a sphere of radius $|k|$ (in reciprocal space) is $N = (L/2\pi)^3(4\pi|k|^3/3)$.

The **thermal energy** is given by

$$U_{\text{lattice}} = \sum_d \sum_k f_{k,d}\hbar\omega_{k,d} = \sum_d \int D_d(\omega) f(\omega) d\omega$$

where the sum goes over all wavevectors k in the Brillouin zone and phonon polarizations d. The terms $f_{k,d}$ and $f(\omega)$ are the occupancies of the phonons specified by either k and d, or by frequency ω. At thermal equilibrium, the phonon occupancy is given by the Planck (or Bose-Einstein) distribution

$$f_0(\omega) = \frac{1}{\exp(\hbar\omega/k_B T) - 1} \ .$$

The **phonon heat capacity**, which assumes constant volume because we are considering crystalline materials, is given by

$$C_v = \frac{\partial U}{\partial T} = k_B \sum_d \int D_d(\omega) \frac{x^2 \exp(x)}{(\exp(x) - 1)^2} d\omega$$

where $x = \hbar\omega/k_B T$, T is the temperature, and k_B is the Boltzmann constant.

Thermal conductivity κ relates the steady-state heat flux q through a material given a temperature gradient

$$q = \sum_d \sum_k v_{gx,k,d} f_{k,d} \hbar\omega_{k,d} \equiv -\kappa \frac{dT}{dx} \ . \tag{2.3}$$

From kinetic gas theory, the thermal conductivity is

$$\kappa = \frac{1}{3} C_v v_g \Lambda$$

where Λ is the mean free path of the phonon (treated as a particle) between Umklapp scattering events. Umklapp scattering occurs when the crystal momentum, given by reciprocal lattice vector $\vec{G}$, contributes to the phonon scattering event. In other words, the scattering of two phonons into a third phonon satisfies

$$\vec{k}_1 + \vec{k}_2 = \vec{k}_3 + \vec{G} \ .$$

In other words, if the scattering of the first two phonons yields a third phonon with momentum $\vec{k}_3$ outside of the first Brillouin zone (defined by the unit cell size in reciprocal space), it can be mapped back to a point within the first Brillouin zone. Thus the scattering event does not appear to conserve momentum (though energy must still be conserved). This phenomenon explains why perfect crystals still have finite thermal resistivity. Normal scattering events ($\vec{G} = 0$) can also occur, but they do not contribute to the thermal resistivity.

Given this expression, at extremely low temperatures, the thermal conductivity scales like T^3 due to the heat capacity, while at high temperatures thermal conductivity drops like $1/T$ due to the mean-free path reflecting the increased probability of collision.

However, note that in order for these scattering events to occur in the bulk of a defect-less crystal, anharmonic lattice interactions need to be included.

Debye model

In the Debye model, we assume a linear dispersion relation $\omega = v_g k$. This model thus is only valid for low energy acoustic modes.

Using this dispersion relation, the density of states (in 3-D) is then

$$D(\omega) = V\omega^2/2\pi^2 v_g^3$$

and one defines a maximum frequency cut-off because the total number of acoustic modes must be N,

$$\omega_D^3 = 6\pi^2 v_g^3 N/V \ .$$

The thermal energy is

$$U = \int_0^{\omega_D} \frac{V\omega^2}{2\pi^2 v_g^3} \frac{\hbar}{e^{\hbar\omega/T} - 1}\, d\omega \ = \ 9Nk_B T \left(\frac{T}{\theta_D}\right)^3 \int_0^{x_D} \frac{x^3}{e^x - 1}\, dx$$

where in the second equation we changed the variable of integration to $x = \hbar\omega/k_B T$ and defined the Debye temperature,

$$\theta_D = \frac{\hbar v_g}{k_B} \left(\frac{6\pi^2 N}{V}\right)^{1/3} \ .$$

The heat capacity is

$$C_v = 9Nk_B \left(\frac{T}{\theta_D}\right)^3 \int_0^{x_D} \frac{x^4 e^x}{(e^x-1)^2}\,dx \;\rightarrow\; \frac{12\pi^4}{5} Nk_B \left(\frac{T}{\theta_D}\right)^3$$

where in the second line we take the limit $x_D \rightarrow \infty$, which is equivalent to taking $T \rightarrow 0$.

Einstein model

In the Einstein model of phonons, all phonons are assumed to be of the same energy, and the density of states is

$$D(\omega) = N\delta(\omega - \omega_E)$$

where N is the number of atoms and thus modes in a 1-D system. (In three dimensions, N is replaced by $3N$.) This model is based on the fact that most optical phonon bands are relatively flat across all k.

The thermal energy is

$$U = \frac{N\hbar\omega_E}{e^{\hbar\omega_E} - 1}$$

and the heat capacity is

$$C_v = Nk_B \left(\frac{\hbar\omega_E}{k_B T}\right)^2 \frac{e^{\hbar\omega_E/k_B T}}{(e^{\hbar\omega_E/k_B T} - 1)^2} \ .$$

In the high temperature limit, $C_V \propto Nk_B$, and in the low temperature limit, $C_V \propto \exp(-h\omega_E/k_B T)$. As expected, the heat capacity in the low temperature limit is incorrect, as it has been observed to scale like T^3 in experiments and as predicted by the Debye model.

Anharmonic scattering

The discussion here can be found in various references on using anharmonic force constants to derive scattering rates [1, 43, 44].

Three-phonon scattering events are constrained by energy and momentum conservation

$$\begin{aligned}
&\omega_j(\vec{k}) \pm \omega_{j'}(\vec{k}') = \omega_{j''}(\vec{k}'') \\
&\vec{k} + \vec{k}' = \vec{k}'' + \vec{G}
\end{aligned}$$

where j and $\vec{k}$ are the phonon mode and wavevector of each phonon (denote by apostrophes) in scattering event, and ω is the corresponding frequency of the phonons. The vector $\vec{G}$ is the crystal reciprocal lattice vector, which is zero for normal scattering processes and nonzero for umklapp scattering processes.

Defining $\lambda = (j, \vec{k})$, the three-phonon scattering rates $W^{\pm}_{\lambda,\lambda',\lambda''}$ are determined by Fermi's golden rule,

$$W^{\pm}_{\lambda,\lambda',\lambda''} = \frac{\hbar\pi}{4N} \frac{(n_{0,\lambda}+1)(n_{0,\lambda'}+1/2 \pm 1/2)n_{0,\lambda''}}{\omega_\lambda \omega_{\lambda'} \omega_{\lambda''}} |V_{\pm}(\lambda, \lambda', \lambda'')|^2 \\ \times \delta(\omega_\lambda \pm \omega'_\lambda - \omega''_\lambda)$$

where N is the number of unit cells, the delta function ensures energy conservation, n_0 is the equilibrium phonon distribution, and

$$V_{\pm}((j,\vec{k}); (j',\vec{k}'); (j'',\vec{k}'')) = \\ \sum_{i_1,i_2,i_3} \sum_{\ell_2,\ell_3} \sum_{\alpha,\beta,\gamma} \Phi_{\alpha,\beta,\gamma}((0,i_1); (\ell_2,i_2); (\ell_3,i_3)) e^{i\vec{k}'\vec{R}_{\ell_2}} e^{i\vec{k}''\vec{R}_{\ell_3}} \\ \frac{\psi^{j}_{\alpha,i_1}(\vec{k}) \psi^{j'}_{\beta,i_2}(\vec{k}') \psi^{j}_{\gamma,i_3}(\vec{k}'')}{\sqrt{m_{i_1} m_{i_2} m_{i_3}}}$$

where numbers 1, 2, and 3 label the atoms coupled together by the anharmonic term, $\{(i,\ell)\}$ indexes the ith atom in the ℓth unit cell, and $\{\alpha, \beta, \gamma\}$ specify the spatial axis (assuming 3-D space). $\vec{R}_\ell$ is the lattice vector pointing to the ℓth unit cell, m_i is the mass of the ith atom in the unit cell, and $\psi^{j}_{\alpha,i}(\vec{k})$ is element in the phonon eigenvector (specified by $(j, \vec{k})$) corresponding to direction α and atom i.

The collision integral then

$$I_{\text{coll}} = \sum_{\lambda',\lambda''} \left[W^{+}_{\lambda,\lambda',\lambda''} (\Psi_{\lambda''} - \Psi_{l'} - \Psi_\lambda) + \frac{1}{2} W^{-}_{\lambda,\lambda',\lambda''} (\Psi_{\lambda''} + \Psi_{l'} - \Psi_\lambda) \right] \equiv \frac{n_{1,\lambda}}{\tau_\lambda} \tag{2.4}$$

where $\Psi = n_{1,\lambda}/[n_{0,\lambda}(n_{0,\lambda}+1)]$ and $n_{1,\lambda}$ is the unknown deviation from the equilibrium phonon distribution. The sum over λ', λ'' is over the three-phonon scattering phase space that satisfies energy and momentum conservation. This sum can be used to determine the scattering lifetime τ of phonon mode λ. The mean free path of the phonon is then $\Lambda = v_g \tau$.

2.3 Introduction to the Boltzmann Transport Equation (BTE)

The discussion below can be found in more detail in Chapter 3 (Kinetic theory of gases) in the textbook by Kardar [45].

Consider an N-body system, fully described by the generalized position ($\vec{r}_i$) and momentum ($\vec{p}_i$) of each particle indexed by i in 3-dimensional space. The space defined by these coordinates is called the phase space. Let **r** and **p**, containing information on the positions and momenta for each of the N particles, denote specific points in phase space. Let the particle density be described by $f(\mathbf{r};\mathbf{p})$.

Due to the incompressibility of phase space, we know that the change in density at some **r**, **p** with respect to time is given by

$$\frac{df}{dt} = \frac{\partial f}{\partial t} + \sum_i \left(\frac{\partial f}{\partial \vec{r}_i} \frac{\partial \vec{r}_i}{\partial t} + \frac{\partial f}{\partial \vec{p}_i} \frac{\partial \vec{p}_i}{\partial t} \right) = 0 \ . \tag{2.5}$$

In the case that $\frac{df}{dt} = 0$, we arrive at Liouville's equation.

However, it is proposed that one can simplify the above equation, which involves the full phase space, by reducing it to a 1-particle density that returns the expectation value of finding any of the N particles at location $\vec{r}$ with momentum $\vec{p}$. This can be done following the Bogoliubov-Born-Green-Kirkwood-Yvon (BBGKY) hierarchy. Details can be found in Kardar [45]. In the end, in the dilute particle limit, we only need to consider the first equation of the hierarchy,

$$\frac{df_1}{dt} = \frac{\partial f_1}{\partial t} + \frac{\partial f_1}{\partial \vec{r}_i} \frac{\partial \vec{r}_i}{\partial t} + \frac{\partial f_1}{\partial \vec{p}_i} \frac{\partial \vec{p}_i}{\partial t} = \left(\frac{df_1}{dt} \right)_c \tag{2.6}$$

where the last term is the collision term obtained by considering the interactions of the single particle captured by the first hierarchical equation with the other remaining particles.

Thus, additionally defining velocity $\vec{v} = \partial \vec{r} / \partial t$ and force $F = \partial \vec{p} / \partial t$ for the 1-particle density, and dropping the 1 index, we arrive at the BTE

$$\frac{\partial f}{\partial t} + \vec{v} \cdot \nabla_{\vec{r}} f + \vec{F} \cdot \nabla_{\vec{p}} f = \left(\frac{df}{dt} \right)_c \ . \tag{2.7}$$

The collision integral can be determined by kinematic collision and scattering theory. However, one can also use a quantum mechanical description, ie. Fermi's Golden Rule, which dictates conservation of energy and conservation of momentum in the collision and the transition probability determined by the Hamiltonian describing the interaction between the particles.

Relaxation time approximation

It is common to simplify the collision term using the relaxation time approximation, using the relation

$$\left(\frac{df}{dt}\right)_c = -\frac{f - f_0(T)}{\tau}$$

where $f_0(T)$ is the equilibrium distribution at some temperature T and τ is called the particle lifetime.

For phonons, the collision integral can be determined using three-phonon scattering events, as given in Eq. (2.4).

BTE for heat transfer

Phonons are determined by atomistic material properties, and are described by a dispersion relation $\omega(\vec{k})$, where ω is the frequency of the phonons. Each wavevector can specify multiple phonons of different polarizations.

We use the BTE to separately describe the density of each phonon mode, indexed by λ which specifies both wavevector $\vec{k}$ and polarization. The velocity is the group velocity of the phonon, given by $\vec{v}_g = \nabla_{\vec{k}}\omega(\vec{k})$. It is not possible to exert forces on phonons, so the force term is dropped. The collision term is approximated using the three-phonon scattering rates that can be obtained using ab initio methods like density functional perturbation theory [1]. Volumetric heat generation can also be included here with the collision term. Thus, we arrive at

$$\frac{\partial f_\lambda}{\partial t} + \vec{v}_{g,\lambda} \cdot \nabla_{\vec{r}} f_\lambda = -\frac{f_\lambda - f_{0,\lambda}(T)}{\tau_\lambda} + Q_\lambda \ . \tag{2.8}$$

Note that the equilibrium distribution $f_0(T)$ depends on the current temperature of the system, which depends on the phonon distribution. If we are only considering heat transfer along one direction, we can write

$$\frac{\partial f_\lambda}{\partial t} + v_{gx,\lambda}\frac{\partial f_\lambda}{\partial x} = -\frac{f_\lambda - f_{0,\lambda}(T)}{\tau_\lambda} + Q_\lambda \ . \tag{2.9}$$

Because the equilibrium distribution should yield time derivations that equal zero, one can write the BTE in terms of energy deviations from the equilibrium distribution at the equilbrium temperature T_0, which we denote as $g(T) = \hbar\omega(f(T) - f_0(T_0))$,

$$\frac{\partial g_\lambda}{\partial t} + v_{gx,\lambda}\frac{\partial g_\lambda}{\partial x} = -\frac{g_\lambda - \left(g_{0,\lambda}(T) - g_{0,\lambda}(T_0)\right)}{\tau_\lambda} + Q_\lambda \ . \tag{2.10}$$

Assuming a small deviation in temperature $\Delta T = T - T_0$,

$$g_{0,\lambda}(T) - g_{0,\lambda}(T_0) = \hbar\omega_\lambda(f_{BE,\lambda}(T) - f_{BE,\lambda}(T_0)) \approx C_\lambda \Delta T$$

where $f_{BE,\lambda}(T) = (e^{\hbar\omega_\lambda/k_BT} - 1)^{-1}$ is the Bose-Einstein distribution at temperature T, and $C_\lambda = \hbar\omega_\lambda \frac{\partial f_{BE,\lambda}}{\partial T}$ is the modal heat capacity. Thus, the BTE for heat transfer is

$$\frac{\partial g_\lambda}{\partial t} + v_{gx,\lambda}\frac{\partial g_\lambda}{\partial x} = -\frac{g_\lambda - C_\lambda \Delta T}{\tau_\lambda} + Q_\lambda \ . \tag{2.11}$$

Finally, g_λ and ΔT are related by energy conservation,

$$\sum_\lambda (g_\lambda - C_\lambda \Delta T) = 0 \ . \tag{2.12}$$

Note that all phonons contribute to ΔT, thus requiring the BTE for all phonons to be considered simultaneously.

1-D BTE: General solution

For simplicity, we assume a stationary solution and no internal heat generation, so that Eq. (2.11) becomes

$$v_{gx,\lambda}\frac{\partial g_\lambda}{\partial x} = -\frac{g_\lambda - C_\lambda \Delta T}{\tau_\lambda} \ . \tag{2.13}$$

This a 1-D ordinary differential equation, and the forward propagating and backward propagating solutions for g_λ are, respectively,

$$g_\lambda^+(\hat{x}) = P_\lambda \, \mathrm{e}^{-\gamma_\lambda \hat{x}} + \int_0^{\hat{x}} \frac{C_\lambda \Delta T(\hat{x}')}{\mathrm{Kn}_\lambda} \, \mathrm{e}^{-\gamma_\lambda(\hat{x}-\hat{x}')} \, d\hat{x}' \qquad \text{for } v_{gx,\lambda} > 0 \tag{2.14a}$$

$$g_\lambda^-(\hat{x}) = B_\lambda \, \mathrm{e}^{\gamma_\lambda(1-\hat{x})} - \int_{\hat{x}}^{1} \frac{C_\lambda \Delta T(\hat{x}')}{\mathrm{Kn}_\lambda} \, \mathrm{e}^{\gamma_\lambda(\hat{x}'-\hat{x})} \, d\hat{x}' \qquad \text{for } v_{gx,\lambda} \leq 0 \tag{2.14b}$$

where $\hat{x} = x/L$ is the normalized distance, $\Delta T(\hat{x})$ is the local deviation in temperature from T_0, $\mathrm{Kn}_\lambda = v_{gx,\lambda}\tau_\lambda/L$ is the modal Knudsen number, and $\gamma_\lambda = 1/\mathrm{Kn}_\lambda$. The coefficients P_λ and B_λ are defined by boundary conditions at the edges of the slab,

$$g_\lambda^+(\hat{x}=0) = P_\lambda = \epsilon_1 C_\lambda \Delta T_L + (1-\epsilon_1)\sum_\lambda g_\lambda^-(\hat{x}=0) \tag{2.15a}$$

$$g_\lambda^-(\hat{x}=1) = B_\lambda = \epsilon_2 C_\lambda \Delta T_R + (1-\epsilon_2)\sum_\lambda g_\lambda^+(\hat{x}=1) \tag{2.15b}$$

where ΔT_L and ΔT_R are the temperature offsets defined at the left and right edges of the slab, and ϵ denotes the emissivity of the two boundaries. For Dirichlet boundary conditions, the walls are black and $\epsilon = 1$.

The modal deviational heat flux is

$$q_\lambda = q_\lambda^+ - q_\lambda^- = v_{gx,\lambda}(g_\lambda^+ - g_\lambda^-) \ , \tag{2.16}$$

and the thermal conductivity is

$$\kappa = \sum_\lambda \frac{q_\lambda}{(\Delta T_R - \Delta T_L)/L} \ . \tag{2.17}$$

Combining Eq. (2.12) and Eq. (2.14), we obtain an integral equation for $\Delta T(\hat{x})$,

$$\begin{aligned}&\left(\sum_\lambda \frac{C_\lambda}{\tau_\lambda}\right)\Delta T(\hat{x}) \\ &\quad = \sum_\lambda \frac{1}{\tau_\lambda}\left[P_\lambda e^{-\gamma_\lambda \hat{x}} + B_\lambda \, \mathrm{e}^{-\gamma_\lambda(1-\hat{x})} + \int_0^1 \frac{C_\lambda \Delta T(\hat{x}')}{\mathrm{Kn}_\lambda} e^{-\gamma_\lambda|\hat{x}'-\hat{x}|} \, d\hat{x}'\right]\end{aligned} \tag{2.18}$$

which is a Fredholm integral of the second kind, as it is of the form

$$\Delta T(\hat{x}) = f(\hat{x}) + \int_0^1 K(\hat{x},\hat{x}')\Delta T(\hat{x}') \, d\hat{x}' \ . \tag{2.19}$$

One way to numerically solve for $\Delta T(\hat{x})$ is to write the variable as a vector with each element corresponding to a different point along $\hat{x}$. One could use an even discretization or a quadrature (eg. Gaussian quadrature) discretization. However, this spatial discretization requires on the order of 1000 points for convergence [41]. Alternatively, $\Delta T(\hat{x})$ can be solved for by expanding f and K as a cosine expansion with N terms. After some mathematical manipulation as detailed by Hua et al. [41], one can write $\Delta T(\hat{x})$ as a matrix equation

$$\Delta T(\hat{x}; \vec{P}, \vec{B}) = \mathbf{\Phi}(\hat{x}) \left(\mathbf{I} - \frac{1}{2}\mathbf{K}\right)^{-1} \left(\mathbf{F}_1 \vec{P} + \mathbf{F}_2 \vec{B}\right) \ . \tag{2.20}$$

Here, $\mathbf{\Phi}(\hat{x})$ is a matrix of the cosines used in the expansion. Values of the cosines with spatial frequencies $m\pi$, where m is an integer from 0 to N, evaluated at various $\hat{x}$ are along each column. The vectors $\vec{P}$ and $\vec{B}$ are defined by the boundary conditions and contain N_{ph} values, where N_{ph} is the total number of phonon modes. The $(N+1) \times (N+1)$ matrix $\mathbf{K}$ contains the cosine expansion coefficients of the kernel $K(\hat{x},\hat{x}')$. The F matrices correspond to the cosine expansion coefficients for the inhomogeneous term $f(\hat{x})$, and are of dimension $(N+1) \times N_{\mathrm{ph}}$. Explicit expressions for the matrix elements are given in the following section.

Cosine expansion matrix elements

In all of the following equations, the normalization factor is $M = 2\sum_\lambda C_\lambda/\tau_\lambda$. These coefficients are generalized versions of those given in the Appendix of Ref. [41].

The kernel $K(x, x')$ is

$$K(\hat{x}, \hat{x}') = \frac{1}{M} \sum_{\lambda} \frac{C_\lambda}{\mathrm{Kn}_\lambda \tau_\lambda} e^{-\gamma_\lambda |\hat{x} - \hat{x}'|} \ . \tag{2.21}$$

The elements in $\mathbf{K}$ are the coefficients for the cosine expansion,

$$[\mathbf{K}]_{m,n} = \frac{c}{M} \int_0^1 \int_0^1 K(\hat{x}, \hat{x}') \cos(m\pi\hat{x}) \cos(n\pi\hat{x}') \, d\hat{x} \, d\hat{x}' \tag{2.22}$$

$$= \begin{cases} \dfrac{c}{M} \displaystyle\sum_{\lambda} \frac{C_\lambda}{\mathrm{Kn}_\lambda \tau_\lambda} \left[\dfrac{(((-1)^m + (-1)^n) e^{-\gamma_\lambda} + (-1 - (-1)^{m+n}))\gamma_k^2}{(\gamma_\lambda^2 + m^2\pi^2)(\gamma_\lambda^2 + n^2\pi^2)} \right] & \text{if } m \neq n \\[2ex] \dfrac{c}{M} \displaystyle\sum_{\lambda} \frac{C_\lambda}{\mathrm{Kn}_\lambda \tau_\lambda} \left[\dfrac{e^{-\gamma_\lambda}(2(-1)^m \gamma_\lambda^2) + \gamma_\lambda((\gamma_\lambda - 2)\gamma_\lambda + m^2\pi^2)}{(\gamma_\lambda^2 + m^2\pi^2)^2} \right] & \text{if } m = n \neq 0 \\[2ex] \dfrac{c}{M} \displaystyle\sum_{\lambda} \frac{C_\lambda}{\mathrm{Kn}_\lambda \tau_\lambda} \left[\dfrac{2(-1 + e^{-\gamma_\lambda} + \gamma_\lambda)}{\gamma_\lambda^2} \right] & \text{if } m = n = 0 \end{cases}$$

where $c = 1$ if $m = n = 0$, $c = 2$ if either $m = 0$ or $n = 0$, or $c = 4$ if both $m, n \neq 0$.

The inhomogeneous term is $f(\hat{x}) = \sum_\lambda f_{1,\lambda}(\hat{x}) P_\lambda + f_{2,\lambda}(\hat{x}) B_\lambda$, where

$$f_{1,\lambda}(\hat{x}) = \frac{1}{M} \frac{1}{\tau_\lambda} e^{-\gamma_\lambda \hat{x}} \tag{2.23a}$$

$$f_{2,\lambda}(\hat{x}) = \frac{1}{M} \frac{1}{\tau_\lambda} e^{-\gamma_\lambda (1 - \hat{x})} \ . \tag{2.23b}$$

The elements in $\mathbf{F}_b$ are the cosine expansion coefficients $[\mathbf{F}_b]_{m,\lambda} = c \int_0^1 f_{b,\lambda}(\hat{x}) \cos(m\pi\hat{x}) \, d\hat{x}$ (where $b = 1, 2$), which yield

$$[\mathbf{F}_1]_{m,\lambda} = \frac{c}{M} \frac{1}{\tau_\lambda} \left[\frac{(1 - (-1)^m e^{-\gamma_\lambda})}{\gamma_\lambda (1 + m^2\pi^2/\gamma_\lambda^2)} \right] \tag{2.24a}$$

$$[\mathbf{F}_2]_{m,\lambda} = \frac{c}{M} \frac{1}{\tau_\lambda} \left[\frac{((-1)^m - e^{-\gamma_\lambda})}{\gamma_\lambda (1 + m^2\pi^2/\gamma_\lambda^2)} \right] \tag{2.24b}$$

where $c = 1$ if $m = 0$, and $c = 2$ otherwise.

1-D BTE: Diffusive limit

Fourier's law describes heat transfer in the diffusive limit and is valid for bulk systems. Unfortunately, taking the equations for heat flux (Eq. (2.14)) in the limit Kn goes to 0^+ yields a deviational heat flux of 0, which is a not informative zeroth order solution. Instead, we start back at Eq. (2.9). Under the assumption that the deviational phonon energy g_λ and its gradient is much smaller than the equilibrium phonon distribution, and assuming a stationary solution and no internal heat generation, we have

$$v_{gx,\lambda}\frac{\partial g_{0,\lambda}}{\partial x} = -\frac{g_\lambda - g_{0,\lambda}(T)}{\tau_\lambda} \ .$$

We can then solve for g_λ,

$$g_\lambda = g_0 - \tau_\lambda\, v_{gx,\lambda}\frac{\partial g_{0,\lambda}}{\partial x} = g_0 - \tau\, v_{gx,\lambda}\frac{\partial g_{0,\lambda}}{\partial T}\frac{dT}{dx} \ .$$

Thus, after multiplying the deviational phonon population by the group velocity and summing over all phonon modes, we arrive at Fourier's law for the deviational heat flux,

$$q = \sum_\lambda v_{gx,\lambda}(g_\lambda - g_{0,\lambda}) = -\sum_\lambda v_{gx,\lambda}^2 \tau \frac{\partial g_{0,\lambda}}{\partial T}\frac{dT}{dx} = -\sum_\lambda -C_\lambda v_{gx,\lambda}\Lambda_\lambda \frac{dT}{dx} \equiv -\kappa\frac{dT}{dx}$$

from which we define the thermal conductivity κ.

More generally, one can follow the Chapman-Enskog solution to the BTE and assume a 'Hilbert-type' expansion of the phonon distribution [34],

$$g = \sum_{n=0}^{\infty} \langle \mathrm{Kn} \rangle^n g_n$$

where the gray approximation is used and $\langle \mathrm{Kn} \rangle$ is averaged over all phonons. Taking the expansion only up to the first order term is valid for small Kn, and returns Fourier's law when inserted into the expression for heat flux (Eq. (2.3)) [34]. Consistent with what we discussed above, the first order expansion in Kn is required because the zeroth order expansion yields no heat flux (ie. is the equilbirium phonon distribution).

1-D BTE: Ballistic Limit

Suppose we are interested in heat flow across a thin layer or at an interface. In the ballistic limit, the mean free path is much longer than the length of the system of interest, and the phonon scattering is dominated by scattering at the boundary. Equivalently, in the BTE, we can take the limit $\tau_\lambda \to \infty$, and as a result, the phonon distribution is constant through the thin system.

However, complications arise when the two ends of the slab are pinned to different temperatures. It turns out that because phonons can't dissipate heat in the bulk material, a discontinuity in the temperature appears at the boundaries.

One can see this by taking Eqs. (2.14) in the infinite scattering lifetime limit (so that Kn $\rightarrow \infty$ and $\gamma \rightarrow 0$), yielding

$$\begin{aligned} q_\lambda(\hat{x}) = v_{gx,\lambda}(g_\lambda^+(\hat{x}) - g_\lambda^-(\hat{x})) &= v_{gx,\lambda}\left(P_\lambda - B_\lambda\right) \\ &= v_{gx,\lambda} C_\lambda (\Delta T_1 - \Delta T_2) \end{aligned}$$

where we assumed Dirichlet boundary conditions (Eqs. (2.15)).

This result is not obviously obtainable using Fourier's law. However, one can incorporate temperature slippage manually [35], which was shown to be equivalent to including a first order correction of phonons emitted from the boundary [34].

In this limit, the deviational heat flux should be consistent with the Landauer formalism,

$$q = \sum_\lambda v_{gx,\lambda}\, g_\lambda\, \boldsymbol{T}_\lambda^{(1,2)}$$

in which we simply sum over the energies of the phonons passing through the system, scaled by their transmissivities $\boldsymbol{T}^{(1,2)}$ through the system. In the case we are considering here, $\boldsymbol{T}^{(1,2)} = 1$. The transmissivities can be less than 1 if considering heat flux across an interface that reflects some of the incoming phonons.

2.4 Prior Work on Superlattice Thermal Conductivity

1-D superlattices are structures built from various layers stacked sequentially in some periodic fashion. For example, a binary superlattice would consist of two types of layers placed in an alternating fashion.

Classical heat transfer in superlattices

At an interface, the bulk material's periodicity is broken, and incident phonons scatter into other phonon modes. One can use reflection or transmission matrices to describe the coupling of the incident phonon to phonon modes travelling back through the original layer or phonons travelling forward through the next layer, respectively. The scattering at the interface must satisfy boundary conditions such as energy conservation, detailed balance of heat flux, conservation of transverse momentum, and time reversal symmetry. Unlike the scattering of light, which is accurately described by Snell's law, the scattering of phonons is often not so simple, since the phonon band structure is more complicated and the boundary conditions can potentially be satisfied by multiple phonon modes. Furthermore, the scattering is sensitive to the quality of the interface, and the thermal conductivity across the interface is known to vary significantly depending on the interface.

Several models describing the scattering at an interface have been developed. For simplicity, one often assumes an isotropic material, meaning that the phonon of some frequency propagates in all directions at the same group velocity, and can be specified by the group velocity magnitude v_g, wavevector magnitude k, and angle of propagation θ (with respect to normal). Thus, the interface transmission models discussed below are often written as functions of phonon frequency and angle of incidence.

If one assumes that phonons undergo elastic scattering based on **Snell's law**, the transmission is determined by the constraint

$$\frac{\sin\theta_1}{|v_g^{(1)}|} = \frac{\sin\theta_2}{|v_g^{(2)}|}$$

where i denotes the superlattice layer. When this constraint cannot be met (ie. the angle of incidence is greater than some critical value), the phonon is completely reflected and nothing is transmitted through the interface. However, this model only holds for transversely polarized low frequency acoustic modes where the phonon dispersion relation is approximately linear and there is no mode conversion.

In the elastic **acoustic mismatch model** (AMM) [46], one instead uses impedance matching to determine reflection and transmission across the interface, arriving at

$$\begin{aligned} \boldsymbol{R}^{(1,2)}(\cos\theta^{(1)}) &= \left|\frac{Z^{(1)}\cos\theta^{(1)} - Z^{(2)}\cos\theta^{(2)}}{Z^{(1)}\cos\theta^{(1)} + Z^{(2)}\cos\theta^{(2)}}\right|^2 \\ \boldsymbol{T}^{(1,2)}(\cos\theta^{(1)}) &= \frac{4Z^{(1)}Z^{(2)}\cos\theta^{(1)}\cos\theta^{(2)}}{(Z^{(1)}\cos\theta^{(1)} + Z^{(2)}\cos\theta^{(2)})^2} \end{aligned} \tag{2.25}$$

where $Z^{(i)} = \rho^{(i)}|v_g^{(i)}|$ is the acoustic impedance of the ith layer, with ρ being the material density.

At rough interfaces, one might expect incident phonons to undergo multiple scattering events. It is argued that in the diffuse scattering limit [47], phonons at the interface would forget which side they were on. Then, in the **diffuse mismatch model** (DMM), transmission of a phonon from layer j into i looks the same as reflection of a phonon in layer i off of the interface back into i. Mathematically, this can be written as

$$\boldsymbol{T}^{(i,j)} = \boldsymbol{R}^{(i.j)} = 1 - \boldsymbol{T}^{(j,i)} \ .$$

Thus, assuming elastic scattering events, energy balance requires that

$$\sum_m 2\pi \int_0^{\pi/2} v_{g,m}^{(1)} \cos(\theta) g D_m^{(1)}(\omega) \boldsymbol{T}^{(1,2)}(\omega)\, d\theta = \\ \sum_m 2\pi \int_0^{\pi/2} v_{gx,m}^{(2)} \cos(\theta) g D_m^{(2)}(\omega) \boldsymbol{T}^{(2,1)}(\omega)\, d\theta$$

for all phonon frequencies ω, where m indexes all phonons of that frequency. In the low temperature limit where the Debye model is valid, $C \propto v_g^{-3}$, and the DMM model can be reduced to

$$\boldsymbol{T}_d^{(i,j)}(\omega) = \frac{\sum_m (|v_{g,m}^{(j)}|)^{-2}}{\sum_m (|v_{g,m}^{(i)}|)^{-2} + \sum_m (|v_{g,m}^{(j)}|)^{-2}} \tag{2.26}$$

where again m indexes all phonons of frequency ω.

Note that by definition, DMM does not actually preserve time reversal symmetry.

Prior works computing the superlattice thermal conductivity using the BTE assume **frequency-independent transmission and reflection models**. This is because the works assume constant mean-free path and write the BTE as a function of the total deviational phonon intensity [38]

$$I = \frac{1}{2} \sum_m \int_0^{\omega_{\max}} |v_{g,m}(\omega)| g(\omega) D_m(\omega)\, d\omega$$

where $g(\omega)$ is the the deviational phonon energy distribution, $D(\omega)$ is the phonon density of states, and m indexes over the different phonon polarizations. Scattering at the interfaces now are described by boundary conditions enforcing energy conservation with respect to the total phonon density I for a differential solid angle, requiring

$$\boldsymbol{T}^{(1,2)}(\theta_1)\, I_o^{(1)}(T)\, d\cos\theta_1 = \boldsymbol{T}^{(2,1)}(\theta_2)\, I_o^{(2)}(T)\, d\cos\theta_2$$

where $I_o = v_g C(T - T_0)/4\pi$ is the equilibrium total deviational phonon intensity.

Given some model describing phonon transmission through an interface, one can compute its **thermal boundary resistance** (TBR, or Kapitza resistance), $R_{\text{int}} =$

$\Delta T_{\text{int}}/q$ where ΔT_{int} is the non-equilibrium temperature difference of the phonons emitted on either side of the interface, and q is the heat flux flowing through the interface. Thus, the interface's TBR also varies with the thicknesses of the materials on either side of it. For example, in the limit that of thick superlattice layers, one should expect to see diffusive phonon transport in accordance with Fourier's law, in addition to the temperature drops at the interfaces. In contrast, in the limit of thin superlattice layers, one should expect most of the temperature drop to occur across the interfaces. Thus, the TBR would appear to be larger in superlattices with thin layers.

To compute the heat flux through a 1-D superlattice, one requires a scattering model for each distinct interface. Then, one solves a system of integral equations that enforce heat flux conservation and energy conservation as described by the transmission and reflection matrices, which are expressed depend on the unknown phonon intensity and the local non-equilibrium temperature. To solve the BTE for total phonon intensity, Chen numerically solves the system of equations using the Gauss-Legendre integration scheme to compute the integrals in the equations [38]. An nth order Gauss quadrature would yield n equations for each original integral equation. The unknowns are obtained by matrix inversion.

Simkin and Mahan model

Simkin and Mahan used lattice dynamics and the concept of band-folding to predict the cross-plane thermal conductivity of 1-D superlattices [22, 48]. They discuss a simple model where the atoms in the superlattice layers only vary by mass, and obtain the phonon dispersion relation by solving for the characteristic equations of motion describing their simple system. However, to compute thermal conductivity, they utilize a gray model and assume constant mean free path (MFP). For finite MFP, they observe a dip in the thermal conductivity with respect to superlattice period (the width of the layers). It is proposed that this dip is indicative of the wave-particle crossover point, at which phonons behave in the coherent wave-like limit for smaller superlattice periods and in the particle-like limit for larger superlattice periods.

Other atomistic thermal transport methods

In molecular dynamics (MD) calculations, one specifies the positions and force constants of all of the atoms in the system of interest and propagates the motion of each particle (classically) according to Newton's equations of motions in time, given some initial conditions [49]. The force constants are approximated from non-harmonic interatomic potentials, such as the Stillinger-Weber or Tersoff potential. Several methods to compute the sample's thermal conductivity from these calculations have been reported. For example, one can consider a sample that is in contact with hot and cold baths and compute the heat flow between them [50], or one can measure the average energy of the atoms to determine the local temperature [51]. Alternatively, one can measure correlation functions of thermal fluctuations and then use the Green-Kubo formalism to determine the contributions to thermal conductivity from each phonon [52, 53] or other normal modes [54]. Extending the MD algorithm to consider periodic superlattices is straightforward as one simply modifies the set of atoms to simulate.

Alternatively, one can compute the thermal conductivity of the superlattice using ab initio harmonic and anharmonic force constants computed using density functional perturbation theory (DFPT) [1, 43, 44]. The procedure is analogous to that of computing the thermal conductivity of a crystalline bulk material, except one computes the harmonic and anharmonic forces of the entire superlattice supercell, and thus is much more expensive [24]. One can also account for interfacial scattering by adding an additional contribution to the anharmonic scattering using Matthiessen's rule for computing the total lifetime [23]. However, computing the force constants, band structure, and scattering rates for large unit cells is expensive, so one is generally limited to atomistically thin superlattice periods.

The atomistic Green's functions (AGF) method is a quantum mechanical scheme to compute the scattering properties across interfaces. It relies on using harmonic force constants to compute the Green's functions and self-energies of the left boundary, the right boundary, and the central region containing the interface [26]. Using these elements, one can determine the transmission between the left and right boundaries, and then compute the thermal conductivity using Landauer's formula if desired. To compute the thermal conductivity for superlattices, one would need to incorporate multiple layers in the central region, which complicates computing the system's Green's functions and self energies [25].

2.5 Solving the Spectral BTE for 1-D Superlattices

For simplicity, we consider a binary superlattice as shown in Fig. 2.1, though one can easily consider arbitrary superlattices using the framework provided here. For generality, we will denote the thicknesses of the two layers as $L^{(1)}$ and $L^{(2)}$ (though in our calculations the two are the same). We will use the following notation: all

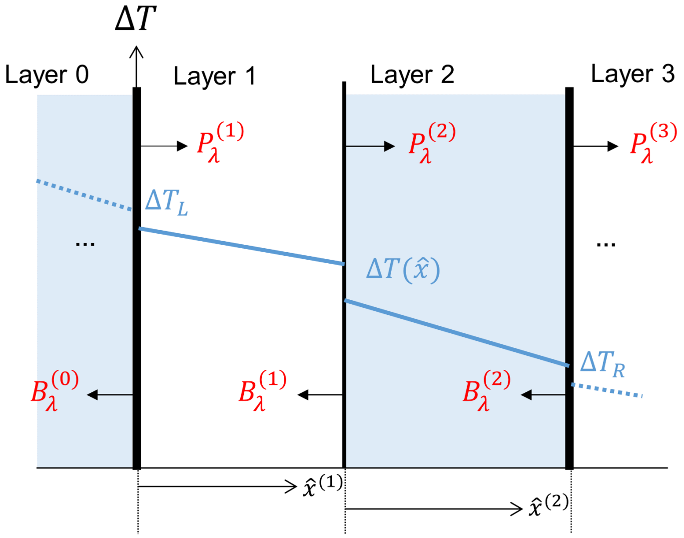

Figure 2.1: Schematic of the binary 1-D superlattice system consisting of a unit cell of two layers. $\Delta T(\hat{x})$ is the deviation of the local temperature with respect to the equilibrium temperature, and ΔT_L and ΔT_R are the temperatures specified at the left and right boundaries, respectively. $\hat{x}^{(\alpha)}$ is the spatial coordinate for layer α normalized by layer thickness $L^{(\alpha)}$. The variables $P_\lambda^{(\alpha)}$ and $B_\lambda^{(\alpha)}$ are the coefficients of the inhomogeneous solution of the Boltzmann equation, which determine the heat flux propagating in the forward and backward direction. In the case of periodic boundary conditions, $B_\lambda^{(0)} = B_\lambda^{(2)}$ and $P_\lambda^{(3)} = P_\lambda^{(1)}$.

material parameters will be written as vectors of size N_{ph} (the number of phonon modes used to describe the thermal properties of the material) where each element is the value for a specific phonon mode. Material parameters for a specific mode will be referred to using subscripts i, j, or λ. Superscripts in parentheses will denote the layer, if needed. If superscripts are omitted, then the expression is valid for all layers generally. When the subscripts are omitted, we are referring to all phonon modes. Matrices will be bolded and vectors will have an arrow. For example, $\vec{C}^{(1)}$ refers to the heat capacities for all phonon modes in layer 1, and $C_\lambda^{(1)}$ refers to the heat capacity of the phonon indexed by λ in layer 1. Multiplication of two vectors, such as $\vec{v}_{gx}\vec{C}$, corresponds to elemental multiplication. Multiplication of a matrix and a vector follows ordinary matrix algebra.

Interface boundary conditions

At each interface, phonons are transmitted or reflected with some probability. The phonons that the original is scattered to depends on the phonon wavevector and frequency, as well as the specularity of the interface. We assume elastic scattering such that phonons only reflect or transmit to phonons of the same frequency ω. The phonon scatterings are further constrained by basic symmetries and conservation laws.

Relations that enforce heat flux conservation are given by

$$\vec{q}^{\,(2),+} = \boldsymbol{T}^{(1,2)}\,\vec{q}^{\,(1),+} + \boldsymbol{R}^{(2,1)}\,\vec{q}^{\,(2),-} \tag{2.27a}$$

$$\vec{q}^{\,(1),-} = \boldsymbol{R}^{(1,2)}\,\vec{q}^{\,(1),+} + \boldsymbol{T}^{(2,1)}\,\vec{q}^{\,(2),-} \;. \tag{2.27b}$$

Here, $R^{(\alpha,\beta)}$ is a $(N_{\text{ph}}^{(\alpha)} \times N_{\text{ph}}^{(\alpha)})$ matrix specifying the reflection coefficients of phonons in layer α at the interface between layers α and β. $\boldsymbol{T}^{(\alpha,\beta)}$ is a $(N_{\text{ph}}^{(\alpha)} \times N_{\text{ph}}^{(\beta)})$ matrix describing the transmission of phonons from layer α into layer β.

The reflection and transmission matrices of each phonon are subject to the constraints of power conservation,

$$\sum_j R_{ij}^{(1,2)} + T_{ij}^{(1,2)} = 1 \tag{2.28a}$$

$$\sum_j R_{ij}^{(2,1)} + T_{ij}^{(2,1)} = 1 \;, \tag{2.28b}$$

time reversal symmetry,

$$\boldsymbol{R}^{(1,2)} = \left(\boldsymbol{R}^{(1,2)}\right)^T \tag{2.29a}$$

$$\boldsymbol{R}^{(2,1)} = \left(\boldsymbol{R}^{(2,1)}\right)^T \tag{2.29b}$$

$$\boldsymbol{T}^{(1,2)} = \left(\boldsymbol{T}^{(2,1)}\right)^T \;, \tag{2.29c}$$

and detailed balance,

$$\sum_{j\in\omega} \boldsymbol{T}_{ij}^{(1,2)} \vec{q}_{j,0}^{\,(1),+} = \sum_{j\in\omega} \boldsymbol{T}_{ij}^{(2,1)} \vec{q}_{j,0}^{\,(2),-} \tag{2.30}$$

where $q_{j,0} = C_j v_{gx,j} T_0$ is the equilibrium heat flux for each phonon mode. These sums occur over all modes of the same frequency ω, as indicated by the notation $j \in \omega$.

Heat transfer across an interface

To determine heat transfer at the interface, we plug our expressions for $\vec{q}(\hat{x})$ (obtained by combining Eq. (2.14), Eq. (2.16), and Eq. (2.20) from the section describing the solution to the BTE of the cross-plane thermal conductivity for a single slab) into the equations expressing conservation of heat flux (Eq. (2.27)) and get

$$\begin{aligned} &P_i^{(2)} v_{gx,i}^{(2)} u_i^{(2)} = \\ &\quad T_{ij}^{(1,2)} \left[P_j^{(1)} e^{-\gamma_j^{(1)}} v_{gx,j}^{(1)} u_j^{(1)} + \left[\mathbf{\Phi}_f^{(1)} \left(\left(\mathbf{I} - \frac{1}{2}\mathbf{K}^{(1)} \right)^{-1} (\mathbf{F}_1^{(1)} \vec{P}^{(1)} + \mathbf{F}_2^{(1)} \vec{B}^{(1)}) \right) \right]_j \right] \\ &\quad + R_{ij}^{(2,1)} \left[B_j^{(2)} e^{-\gamma_j^{(2)}} v_{gx,j}^{(2)} u_j^{(2)} + \left[\mathbf{\Phi}_b^{(2)} \left(\left(\mathbf{I} - \frac{1}{2}\mathbf{K}^{(2)} \right)^{-1} (\mathbf{F}_1^{(2)} \vec{P}^{(2)} + \mathbf{F}_2^{(2)} \vec{B}^{(2)}) \right) \right]_j \right] \end{aligned} \tag{2.31a}$$

$$\begin{aligned} &B_i^{(1)} v_{gx,i}^{(1)} u_i^{(1)} = \\ &\quad R_{ij}^{(1,2)} \left[P_j^{(1)} e^{-\gamma_j^{(1)}} v_{gx,j}^{(1)} u_j^{(1)} + \left[\mathbf{\Phi}_f^{(1)} \left(\left(\mathbf{I} - \frac{1}{2}\mathbf{K}^{(1)} \right)^{-1} (\mathbf{F}_1^{(1)} \vec{P}^{(1)} + \mathbf{F}_2^{(1)} \vec{B}^{(1)}) \right) \right]_j \right] \\ &\quad + T_{ij}^{(2,1)} \left[B_j^{(2)} e^{-\gamma_j^{(2)}} v_{gx,j}^{(2)} u_j^{(2)} + \left[\mathbf{\Phi}_b^{(2)} \left(\left(\mathbf{I} - \frac{1}{2}\mathbf{K}^{(2)} \right)^{-1} (\mathbf{F}_1^{(2)} \vec{P}^{(2)} + \mathbf{F}_2^{(2)} \vec{B}^{(2)}) \right) \right]_j \right] \end{aligned} \tag{2.31b}$$

where the i, j subscripts indicate the phonon mode, and u_λ is the weighting associated with phonon mode λ denoted explicitly.

The matrices $\mathbf{\Phi}_f$ and $\mathbf{\Phi}_b$ are defined as

$$[\mathbf{\Phi}_f]_{m,\lambda} = \int_0^1 \frac{C_\lambda \cos(m\pi\hat{x}')}{\mathrm{Kn}_\lambda} e^{-\gamma_\lambda(1-\hat{x}')} d\hat{x}' = \frac{M}{c} C_\lambda L [F_2]_{m,\lambda} \tag{2.32}$$

$$[\mathbf{\Phi}_b]_{m,\lambda} = \int_0^1 \frac{C_\lambda \cos(m\pi\hat{x}')}{\mathrm{Kn}_\lambda} e^{-\gamma_\lambda \hat{x}'} d\hat{x}' = \frac{M}{c} C_\lambda L [F_1]_{m,\lambda} \tag{2.33}$$

with $M = 2\sum_\lambda C_\lambda/\tau_\lambda$ and $c = 1$ if $m = 0$, or $c = 2$ if $m \neq 0$.

Matrix formulation

To explicitly show the role of the coefficients $\vec{P}, \vec{B}$ at the interface between layers α and $\alpha + 1$, we write the boundary conditions as a matrix equation (in block matrix form),

$$\begin{bmatrix} \mathbf{a}^{(\alpha)} & \mathbf{b}^{(\alpha+1)} \\ \mathbf{c}^{(\alpha)} & \mathbf{d}^{(\alpha+1)} \end{bmatrix} \begin{bmatrix} B^{(\alpha)} \\ P^{(\alpha+1)} \end{bmatrix} = \begin{bmatrix} \mathbf{e}^{(\alpha+1)} & 0 \\ \mathbf{f}^{(\alpha+1)} & 0 \end{bmatrix} \begin{bmatrix} B^{(\alpha+1)} \\ P^{(\alpha+2)} \end{bmatrix} + \begin{bmatrix} 0 & \mathbf{g}^{(\alpha)} \\ 0 & \mathbf{h}^{(\alpha)} \end{bmatrix} \begin{bmatrix} B^{(\alpha-1)} \\ P^{(\alpha)} \end{bmatrix} . \tag{2.34}$$

The two rows of the matrix correspond to the boundary conditions given by Eq. (2.27). A schematic showing the organization of the equations are shown in Fig. 2.2, and explicit expressions for blocks **a** through **h** can be obtained from equations in the previous sections.

Incorporation of symmetries

Determining the unknown coefficients $(\vec{B}^{(\alpha)}, \vec{P}^{(\alpha+1)})$ requires inversion of the matrix $(\mathbf{abcd})$. The computational cost scales like $O(N_{\text{ph}}^3)$, and N_{ph} is proportional to the number of points in reciprocal space needed to accurately represent the bulk material's band structure. The data provided to us by Lindsay already discretizes the Brillouin zone using a Gaussian quadrature grid [2, 55, 56] for computing phonon-phonon scattering rates, so it is not likely that coarser discretization can be used. Thus, to further reduce the cost of the calculation, we use symmetry to consolidate the phonon modes. First, we only consider the irreducible wedge of the Brillouin zone. Then, we account for rotational symmetry about the x-axis by grouping terms with wavevectors $(k_x, k_y, k_z) = (k_x, k_z, k_y)$. We also do not distinguish between otherwise equivalent modes by polarization. Modes are considered to be degenerate if the modal energies are within $v_{gx}\Delta k$ of each other, where Δk is the difference in k_x for adjacent k-points in the Brillouin zone mesh. This consolidation is accounted for in the weighting used when taking the sum over all the phonon modes.

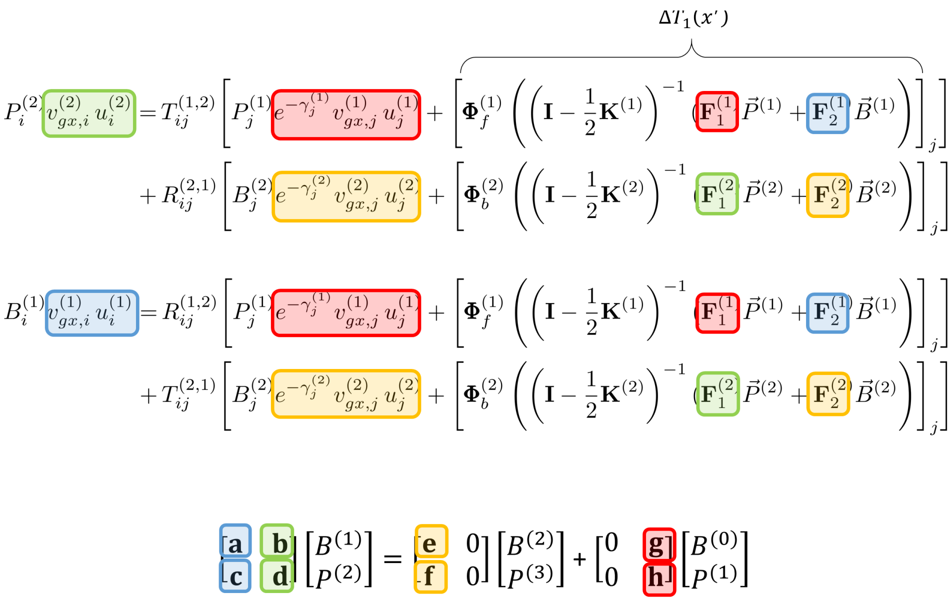

Figure 2.2: Schematic indicating how Eq. (2.31) can be written as a matrix equation.

Partially specular boundary conditions

Our modal approach allows us to account for reflection and transmission between an arbitrary set of phonons of the same frequency; therefore, we can also consider diffuse, specular, and partially specular interfaces. We neglect any anharmonic couplings across the interface. For diffuse transmission, phonon scattering only needs to satisfy energy conservation (all involved ω must be the same). For specular transmission, phonons must satisfy transverse momentum conservation (matching in k_y, k_z) in addition to energy conservation. However, if the reflection or transmission is completely diffuse, the block matrix (**abcd**) becomes singular and one cannot solve for $\Delta T(\hat{x})$. So, to prevent this problem, we define separate sets of coefficients for the specular problem ($\vec{P}_s, \vec{B}_s$) and the diffuse problem ($\vec{P}_d, \vec{B}_d$). Diffuse coefficients $\vec{P}_d$ and $\vec{B}_d$ each only contain N_{freq} unknown variables, where $N_{\text{freq}} < N_{\text{ph}}$ is the number of frequency bins used.

We define the partial specularity for frequency bin ω as p_ω with respect to the deviational distribution of the phonon mode as

$$p_\omega = \frac{\sum_{\lambda\in\omega} P_{s,\lambda}}{\sum_{\lambda\in\omega} P_{s,\lambda} + P_{d,\omega_i}} . \tag{2.35}$$

A similar expression can be defined for backwards propagating modes. The summations over $\lambda \in \omega$ mean that the sum includes phonons within the frequency bin corresponding to ω.

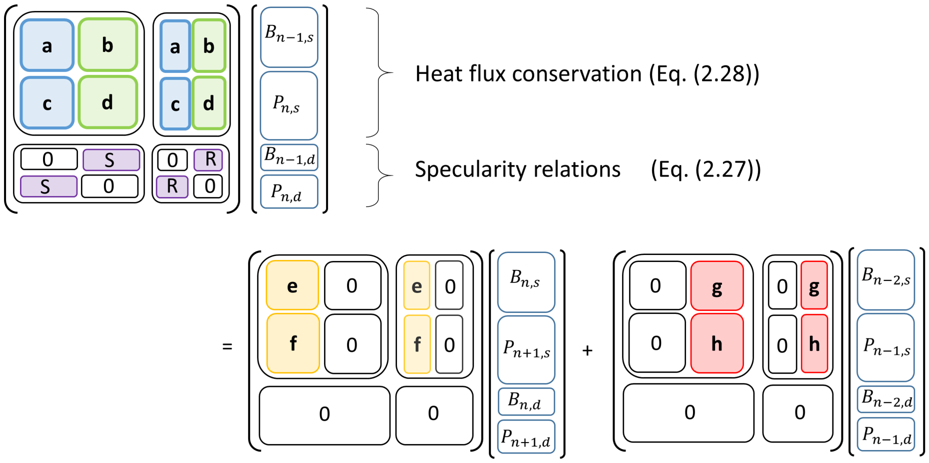

Figure 2.3: Schematic indicating how matrices are modified to incorporate partial specularity. Constraints from boundary conditions of the interface are given by Eq. (2.36), and the constraints from the definition of specularity are given by Eq. (2.35) from which define block matrices R and S.

Using these specularity constraints, in addition to the conservation of heat flux at the interface as described in the previous section, we can solve for the specular and diffuse coefficients. Details of the extended block matrix system of equations to account for specularity are described below and summarized in Fig. 2.3.

To account for both specular and diffuse reflection and transmission, the interface heat flux boundary conditions can be written as

$$\begin{aligned}
&P^{(2)}_{s,i} v^{(2)}_{gx,i} u^{(2)}_i + P^{(2)}_{d,i} \sum_{\lambda \in \omega_i} v^{(2)}_{gx,\lambda} u^{(2)}_\lambda = \\
&\quad T^{(1,2)}_{s,ij} \left[P^{(1)}_{s,j} e^{-\gamma^{(1)}_j} v^{(1)}_{gx,j} u^{(1)}_j + \left[\mathbf{\Phi}^{(1)}_f \left(\left(\mathbf{I} - \frac{1}{2}\mathbf{K}^{(1)} \right)^{-1} (\mathbf{F}^{(1)}_{1,s} \vec{P}^{(1)}_s + \mathbf{F}^{(1)}_{2,s} \vec{B}^{(1)}_s) \right) \right]_j \right] \\
&\quad + T^{(1,2)}_{d,ij} \left[P^{(1)}_{d,j} \sum_{\lambda \in \omega_j} e^{-\gamma^{(1)}_\lambda} v^{(1)}_{gx,\lambda} u^{(1)}_\lambda \right. \\
&\qquad\qquad \left. + \left[\mathbf{\Phi}^{(1)}_f \left(\left(\mathbf{I} - \frac{1}{2}\mathbf{K}^{(1)} \right)^{-1} (\mathbf{F}^{(1)}_{1,d} P^{(1)}_d + \mathbf{F}^{(1)}_{2,d} \vec{B}^{(1)}_d) \right) \right]_j \right] \\
&\quad + R^{(2,1)}_{s,ij} \left[B^{(2)}_{s,j} e^{-\gamma^{(2)}_j} v^{(2)}_{gx,j} u^{(2)}_j + \left[\mathbf{\Phi}^{(2)}_b \left(\left(\mathbf{I} - \frac{1}{2}\mathbf{K}^{(2)} \right)^{-1} (\mathbf{F}^{(2)}_{1,s} \vec{P}^{(2)}_s + \mathbf{F}^{(2)}_{2,s} \vec{B}^{(2)}_s) \right) \right]_j \right] \\
&\quad + R^{(2,1)}_{d,ij} \left[B^{(2)}_{d,j} \sum_{\lambda \in \omega_j} e^{-\gamma^{(2)}_\lambda} v^{(2)}_{gx,\lambda} u^{(2)}_\lambda \right. \\
&\qquad\qquad \left. + \left[\mathbf{\Phi}^{(2)}_b \left(\left(\mathbf{I} - \frac{1}{2}\mathbf{K}^{(2)} \right)^{-1} (\mathbf{F}^{(2)}_{1,d} \vec{P}^{(2)}_d + \mathbf{F}^{(2)}_{2,d} \vec{B}^{(2)}_d) \right) \right]_j \right]
\end{aligned} \tag{2.36}$$

where the subscripts s and d correspond to specular and diffuse scattering, respectively. The summations over $\lambda \in \omega_i$ mean that the sum includes phonons of frequency bin ω_i. The elements in $F_{b,s}$ for specular scattering are the same as defined in Eq. (2.24). The elements in the corresponding matrices for diffuse scattering, $F_{b,d}$, are defined as $[F_{b,d}]_{m,i} = \sum_{\lambda \in \omega_i} [F_b]_{m,\lambda}$.

Recall that $\vec{P}_s$ and $\vec{B}_s$ contain N_{ph} elements; $\vec{P}_d$ and $\vec{B}_d$ contain N_{freq} elements, where N_{freq} is the number of frequency bins. Then, $\boldsymbol{T}^{(1,2)}_s$ is a $N_{\text{ph},2} \times N_{\text{ph},1}$ matrix and $\boldsymbol{T}^{(1,2)}_d$ is a $N_{\text{ph},2} \times N_{\text{freq},1}$ matrix. Similarly, $\boldsymbol{R}^{(1,2)}_s$ is a $N_{\text{ph},1} \times N_{\text{ph},1}$ matrix and $\boldsymbol{R}^{(1,2)}_d$ is a $N_{\text{ph},1} \times N_{\text{freq},1}$ matrix. The diffuse reflection and transmission matrices describe how the collective set of phonons with some energy scatter into each other. In essence, they perform an averaging operation on the incident phonons.

A similar expression can be found for the $\vec{B}^{(1)}$ coefficients that corresponds to the phonons propagating away from the interface.

Periodic boundary conditions

To consider binary superlattices of infinite thickness, we must apply periodic boundary conditions at the two ends of a single unit cell. With periodic boundary conditions, the deviational phonon energy distribution at the boundaries is defined to be periodic [57, 58], meaning that the coefficients $\vec{P}$ and $\vec{B}$ are also periodic. However, the temperature profile in each unit cell is not periodic. As a result, the black-body phonon radiation contribution $C_\lambda v_{gx,\lambda} T_0$ is also different for each unit cell, and the difference must be included at the boundaries.

More specifically, let $\Delta T_0 = \Delta T_L - \Delta T_R$ denote the temperature difference between two adjacent unit cells, or equivalently, the temperature difference imposed at the ends of the unit cell. Then, the deviational heat fluxes at the interface between layers 2 and 3 are related to the deviational heat fluxes at the interface between layers 0 and 1 by

$$\vec{q}^{\,(3),+}(\hat{x}^{(3)} = 0) = \vec{q}^{\,(1),+}(\hat{x}^{(1)} = 0) + \left(\vec{C}^{(1)}\vec{v}_{gx}^{(1)}\right)\Delta T_0 \tag{2.37a}$$

$$\vec{q}^{\,(2),-}(\hat{x}^{(2)} = 1) = \vec{q}^{\,(0),-}(\hat{x}^{(0)} = 1) + \left(\vec{C}^{(2)}\vec{v}_{gx}^{(2)}\right)\Delta T_0 \ . \tag{2.37b}$$

Combining the above with Eq. (2.27) for heat flux conservation at the interface and rewriting all the components in terms of values in layers 1 and 2, we obtain the boundary conditions

$$\begin{aligned} \vec{q}^{\,(1),+}(x^{(1)} = 0) + \left(\vec{C}^{(1)}\vec{v}_{gx}^{(1)}\right)\Delta T_0 = & \qquad \qquad (2.38a) \\ & \boldsymbol{T}^{(2,1)}\,\vec{q}^{\,(2),+}(x^{(2)} = L^{(2)}) \\ & + \boldsymbol{R}^{(1,2)}\left[\vec{q}^{\,(1),-}(x^{(1)} = 0) + \left(\vec{C}^{(1)}\vec{v}_{gx}^{(1)}\right)\Delta T_0\right] \\ \vec{q}^{\,(2),-}(x^{(2)} = 0) = & \qquad \qquad (2.38b) \\ & \boldsymbol{R}^{(2,1)}\vec{q}^{\,(2),+}(x^{(2)} = L^{(2)}) \\ & + \boldsymbol{T}^{(1,2)}\left[\vec{q}^{\,(1),-}(x^{(1)} = 0) + \left(\vec{C}^{(1)}\vec{v}_{gx}^{(1)}\right)\Delta T_0\right] \ . \end{aligned}$$

For a binary superlattice, there are two interfaces: one in the middle (between layers (1) and (2)) with boundary conditions described by Eq. (2.27), and one at which the periodic boundary condition is applied (between layers (0) and (1)), as given by Eq. (2.38). These two boundary conditions provide a system of two matrix equations with two unknown vectors,

$$\begin{bmatrix} \mathbf{a}^{(1)} & \mathbf{b}^{(2)} \\ \mathbf{c}^{(1)} & \mathbf{d}^{(2)} \end{bmatrix} \begin{bmatrix} B^{(1)} \\ P^{(2)} \end{bmatrix} = \begin{bmatrix} \mathbf{e}^{(2)} & \mathbf{g}^{(1)} \\ \mathbf{f}^{(2)} & \mathbf{h}^{(1)} \end{bmatrix} \begin{bmatrix} B^{(2)} \\ P^{(1)} \end{bmatrix} \tag{2.39a}$$

$$\begin{bmatrix} \mathbf{a}^{(2)} & \mathbf{b}^{(1)} \\ \mathbf{c}^{(2)} & \mathbf{d}^{(1)} \end{bmatrix} \begin{bmatrix} B^{(2)} \\ P^{(1)} \end{bmatrix} = \begin{bmatrix} \mathbf{e}^{(1)} & \mathbf{g}^{(2)} \\ \mathbf{f}^{(1)} & \mathbf{h}^{(2)} \end{bmatrix} \begin{bmatrix} B^{(1)} \\ P^{(2)} \end{bmatrix} . \tag{2.39b}$$

After solving for the coefficients $\vec{B}^{(1)}$, $\vec{P}^{(1)}$, $\vec{B}^{(2)}$, and $\vec{P}^{(2)}$, the thermal conductivity can be calculated by inserting them into Eq. (2.14a) and Eq. (2.14b), and then using Eq. (2.16) and Eq. (2.17). To find the temperature profile across one unit cell of the superlattice, the coefficients are inserted into Eq. (2.20).

Summary of the calculation

In summary, the steps for solving the thermal conductivity and temperature profile for a binary superlattice with periodic boundary conditions are as follows. First, one uses Eq. (2.23a) and Eq. (2.24) to obtain the matrices in Eq. (2.20). Then, one builds the block matrix system of equations (Eq. (2.34)) describing the boundary conditions at the interface within the unit cell (Eq. (2.27)) and the interface between two unit cells (Eq. (2.38)). With these two matrix equations, we then solve for the unknown coefficients $P_\lambda^{(1)}$, $B_\lambda^{(1)}$, $P_\lambda^{(2)}$, and $B_\lambda^{(2)}$. Using these coefficients, we can obtain $g_\lambda(x)$ and then use Eq. (2.16) and Eq. (2.17) to obtain the thermal conductivity.

2.6 Calculations for Toy Models

Here, we present our calculations of the thermal conductivity of binary 1D superlattices with periodic boundary conditions. We define the superlattice to have layers of equal thickness L. We also assume that both constituent materials are silicon, giving a Si/Si superlattice; this is a reasonable approximation when the lattice spacing and dispersion of the two materials in the SL are similar. Making this approximation simplifies the definition of the transmission and specularity at the interface, allowing us to investigate how these interface parameters affect the superlattice thermal conductivity. Since we are working in the particle limit, these interface parameters are independent of superlattice period.

The full ab-initio phonon dispersions and lifetimes for crystalline Si are obtained using density functional perturbation theory courtesy of Dr. Lucas Lindsay. The data contains 2048 data points per phonon branch in the irreducible Brillouin zone. The dispersion relation can be found in the appendix of Ref. [2]. In our thermal conductivity calculations, we assume that the superlattices are oriented in the [100] direction.

Uniform Transmission Coefficients

We first consider the cases where (1) specular transmission is unity for all modes (in accordance with the acoustic mismatch model, AMM), and (2) diffuse transmission is 0.5 for all modes (in accordance with the diffuse mismatch model, DMM). The test cases of purely specular transmission ($p^\omega = 1$) and purely diffuse transmission ($p^\omega = 0$) provide evidence that the calculation is working properly. If the interfaces transmit phonons perfectly specularly, the interfaces pose no resistance to heat flow and the thermal conductivity should be independent of SL period. On the other hand, if the interfaces are perfectly diffuse, the thermal conductivity decreases with decreasing period due to interface scattering, consistent with the well-known classical size effects [59]. These two results are indeed observed in Fig. 2.4a. Clearly, neither of these cases exhibit a non-monotonic trend of thermal conductivity with superlattice layer thickness L.

We next investigate the behavior with partial specularity. For the first partially specular case, we use Ziman's definition of specularity [60],

$$p_\omega = \sum_{\lambda \in \omega} \exp(-4\eta^2 k_{x,\lambda}^2) \tag{2.40}$$

where η is the interface roughness chosen to be 0.8 Å so that the thermally occupied modes exhibit a broad range of specularities. In this case, we find that κ decreases with L, similar to the purely diffuse case, but has a higher overall thermal conductivity and decreases more slowly. The higher thermal conductivity is due to the fact that some phonons still transmit specularly, and the slower decrease arises from a lower effective interface resistance.

Recently, it was suggested that by defining the specularity in relation to an interface density of states, one can more accurately predict the phonon transmission profile through the interface [61]. This choice of specularity would still exhibit the same thermal conductivity trend as one decreases superlattice layer thickness. As L is decreased, phonons with non-unity transmission contribute less to thermal conductivity while phonons with near-unity transmission dominate the thermal conductivity. Since the interface density of states is independent of L in the present formalism, there is no mechanism by which the thermal conductivity could increase at smaller L.

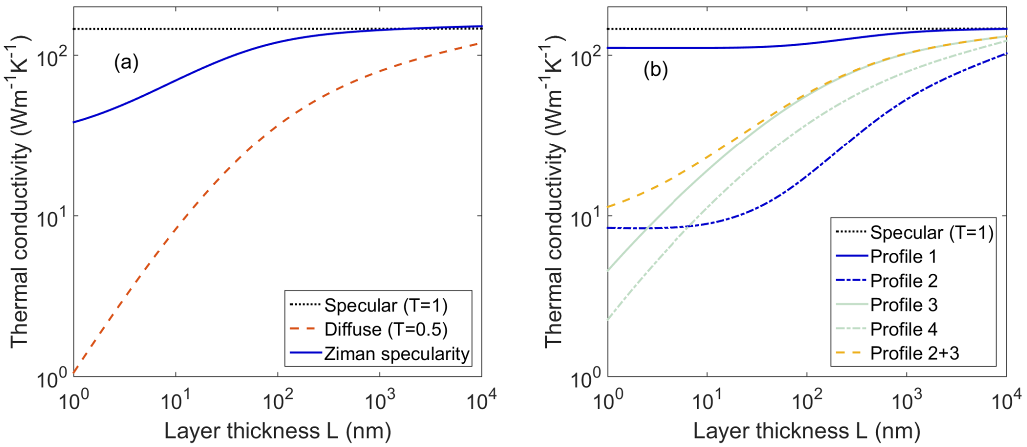

Figure 2.4: Thermal conductivity versus layer thickness L, (a) assuming (dotted black) specular transmission with unity transmission, (dot-dash red) diffuse transmission with 50% transmission, in accordance with DMM, (solid blue) and partially specular transmission with Ziman specularity assuming a roughness 0.8 Å. For partially specular scattering, considering transmission with and without mode conversion yielded no discernible differences. (b) Results assuming unity specularity, for the non-uniform transmission profiles: [[1]] (solid blue) a low pass frequency filter $T^{\mathrm{LP}}(\omega; 0.3)$, [[2]] (dot-dash blue) a high pass frequency filter $T^{\mathrm{HP}}(\omega; 0.6)$, [[3]] (solid light gray) a filter that preferentially transmits normally incident modes $T^{\perp}(k; 1)$, [[4]] (dot-dash light gray) a filter that preferentially transmits angled-incidence modes $T^{\parallel}(k; 1)$, and [[5]] (dashed yellow) a combination of profiles 2 and 3. Phonons with $\omega > 0.6\,\omega_{\mathrm{max}}$ have unity transmission and phonons with $\omega < 0.6\,\omega_{max}$ are filtered by incident angle according to $T^{\perp}(k; 1)$. For reference, the bulk conductivity (equivalent to an interface with unity transmission and specularity) is shown in the dotted black line.

Non-uniform Transmission Coefficients

In this section, we assume specular but non-unity transmission coefficients that vary with angle of incidence and phonon frequency. In particular, we consider frequency filters that would emulate a mismatch between phonon density of states and angle-dependent filters that would emulate an impedance mismatch, as described by the equations

$$T^{\mathrm{LP}}(\omega; a) = \Theta(\omega - a\,\omega_{\mathrm{max}}) \tag{2.41a}$$

$$T^{\perp}(k; b) = 1 - b\,(1 - |k_x|/|k|) \tag{2.41b}$$

$$T^{\mathrm{HP}}(\omega; a) = 1 - \Theta(\omega - a\,\omega_{\mathrm{max}}) \tag{2.42a}$$

$$T^{\parallel}(k; b) = b\,(1 - |k_x|/|k|) \tag{2.42b}$$

where Θ is the Heaviside step function and a and b are constant parameters between 0 and 1 (specified in the caption of Fig. 2.4). The reflection and transmission profiles given by Eq. (2.41) are physically motivated, as the low-pass (LP) frequency filter (Eq. (2.41a)) corresponds to materials with overlapping density of states for low frequency acoustic modes near the Γ point, while preferential transmission of phonons at normal incidence (Eq. (2.41b)) is the intuitive expectations of wave reflection and transmission as in Snell's law. The second set of equations (Eq. (2.42)) are less physically motivated as the frequency filter is a high-pass (HP) and the wave-vector filter preferentially transmits phonons at shallow incident angles.

The thermal conductivity versus layer thickness is shown in Fig. 2.4b. In the case of the frequency filters, as L decreases, the thermal conductivity first decreases, but then reaches a plateau. This plateau occurs because of the phonons that propagate without reflection. The LP filter results in a plateau at a higher thermal conductivity than the HP filter since low frequency phonons contribute more to thermal conductivity than the high frequency optical modes. In the case of the incident angle filters, as L decreases, the thermal conductivity continues to decrease, as only normally incident phonon modes (if $T^{\perp}$) or phonons parallel to the interface (if $T^{\|}$) are able to propagate without reflection. In all cases, the thermal conductivity does not exhibit a minimum as a function of L.

Though we only showed a few sample transmission and reflection coefficient choices, more general transmission coefficients can be obtained using superpositions of the filters. For example, Profile 5 (yellow curve) in Fig. 2.4b corresponds to the thermal conductivity for a transmission profile that follows $T^{\perp}(k;1)$ for phonon frequencies below 0.3 ω_{max} and otherwise has unity transmission. The resulting thermal conductivity also does not exhibit a minimum. One can build a variety of other transmission profiles of various shapes using the proposed phonon filters given in Eq. (2.41) and Eq. (2.42). However, since the thermal conductivity always is non-increasing with decreasing L, regardless of the phonon filter, we will not be able to identify a transmission profile that will generate a non-monotonic thermal conductivity trend.

One can also include the possibility of partially specular transmission using a similar analysis. As L decreases, the thermal conductivity will initially decrease as the phonons reflect from the interface more frequently. At some value of L, phonons with specular and near-unity transmission coefficients dominate the thermal conductivity and the thermal conductivity becomes independent of L. Therefore, in the particle picture, there is no obvious physical mechanism for the thermal conductivity to increase at smaller L.

Temperature dependence of thermal conductivity

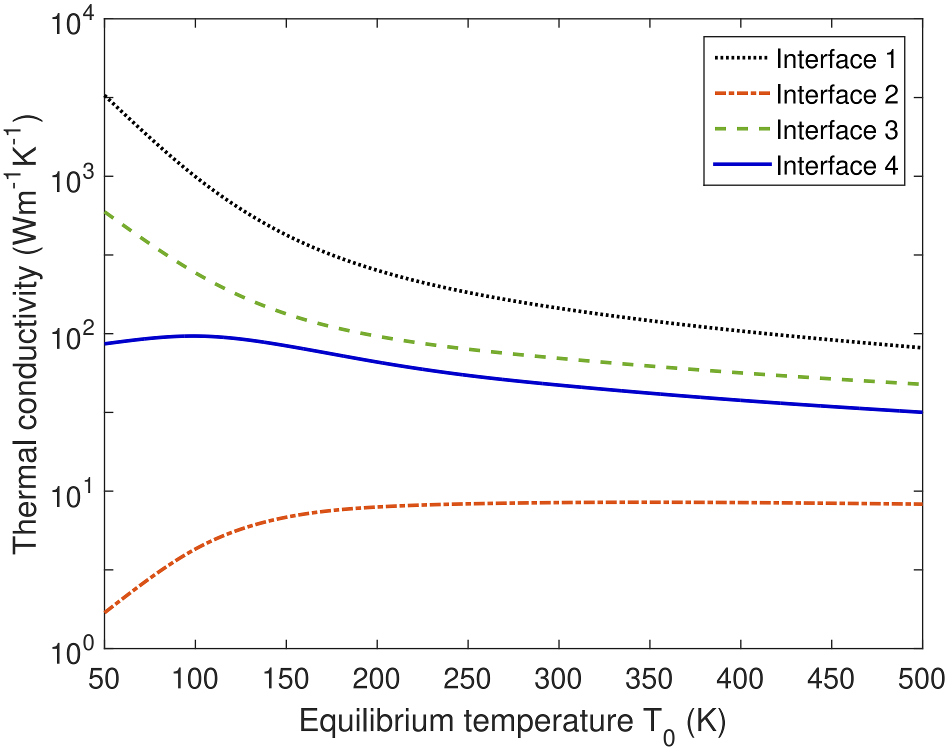

Figure 2.5: Thermal conductivity versus temperature for several different superlattices. We consider the following interfaces: [[1]] (dotted black) unity specularity with unity transmission, [[2]] (dot-dash red) diffuse transmission coefficients with a value of 0.5, [[3]] (dashed green) Ziman specularity with roughness of 0.8 Å, [[4]] (solid blue) angle-dependent reflectivity (b = 0.05) with unity specularity. The layer thickness L is 10 nm.

Some experimental works have also looked at the temperature dependence of the thermal conductivity to assess the role of phonon coherence on thermal conductivity [20]. We too calculate the temperature dependence for several of the transmission profiles shown above, and present the results in Fig. 2.5.

We find that the thermal conductivity trend with respect to temperature qualitatively varies significantly depending on the properties of the interface. As expected, systems with unity transmission exhibit higher thermal conductivities at lower temperatures due to the longer phonon lifetimes. In contrast, systems with non-unity transmission may exhibit lower thermal conductivities at lower temperatures, depending on the transmission profile. In particular, reduction of thermal conductivity can occur when low-energy phonons have low probabilities of transmission at the interface (e.g. all phonons in the case of Interface 2, and the angled phonons in the case of Interface 4, as defined in the caption of Fig. 2.5). Therefore, while measuring thermal conductivity with respect to ambient temperature can provide some insight on the transmissivity of the phonons at each interface, making definitive conclusions on the role of phonon coherence in thermal transport is challenging.

2.7 Discussion

In summary, we have reported a numerical method to solve the Boltzmann transport equation with ab-initio phonon properties for a 1-D superlattices with modal transmission coefficients. Applying this method to thermal transport in superlattices, we find that the BTE is still unable to predict the existence of a thermal conductivity minimum with respect to SL period. Our results are consistent with the description of interfaces as thermal resistors in the particle limit, though by including modal dependencies, the thermal conductivity can plateau at some minimum value determined by the phonons that are transmitted through the SL without scattering.

However, observing an increase in thermal conductivity at even smaller layer thickness is not possible, and our study thus supports the interpretation that phonon coherence plays a role in recent experimental studies of thermal transport in binary superlattices that exhibit such behavior.

References

[1] D. A. Broido, M. Malorny, G. Birner, N. Mingo, and D. A. Stewart, “Intrinsic lattice thermal conductivity of semiconductors from first principles,” Appl. Phys. Lett. **91**, 231922 (2007).

[2] L. Lindsay, D. A. Broido, and T. Reinecke, “Ab initio thermal transport in compound semiconductors,” Phys. Rev. B , 165201 (2013).

[3] A. J. N. McGaughey, A. Jain, H.-Y. Kim, and B. Fu, “Phonon properties and thermal conductivity from first principles, lattice dynamics, and the boltzmann transport equation,” J. Appl. Phys. **125**, 011101 (2019).

[4] M. Zebarjadi, K. Esfarjani, M. S. Dresselhaus, Z. F. Ren, and G. Chen, “Perspectives on thermoelectrics: from fundamentals to device applications,” Royal Soc. Chem. **5**, 5147–5162 (2012).

[5] C. J. Vineis, A. Shakouri, A. Majumdar, and M. G. Kanatzidis, “Nanostruc-

tured thermoelectrics: Big efficiency gains from small features," Advanced Mater. **22**, 3970–3980 (2010).

[6] G. J. Snyder and E. S. Toberer, "Complex thermoelectric materials," Nature Materials **7**, 105–114 (2008).

[7] D. G. Cahill, P. V. Braun, G. Chen, D. R. Clarke, S. Fan, K. E. Goodson, P. Keblinski, W. P. King, G. D. Mahan, A. Majumdar, H. J. Maris, S. R. Phillpot, E. Pop, and L. Shi, "Nanoscale thermal transport. ii. 2003–2012," Appl. Phys. Rev. **1**, 011305 (2014).

[8] Y. Pennec, J. O. Vasseur, B. Djafari-Rouhani, L. Dobrzynski, and P. Deymier, "Two-dimensional phononic crystals: Examples and applications," Surf. Sci. Rep. **65**, 229–291 (2010).

[9] S. Yang, J. H. Page, Z. Liu, M. L. Cowan, C. T. Chan, and P. Sheng, "Focusing of sound in a 3d phononic crystal," Phys. Rev. Lett. **93**, 024301 (2004).

[10] A. A. Maznev, O. B. Wright, and M. O., "Mapping the band structure of a surface phononic crystal," New J. Phys. **13**, 013037 (2011).

[11] C. Colvard, R. Merlin, M. V. Klein, and A. C. Gossard, "Observation of folded acoustic phonons in a semiconductor superlattice," Phys. Rev. Lett. **45**, 298–301 (1980).

[12] V. Narayanamurti, H. Stormer, M. A. Chin, A. C. Gossard, and W. Wiegmann, "Selective transmission of high-frequency phonons by a superlattice: the "dielectric" phonon filter," Phys. Rev. Lett. **43**, 2012–2016 (1979).

[13] N. Zen, T. A. Puurtinen, T. J. Isotalo, S. Chaudhuri, and I. J. Maasilta, "Engineering thermal conductance using a two-dimensional phononic crystal," Nature Communications **5**, 3435 (2014).

[14] M. Maldovan, "Phonon wave interference and thermal bandgap materials," Nature Materials **14**, 667–674 (2015).

[15] S. M. Lee, D. G. Cahill, and R. Venkatasubramanian, "Thermal conductivity of Si-Ge superlattices," Appl. Phys. Lett. **70**, 2957 (1997).

[16] B. Saha, Y. R. Koh, J. Comparan, S. Sadasivam, J. L. Schroeder, M. Garbrecht, A. Mohammed, J. Birch, T. Fisher, A. Shakouri, and T. D. Sands, "Cross-plane thermal conductivity of (Ti,W)N/(Al,Sc)N metal/semiconductor superlattices," Phys. Rev. B **93**, 045311 (2016).

[17] J. Ravichandran, A. K. Yadav, R. Cheaito, P. B. Rossen, A. Soukiassian, S. Suresha, J. C. Duda, B. M. Foley, C.-H. Lee, Y. Zhu, A. W. Lichtenberger, J. E. Moore, D. A. Muller, D. G. Schlom, P. E. Hopkins, A. Majumdar, R. Ramesh, and M. A. Zurbuchen, "Crossover from incoherent to coherent phonon scattering in epitaxial oxide superlattices," Nature Mater. **13**, 168–172 (2014).

[18] W. Ren, H. Li, L. Gao, Z. Zhang, C. Long, H. Ji, X. Niu, Y. Lin, and Z. Wang, "Epitaxial Growth and thermal conductivity limit of single-crystalline Bi2Se3/In2Se3 superlattices on mica," Nano Research **10**, 247–254 (2018).

[19] R. Venkatasubramanian, "Lattice thermal conductivity reduction and phonon localization-like behavior in superlattice structures," Phys. Rev. B **61**, 3091–3097 (2000).

[20] M. N. Luckyanova, J. Garg, K. Esfarjani, A. Jandl, M. T. Bulsara, A. J. Schmidt, A. J. Minnich, S. Chen, M. S. Dresselhaus, Z. Ren, E. A. Fitzgerald, and G. Chen, "Coherent phonon heat conduction in superlattices," Science **16**, 936–939 (2012).

[21] R. Cheaito, C. A. Polanco, S. Addamane, J. Zhang, A. W. Ghosh, G. Balakrishnan, and P. E. Hopkins, "Interplay between total thickness and period thickness in the phonon thermal conductivity of superlattices from the nanoscale to the microscale: coherent vs incoherent phonon transport," Phys. Rev. B **97**, 085306 (2018).

[22] M. V. Simkin and G. D. Mahan, "Minimum thermal conductivity of superlattices," Phys. Rev. Lett. **84**, 927–930 (2000).

[23] J. Garg and G. Chen, "Minimum thermal conductivity in superlattices: A first-principles formalism," Phys. Rev. B **87**, 140302 (2013).

[24] J. Garg, N. Bonini, and N. Marzari, "High thermal conductivity in short-period superlattices," Nano Lett. **11**, 5135–5141 (2011).

[25] W. Zhang, T. S. Fisher, and N. Mingo, "The atomistic green's function method: an efficient simulation approach for nanoscale phonon transport," Numer. Heat Tr. B-Fund. **51**, 333–349 (2007).

[26] Z. Tian, K. Esfarjani, and G. Chen, "Enhancing phonon transmission across a Si/Ge interface by atomic roughness: First-principles study with the green's function method," Phys. Rev. B **86**, 235304 (2012).

[27] Y. Chen, D. Li, J. R. Lukes, Z. Ni, and M. Chen, "Minimum superlattice thermal conductivity from molecular dynamics," Phys. Rev. B **72**, 174302 (2005).

[28] B. Latour, S. Volz, and Y. Chalopin, "Microscopic description of thermal-phonon coherence: from coherent transport to diffuse interface scattering in superlattices," Phys. Rev. B **90**, 014307 (2014).

[29] R. Frieling, M. Radek, S. Eon, H. Bracht, and D. E. Wolf, "Phonon coherence in isotopic silicon superlattices," Appl. Phys. Lett. **105**, 132104 (2014).

[30] Y. Wang, H. Huang, and X. Ruan, "Decomposition of coherent and incoherent phonon conduction in superlattices and random multilayers," Phys. Rev. B **90**, 165406 (2014).

[31] X.-K. Chen, Z.-X. Xie, W.-X. Zhou, L.-M. Tang, and K.-Q. Chen, “Phonon wave interference in graphene and boron nitride superlattice,” Appl. Phys. Lett. **109**, 023101 (2016).

[32] A. Giri, P. E. Hopkins, J. G. Wessel, and J. C. Duda, “Kapitza resistance and the thermal conductivity of amorphous superlattices,” J. Appl. Phys. **118**, 165303 (2015).

[33] A. France-Lanord, S. Merabia, T. Albaret, D. Lacroix, and K. Termentzidis, “Thermal properties of amorphous/crystalline silicon superlattices,” J. Phys.: Condens. Matter **26**, 355801 (2014).

[34] J.-P. M. Peraud and N. G. Hadjiconstantinou, “Extending the range of validity of Fourier’s law into the kinetic transport regime via asymptotic solution of the phonon BTE,” Phys. Rev. B **93**, 045424 (2016).

[35] J. Kaiser, T. Feng, J. Maassen, X. Wang, X. Ruan, and M. Lundstrom, “Thermal transport at the nanoscale: A Fourier’s law vs. phonon boltzmann equation study,” J. Appl. Phys. **121**, 044302 (2017).

[36] D. Abarbanel and J. Maaseen, “Modeling quasi-ballistic transient thermal transport with spatially sinusoidal heating: A McKelvey-Shockley flux approach,” J. Appl. Phys. **121**, 204305 (2017).

[37] G. Chen and M. Neagu, “Thermal conductivity and heat transfer in superlattices,” Appl. Phys. Lett. **71**, 2761 (1997).

[38] G. Chen, “Thermal conductivity and ballistic-phonon transport in the cross-plane direction of superlattices,” Phys. Rev. B **57**, 14958 (1998).

[39] K. Esfarjani, G. Chen, and H. T. Stokes, “Heat transport in silicon from first-principles calculations,” Phys. Rev. B **84**, 085204 (2011).

[40] A. J. Minnich, “Advances in the measurement and computation of thermal phonon transport properties,” J. Phys.: Condens. Matter **27**, 053202 (2015).

[41] C. Hua and A. J. Minnich, “Semi-analytical solution to the frequency-dependent Boltzmann transport equation for cross-plane heat conduction in thin films,” J. Appl. Phys. **117**, 175306 (2015).

[42] C. Kittel, *Introduction to Solid State Physics*, 8th ed. (John Wiley & Sons, Inc, 2005).

[43] S. Baroni, S. de Gironcoli, A. D. Corso, and P. Giannozzi, “Phonons and related crystal properties from density functional perturbation theory,” Rev. Mod. Phys. **73**, 515–562 (2001).

[44] G. Deinzer, G. Birner, and D. Strauch, “Ab initio calculation of the linewidth of various phonon modes in germanium and silicon,” Phys. Rev. B **67**, 144304 (2003).

[45] M. Kardar, *Statistical Physics of Particles* (Cambridge University Press, 2007).

[46] W. A. Little, "The transport of heat between dissimilar solids at low temperatures," Can. J. Phys. **37**, 334–349 (1959).

[47] E. T. Swartz and R. O. Pohl, "Thermal boundary resistance," Rev. Mod. Phys. **61**, 605–668 (1989).

[48] P. Hyldgaard and G. D. Mahan, "Phonon superlattice transport," Phys. Rev. B **56**, 10754–10757 (1997).

[49] S. Plimpton, "Fast parallel algorithms for short-range molecular dynamics," J. Computational Phys. **117**, 1–19 (1995).

[50] D. N. Payton, M. Rich, and W. M. Visscher, "Lattice thermal conductivity in disordered harmonic and anharmonic crystal models," Phys. Rev. **160**, 706–711 (1967).

[51] B. C. Daly, H. J. Maris, K. Imamura, and S. Tamura, "Molecular dynamics calculations of the thermal conductivity of superlattices," Phys. Rev. B **66**, 024301 (2002).

[52] S. G. Volz and G. Chen, "Lattice dynamic simulation of silicon thermal conductivity," Physica B **263**, 709–712 (1999).

[53] S. G. Volz and G. Chen, "Molecular-dynamics simulation of thermal conductivity of silicon crystals," Phys. Rev. B **61**, 2651–2656 (2000).

[54] W. Lv and A. Henry, "Direct calculation of modal contributions to thermal conductivity via Green-Kubo analysis," New J. Phys. **18**, 013028 (2016).

[55] D. A. Broido, A. Ward, and N. Mingo, "Lattice thermal conductivity of silicon from empirical interatomic potentials," Phys. Rev. B **72**, 014308 (2005).

[56] L. Lindsay and D. A. Broido, "Three-phonon phase space and lattice thermal conductivity in semiconductors," J. Phys.: Condens. Matter **20**, 165209 (2008).

[57] Q. Hao, G. Chen, and M. S. Jeng, "Frequency-dependent Monte Carlo simulations of phonon transport in two-dimensional porous silicon with aligned pores," J. Appl. Phys. **106**, 114321 (2009).

[58] J.-P. M. Peraud and N. G. Hajiconstantinous, "Adjoint-based deviational Monte Carlo methods for phonon transport calculations," Phys. Rev. B **91**, 235321 (2015).

[59] G. Chen, *Nanoscale Energy Transport and Conversion: A Parallel Treatment of Electrons, Molecules, Phonons, and Photons* (Oxford University Press, 2005).

[60] J. M. Ziman, *Electrons and Phonons: The Theory of Transport Phenomena in Solids* (Oxford University Press, 1960).

[61] Y. Zhang, D. Ma, Y. Zang, X. Wang, and N. Yang, "A modified theoretical model to accurately account for interfacial roughness in predicting the interfacial thermal conductance," Front. in Energy Res. , 2018.00048 (2018).

Chapter 3

LOW-RANK APPROXIMATION OF ELECTRONIC STRUCTURE HAMILTONIAN

In this chapter, we rewrite the electronic structure Hamiltonian and unitary coupled cluster operator as a sum of 1- or 2-body terms that can be truncated in a systematic fashion. This decomposition is particularly interesting in the context of near-term quantum computing algorithms, as the Trotter step of a single term in the operator can be implemented efficiently on hardware with only 1-D connectivity [1, 2]. Furthermore, the systematic truncation allows one to easily reduce the number of terms needed to accurately represent the original operator within some error threshold, thereby reducing the computational cost even further. We find that for physically relevant systems, ie. systems that exhibit locality, if N is the number of orbitals in the quantum chemical system of interest, then we are able to reduce the number of terms in the sum from $O(N^4)$ to $O(N^3)$ while maintaining chemical accuracy.

The work in this chapter is presented in the paper

M. Motta, E. Ye, et al. "Low rank representations for quantum simulation of electronic structure," arXiv preprint quant-ph/1808.02625 (2018).

3.1 Introduction

Quantum computers (QC) were initially proposed by Feynman [3, 4] as a means to perform calculations on the high-dimensional problem of interacting quantum particles. Since that time, several fundamental quantum computing algorithms, such as phase estimation [5–7] and the quantum Fourier transform [8, 9], have been developed. These concepts form the basis of Shor's algorithm for factorization of primes, Grover's search algorithm and amplitude amplification, the Harrow-Hassidim-Lloyd alogrithm for solving linear systems of equations, and more [10]. These algorithms promise some degree of computational speed-up (ie. reduction in the scaling of the algorithm with respect to some parameter, usually problem size) compared to their classical counterparts. However, these algorithms require complex controlled operations and assume perfect, noiseless quantum computers with infinite coherence times, which is impractical. Schemes for error correction and fault-tolerant quantum computing have been developed, but often require an expensive step (such as implementing T-gates). As such, efficiently implementing quantum algorithms, such as the time evolution step in phase estimation [11–13], using some specific fault-tolerant quantum architecture is an active area of research.

Furthermore, though quantum computing hardware and controls are quickly improving for all potential hardware types (e.g. superconducting, ion-trapped, photonic), much more progress is needed for the above quantum algorithms to be of any practical use. In light of these hardware limitations, there has been a push to find problems that these "noisy, intermediate scale" quantum (NISQ) devices might be able solve, and quantum chemistry is believed to be one potential field of study. Quantum chemistry can roughly be split into two areas. One is to understand the electronic structure of molecules, which involves finding the eigenstates of the electronic structure Hamiltonian. The other is to understand the dynamics of a chemical system. Due to the exponential scaling of Hilbert space with respect to system size, solving these problems exactly for large molecules is intractable on classical computers. Common to many of these near-term algorithms are Trotter-Suzuki based methods for time-evolution (which break the evolution of a complex sum of operators into a sequence of Trotter steps each evolving only a single term in the sum).

In the context of quantum chemistry, the operators of interest are typically the Hamiltonian or unitary coupled cluster (uCC) operator, which are first represented in a single-particle basis of dimension N. However, depending on the basis chosen, such as the molecular orbital and active space bases common in electronic structure calculations, the operators are typically written as sums of 1, 2, and 4-body terms, the last of which cannot be easily implemented on near-term devices. Furthermore, in these bases, the Hamiltonian and cluster operator contain $O(N^4)$ second-quantized terms. This leads to at least $O(N^4)$ gate complexity for a single Trotter step [14, 15], a formidable barrier to practical progress in near-term devices. While complexity can be reduced using alternative bases [1, 16], such representations are not usually as compact as the molecular orbital one (ie. a longer basis expansion is required to represent typical physical states of interest). Thus, reducing the cost of the Trotter step for general bases is still an important goal.

We present a scheme that allows one to rewrite these 4-body terms as 2-body terms in rotated bases. Now that the operators are written as sums of smaller operators acting on at most 2 qubits at a time, each term in the Trotter step can be implemented efficiently on devices with at least linear connectivity with $O(N^2/2)$ entangling gates and $O(N)$ gate depth, using the algorithms presented in Refs. [1, 2]. A similar decomposition was presented by Poulin et al. [17], but our decomposition allows us to take advantage of the low-rank nature of the electronic structure Hamiltonian that arises from spatial locality in most physically relevant chemical systems. By performing systematic truncations of less important terms in the decomposition, one can reduce the number of 4-body terms from $O(N^4)$ to $O(N^3)$ (or even lower to $O(N^2)$ in the asymptotic limit of N), while maintaining chemical accuracy. Though this is not an exponential speed up, small reductions in computational cost are always welcome for near-term devices.

Though initially discussed for the implementation of Trotter steps, the low-rank decomposition of these operators can be utilized in many quantum algorithms. For example, most obviously, the exponentials of these operators can be used as initial guesses for the state in the variational quantum eigensolver (VQE) algorithm [18–21] and in the body of the quantum algorithm itself, such as in simulating system dynamics or in the phase estimation algorithm [7]. Furthermore, since the initial posting of this work on arXiv, there have been additional works evaluating the cost reduction of the decomposition in the context of other quantum computation algorithms such as qubitization, yielding different cost models [22, 23]. Others have used the double-nested factorized form to reduce the cost of measurements as well [24, 25].

3.2 Background of Related Technical Concepts

Electronic structure Hamiltonian

The Hamiltonian of a molecular system (in atomic units) is

$$H = -\sum_i \frac{1}{2}\nabla_i^2 - \sum_A \frac{1}{2m_A}\nabla_A^2 - \sum_{i,A} \frac{Z_A}{r_{iA}} + \sum_{i>j} \frac{1}{r_{ij}} + \sum_{A>B} \frac{Z_A Z_B}{R_{AB}} \tag{3.1}$$

where i, j index the electrons, A, B index the nuclei, Z_A is the charge of the nucleus A, m_A is the mass of the nucleus A, and r or R is the distance between two electrons or nuclei. The first two terms correspond to the kinetic energies (of the electrons and nuclei, respectively). The last three terms correspond to the Coulomb interactions between an electron and nucleus, two electrons, and two nuclei, respectively.

In the Born-Oppenheimer limit, motivated by the fact that the nuclei are much more massive than the electrons and move much more slowly, we can approximately treat the electronic wavefunction and nuclear wavefunction as separable. For electronic structure calculations, we are interested in solutions of the electronic part of the

Hamiltonian given some nuclear configuration. (This approximation breaks down when the energies of two nuclear configurations are close, which occurs at crossings of the potential energy surface.)

The Hamiltonian of interest is now

$$H_{\text{elec}} = -\frac{1}{2}\sum_i \nabla_i^2 - \sum_{i,A}\frac{Z_A}{r_{iA}} + \sum_{i>j}\frac{1}{r_{ij}} \ , \tag{3.2}$$

and we are interested in writing this in second quantized form. To do this, we choose a complete single particle basis set of N orbitals $\{\phi_i\}$ (typically obtained using Hartree-Fock) that can each either be occupied or unoccupied, and calculate the 1- and 2- particle interactions from the Hamiltonian

$$h_{pq} \equiv \langle\phi_p| H_{\text{elec}} |\phi_q\rangle \tag{3.3}$$

$$h_{pqrs} \equiv \langle\phi_p\phi_q| \frac{1}{r_{12}} |\phi_r\phi_s\rangle \ . \tag{3.4}$$

Note the because of the symmetry of the Coulomb interaction, h_{pqrs} is symmetric and therefore positive with respect to the exchanging of electron 1 and 2. The Hamiltonian in second quantized form is

$$H_{\text{elec}} = \sum_{pq} h_{pq}a_p^\dagger a_q + \sum_{pqrs} h_{pqsr}a_p^\dagger a_q^\dagger a_r a_s \tag{3.5}$$

where the $a_p^\dagger, a_p$ are the fermionic creation/annihilation operators for orbital p.

Unitary coupled cluster

Suppose that $\{|\phi_i\rangle\}$ is a complete basis set for single particle basis. Then, the complete basis of an n particle state is $\{|\phi_{i_1}, \phi_{i_2}, ...\phi_{i_n}\rangle\}$. One can represent the quantum state using Slater determinants containing the single particle orbitals along column, for each of the m electrons. One can then use Hartree-Fock to find the optimal $\{\phi_i\}$ such that the Slater determinant $|\Phi_0\rangle$ minimizes the Hamiltonian.

However, the true ground state may be a superposition of multiple Slater determinants. The coupled cluster ansatz is chosen to include determinants with single and double excitations while maintaining extensivity, and is defined as

$$|\psi\rangle = \exp\left(\sum_{ia} t_{ia}\, a_a^\dagger a_i + \sum_{i>j,a>b} t_{ijab}\, a_a^\dagger a_b^\dagger a_i a_j\right)|\Phi_0\rangle \equiv e^T\,|\Phi_0\rangle \tag{3.6}$$

where the $a_p^\dagger, a_p$ are the fermionic creation/annihilation operators for orbital p, and the coefficients t_{ai} and t_{abij} are found such that the energy of the quantum state is minimized.

The unitary coupled cluster is a similar ansatz, but is defined like

$$|\psi\rangle = e^{-i(T-T^{\dagger})}\,|\Phi_0\rangle \tag{3.7}$$

so that it is suitable for implemention on a quantum computer and can be used as an ansatz for the variational quantum eigensolver (VQE) algorithm, where the coefficients in T are variationally optimized to return the ground state.

However, at second-order perturbation theory in the electron-electron interaction, uCC amplitudes are $t_{abij} \propto \frac{\langle ji||ab\rangle}{\epsilon_a - \epsilon_j + \epsilon_b - \epsilon_i}$, where ϵ_p are the Hartree-Fock eigenvalues and $\langle ji||ab\rangle = h_{abij} - h_{abji}$ is the antisymmetrized electron repulsion integral. Antisymmetrization of the electron repulsion integral prevents from casting t onto a supermatrix indexed by orbitals pertaining to electrons 1 and 2 separately.

Trotter step with fermionic swap network

The fermionic swap network introduced in Ref. [1] was originally designed to implement Trotter steps of Hamiltonians of the form

$$H = \sum_{pq} T_{pq} a_p^{\dagger} a_q + \sum_p U_p n_p + \sum_{p \neq q} V_{pq} n_p n_q \tag{3.8}$$

which have at most 2-body interactions. Here p, q index one of the N orbitals, $a^{\dagger}, a$ are fermionic creation and annihilation operators, and n are number operators. T, U, and V are coefficients that are given.

Suppose we are interested in applying a Trotter step of the proposed Hamiltonian. Then the 1-qubit terms are simple phase gates that need to be applied to each qubit. The 2-qubit terms acting on qubits p and q can be written as

$$F(p,q) = e^{-iV_{pq} n_p n_q t} e^{-iT_{pq}(a_p^{\dagger} a_q + a_q^{\dagger} + a_p)t} \quad . \tag{3.9}$$

However, in general, p and q are not necessarily adjacent qubits, and most devices are limited to nearest neighbor connectivity. But if the positions of the qubits are swapped during the operation (using a fermionic swap gate $f_{\text{swap}}^{(p,q)}$), then one can ensure that qubits p and q are nearest neighbors at some point with $\binom{N}{2}$ swap operations. Thus, we modify the proposed 2-qubit gates to simultaneously implement the two body gate and swap the qubits using

$$\mathcal{F}(p,q) = F(p,q) f_{\text{swap}}^{(p,q)} = \begin{pmatrix} 1 & 0 & 0 & 0 \\ 0 & -i\sin(T_{pq}t) & \cos(T_{pq}t) & 0 \\ 0 & \cos(T_{pq}t) & -i\sin(T_{pq}t) & 0 \\ 0 & 0 & 0 & -e^{-iV_{pq}t} \end{pmatrix} \tag{3.10}$$

and the Trotter step of the Hamiltonian can be implemented using a quantum circuit containing $\binom{N}{2}$ two-qubit gates parallelized into N layers, plus a single layer of N single-qubit gates that can be applied simultaneously, as shown in Fig. 1 of Ref. [1].

By using our decomposition scheme and writing the electronic structure Hamiltonian in a similar 2-body interaction form, one can utilize this algorithm to efficiently implement Trotter steps of the Hamiltonian on a quantum computer.

Variational quantum eigensolver

The variational quantum eigensolver (VQE) is a hybrid classical-quantum algorithm in which one classically optimizes a parameterized ansatz such that the expectation value of some Hamiltonian is minimized [19]. Then, the optimal parameters define the ground state solution of the Hamiltonian of interest. Note that there are various extensions to VQE that allow one to search for excited states as well [26, 27]. Though it is believed that any circuit with a polynomial number of parameters is suitable, most works apply VQE to the unitary coupled cluster (uCC) ansatz [18, 20], which can be written as a product of exponentiated weighted operators. The weights in front of these operators act as the variational parameters.

These many-qubit gates are difficult to implement on a quantum computer, with an added layer of complexity if the quantum computer is limited to nearest neighbor connectivity. Thus, using the proposed decomposition to write the uCC ansatz as a series of two nearest neighbor qubit operations would simplify the costs of implementing the ansatz on a quantum computer. Furthermore, truncations in the decomposition suggest that one should be able to reduce the number of parameters that need to be optimized over.

Qubitization

Qubitization (or block encoding) [12], a generalization of the linear combination of unitaries (LCU) [11, 28], is an approach which determines the evolution of the Hamiltonian, written as a linear combination of unitaries $U = \sum_j w_j U_j$, using quantum signal processing [29].

As shown in [22], one can write the electronic structure Hamiltonian (in the proposed doubly-nested factorized form) as a linear combination of $L \sim O(N)$ unitaries, where again N is the number of orbitals in the system. Naive state preparation for the algorithm requires $O(N^2 L)$ Toffoli gates, though Ref. [22] obtains a scaling of $O(\sqrt{N^2 L \log(N^2/\varepsilon)})$ Toffoli gates, where ε is the target precision by incorporating reductions via symmetries and use of ancillas.

Quantum state measurement

Once the quantum state is prepared, one needs to make measurements in order to extract information from the state. In general, the Hamiltonian can be written as a sum of operators each acting on a subset of the particles in the system, and measuring its expectation value would require measuring the expectation values of each of the terms in the sum. However, the quantum state needs to be re-prepared for each set of non-commuting measurements, and measuring expectation values requires performing measurements of the same observable on the order of $O(1/\varepsilon^2)$ times, where ε is the target precision [24, 30, 31].

One obvious way to reduce costs is to separate terms into groups of commuting observables, so that all observables in each group can be measured simultaneously. The number of groups has been found to scale like $O(N^3)$ for a system with N qubits (see Ref. [24] for a thorough overview). However, the number of groupings themselves do not accurately reflect the number of circuit repetitions required for convergence of the expected values.

An additional complication with fermionic systems is that if the wavefunction antisymmetry is not already encoded in the qubits, then the fermionic algebra needs to be incorporated in the operators being measured, typically in the form of Jordan-Wigner strings that may require support over all N qubits. While there is no added complexity for measuring observables with support on a large number of qubits, the measurements themselves are more prone to qubit measurement errors.

In Ref. [24], our low-rank decomposition method (Ref. [1]) is used to write the Hamiltonian in the form

$$H = U_0 \left(\sum_p g_p n_p \right) U_0^\dagger + \sum_{\ell=1}^{L} U_\ell \left(\sum_{pq} g_{pq}^{(\ell)} n_p n_q \right) U_\ell^\dagger \tag{3.11}$$

where g_p, g_{pq} are coefficients determined by the model, n is the number operator, and U_ℓ are unitary operators that implement a single particle basis rotation. Without approximation, $L = N^2$, but as we show in this chapter, $L \sim O(N)$ is sufficient for most chemical systems. The expectation value of the Hamiltonian is given by

$$\langle H \rangle = \sum_p g_p \langle n_p \rangle_0 + \sum_{\ell=1}^{L} \sum_{pq} g_{pq}^{(\ell)} \langle n_p n_q \rangle_\ell \ . \tag{3.12}$$

Thus, under this decomposition, only $L \sim O(N)$ groups are needed, though an extra linear depth circuit implementing the basis rotation is required [1]. Additionally, the operators have support on only one or two qubits, which helps mitigate read-out errors. Huggins et al. also discuss how postselection can be easily incorporate for additional error mitigation. Yen et al. extend this work by introducing a full-rank optimization to further reduce the number of terms in the decomposition, though determining this optimal form requires non-linear optimization [25].

3.3 Low-Rank Decomposition

The electronic structure Hamiltonian in second quantization is defined as

$$H = \sum_{p,q=1}^{N} h_{pq} a_p^\dagger a_q + \frac{1}{2} \sum_{p,q,r,s=1}^{N} h_{pqrs} a_p^\dagger a_q^\dagger a_r a_s \equiv h + V \tag{3.13}$$

where N is the number of spin orbitals, $a_p^\dagger$ and a_p are fermionic creation and annihilation operators for spin orbital ϕ_p, and the scalar coefficients h_{pq} and h_{pqrs} are the 1- and 2-electron integrals over the basis functions ϕ_p, which we assume to be real.

The uCC cluster operator is defined as $\tau = T - T^\dagger$, where T is the standard (non-unitary) coupled cluster (CC) operator. If one only accounts for single and double excitations applied to a single determinant reference (which is typical for CC), the uCCSD operator is of the form

$$\begin{aligned} \tau &= \sum_{i=1}^{N_o} \sum_{a=N_o+1}^{N} t_{ai} (a_a^\dagger a_i - a_i^\dagger a_a) + \frac{1}{4} \sum_{i,j=1}^{N_o} \sum_{a,b=N_o+1}^{N} t_{abij} (a_a^\dagger a_b^\dagger a_i a_j - a_i^\dagger a_j^\dagger a_a a_b) \\ &\equiv \sum_{pq=1}^{N} t'_{pq} a_p^\dagger a_q + \frac{1}{4} \sum_{pqrs=1}^{N} t'_{pqrs} a_p^\dagger a_q^\dagger a_r a_s \quad , \end{aligned} \tag{3.14}$$

where i, j and a, b index the N_o occupied and N_v virtual spin orbitals, respectively, and $N_o + N_v = N$. Note that the operator is anti-Hermitian by construction, so we work with $i\tau$ for ease of presentation.

We refer to the terms with the two creation and two annihilation operators are considered 4-body terms, since the term acts on up to four distinct orbitals and thus require simultaneously operating on four qubits (even though they describe the interaction of two electrons). Both H and τ contain $O(N^4)$ of these terms. As stated earlier, our goal is to find an alternate decomposition of the sum such that it consists only of 2-body terms, which can be done using a nested matrix factorization, a type of tensor factorization introduced in Ref. [32]. (The coefficients of the 4-body terms h_{pqrs} and t'_{pqrs} can be interpreted as the elements of a 4-dimensional tensor with each dimension of size N.)

We illustrate the factorization procedure using the Hamiltonian operator. First, the creation and annihilation operators are reordered,

$$V = \frac{1}{2} \sum_{pqrs=1}^{N} h_{ps,qr} (a_p^\dagger a_s a_q^\dagger a_r - a_p^\dagger a_r \delta_{qs}) = V' + S\,, \tag{3.15}$$

and V' is recast into a supermatrix indexed by orbitals (ps), (qr) involving electrons 1 and 2, respectively. Due to the commutation relations of the creation and annihilation operators, V' obeys an eight-fold symmetry: $h_{pqrs} = h_{srqp} = h_{pqsr} = h_{qprs} = h_{qpsr} = h_{rsqp} = h_{rspq} = h_{srpq}$. Thus, this matrix is real symmetric, and we can write a matrix decomposition in terms of a rank-three auxiliary tensor $\mathcal{L}$ such that

$$V' = \sum_{\ell=1}^{L} \left(\mathcal{L}^{(\ell)}\right)^2 = \sum_{\ell=1}^{L} \sum_{pqrs=1}^{N} \mathcal{L}_{ps}^{(\ell)} \mathcal{L}_{qr}^{(\ell)} a_p^\dagger a_s a_q^\dagger a_r. \tag{3.16}$$

To perform the decomposition, we use a modified Cholesky decomposition scheme that recursively increases L, the number of Cholesky vectors $\mathcal{L}^{(\ell)}$ included in the sum, until the maximum error of the decomposition is within some error threshold ε_{CD} [33–37]. We choose to measure the error with respect to the L^∞ norm. This means that the iterative modified Cholesky decomposition scheme is terminated once $\max_{psqr} |h_{ps,qr} - \sum_{\ell=1}^{L} \mathcal{L}_{ps}^{(\ell)} \mathcal{L}_{qr}^{(\ell)}| < \varepsilon_{CD}$. For ε_{CD} on the order of 10^{-4} to 10^{-6}, L scales like $O(N)$. The computational cost of the modified Cholesky decomposition scheme is known to scale asymptotically like $O(N^3)$ within the AO basis for a fixed error threshold [36–38].

In contrast, for an exact decomposition, which can equivalently be obtained via diagonalization, the sum would contain N^2 terms, and the computational cost would scale like $O(N^6)$. (Note that the positive nature of the Coulomb kernel means that V' is positive, as is needed for the Cholesky decomposition).

The next step is to decompose each auxiliary matrix $\mathcal{L}^{(\ell)}$. Again, due to the eight-fold symmetry of the Hamiltonian, this is also real symmetric and can be diagonalized,

$$\sum_{ps=1}^{N} \mathcal{L}_{ps}^{(\ell)} a_p^\dagger a_s = \sum_{i=1}^{\rho_\ell} U_{pi}^{(\ell)} \lambda_i^{(\ell)} U_{si}^{(\ell)} a_p^\dagger a_s \tag{3.17}$$

where $\lambda^{(\ell)}$, $U^{(\ell)}$ are the eigenvalues and eigenvectors of $\mathcal{L}^{(\ell)}$. At this step, we can again make an approximation by truncating terms in the sum with corresponding to eigenvalues less than ε_{ET}, so that the summation only contains ρ_ℓ instead of N terms. We choose to perform the truncation based on the L^1 norm, meaning that we use the smallest ρ_ℓ such that $\sum_{j=\rho_\ell+1}^{N} |\lambda_j^{(\ell)}| < \varepsilon_{ET}$.

Combining the two eigenvalue decompositions yields the double-factorized result,

$$\sum_{p,q=1}^{N} S_{pq} a_p^\dagger a_q + \sum_{\ell=1}^{L} \sum_{i,j=1}^{\rho_\ell} \frac{\lambda_i^{(\ell)} \lambda_j^{(\ell)}}{2} n_i^{(\ell)} n_j^{(\ell)} \equiv S + \sum_{\ell=1}^{L} V^{(\ell)} \,, \tag{3.18}$$

where, defining $\psi_i^{(\ell)} = \sum_{p=1}^{N} U_{pi}^{(\ell)} \phi_p$,

$$n_i^{(\ell)} = \sum_{p,s=1}^{N} U_{pi}^{(\ell)} a_p^\dagger a_s U_{si}^{(\ell)} = a_{\psi_i^{(\ell)}}^\dagger a_{\psi_i^{(\ell)}} \tag{3.19}$$

are number operators in a rotated basis.

The double-nested decomposition of the unitary coupled cluster (uCC) operator is slightly more complicated due to its antisymmetry ($t_{abij} = t_{jiba} = -t_{baij} = -t_{abji}$), and is elaborated on in the Supplementary Information of Ref. [39]. In essence, one performs singular value decomposition (SVD) on the CC operator T in lieu of the Cholesky decomposition, obtaining $i\tau = \sum_{\ell\mu} Y_{\ell,\mu}^2$, where $Y_{\ell,\mu}$ are normal and can be diagonalized giving the same double-factorized form. Since the time this work was first posted, an alternate decomposition with the same scaling, inspired by the cluster Jastrow operator, has been investigated [40]. Other decompositions could be considered as well [41].

3.4 Accuracy of Low-Rank Approximation

In summary, the above decomposition of the operators H and τ yields a sum consisting of L terms, and each of those terms can be written as a sum of ρ_L terms. For an exact decomposition, $L = N^2$ and $\rho_\ell = N$. In this section, we will empirically investigate the induced error in ground state energy as a result of truncating lower weight terms and the corresponding reductions in L and ρ_ℓ.

Details of calculations

We investigate trends using the following sets of molecules:

- *Set 1* – small molecules (CH_4, H_2O, CO_2, NH_3, H_2CO, H_2S, F_2, BeH_2, HCl) at experimental equilibrium geometries [42], using the STO-6G, 6-31G*, cc-pVDZ, cc-pVTZ bases. Molecules were studied with restricted Hartree Fock (RHF) and restricted classical coupled cluster with single and double excitations (RCCSD) on top of the RHF state. Matrix elements of the Hamiltonian and classical RCCSD amplitudes have been computed with the PySCF software [43].

- *Set 2* – alkane chains C_nH_{2n+2} (for $n \leq 8$) studied at experimental equilibrium geometries [42], using the STO-6G basis. Molecules were studied with RHF, RCCSD methods. Matrix elements of the Hamiltonian and classical RCCSD amplitudes have been computed with the PySCF software [43].

- *Set 3* – iron-sulfur clusters of nitrogenase ([2Fe-2S] (2Fe(II)), [4Fe-4S] (2Fe(III),2Fe(II)), and the $\mathrm{P^N}$-cluster [8Fe-7S] (8Fe(II))). The active orbitals of [2Fe-2S] and [4Fe-4S] complexes were prepared by a split localization of the converged molecular orbitals at the level of BP86/TZP-DKH, while those of the [8Fe-7S] were prepared at the level of BP86/def2-SVP. The active space for each complex was composed of Fe $3d$ and S $3p$ of the core part and σ-bonds with ligands, which is the minimal chemically meaningful active space. The structure of the iron-sulfur core and the numbers of active orbitals and electrons for each complex are summarized in the diagram below. Note that the active space employed in the present work for the $\mathrm{P^N}$-cluster is larger than the active space previously used to treat the FeMoco cluster of nitrogenase, and has the same number of transition metal atoms [44].

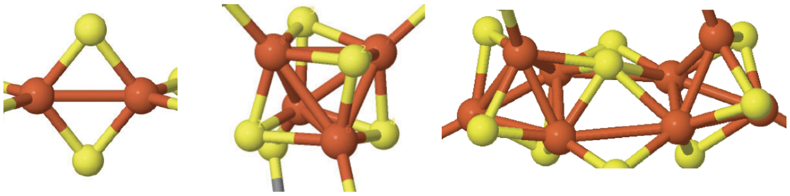

(a) [2Fe-2S] (30e,20o) (b) [4Fe-4S] (54e,36o) (c) [8Fe-7S] (114e,73o)

These molecules were treated with density-matrix renormalization group (DMRG) [45, 46], using the software BLOCK that is available as a part of PySCF. The DMRG calculations were performed for the $S = 0$ states, which are the experimentally identified ground states, with bond dimensions 8000, 4000, and 2000 for [2Fe-2S], [4Fe-4S], and the $\mathrm{P^N}$-cluster, respectively. Broken-symmetry unrestricted Hartree-Fock (UHF) ($M_S = 0$) calculations were carried out for [2Fe-2S] and [4Fe-4S], while high-spin UHF calculations were carried out for [8Fe-7S] due to convergence issues.

Studying the first set will show the performance with respect to basis set size, while studying the second and third sets will show performance with respect to molecule size.

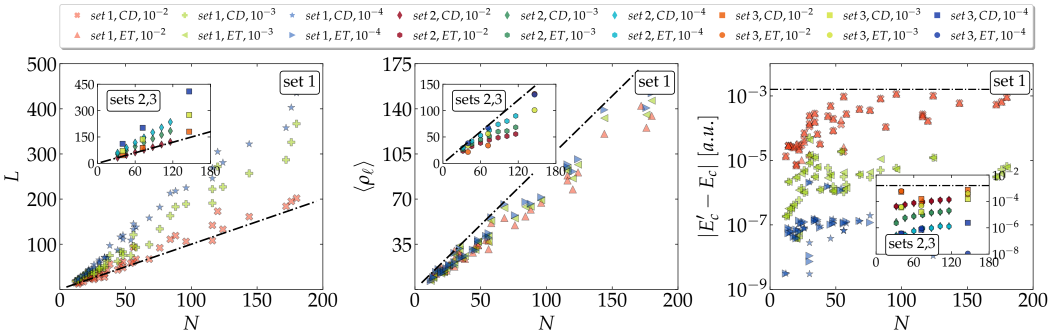

Figure 3.1: Results of low rank decomposition for various molecular systems. (Left) linear scaling of the number L of vectors with basis size N, in the low-rank approximation of H. (Middle) sublinear scaling of the average eigenvalue number $\langle \rho_\ell \rangle$. (Right) error $|E_c' - E_c|$ in the ground-state correlation energy from the low-rank approximation of H, compared with chemical accuracy (horizontal black line). Data points in the main figures comprise set 1 (small molecules with fixed size and increasingly large basis); insets show set 2 (alkane chains with up to 8 C atoms) and set 3 (iron-sulfur clusters of nitrogenase). Lines indicate N (left, middle) and the chemical accuracy (right). Results are shown for different truncation thresholds $\varepsilon = \varepsilon_{CD} = \varepsilon_{TH} = \{10^{-2}, 10^{-3}, 10^{-4}\}$ in red, green, and blue, respectively.

Electronic structure Hamiltonian truncation

We obtain the atomic orbitals and the electronic structure Hamiltonian coefficients h_{pq} and h_{pqrs} for various molecular systems using Hartree Fock (detailed in the previous section). We then use coupled cluster to compute the ground state energy.

For simplicity, we chose to perform truncations on h_{pqrs} with error thresholds $\varepsilon_{CD} = \varepsilon_{ET} \equiv \varepsilon$ in atomic units. Note that for H, ε_{CD} and ε_{ET} have dimension energy and square root of energy, respectively. Performing the CD truncation in the atomic orbital basis or localized molecular orbital basis yields comparable results.

Results for different truncation thresholds are shown in Fig. 3.1. The CD rank scales like $L \sim \mathcal{O}(N)$ when increasing the simulation basis (set 1) or molecular size (sets 2, 3). The average ET rank, defined as $\langle \rho_\ell \rangle = \frac{1}{L} \sum_{\ell=1}^{L} \rho_\ell$, is known to scale like $\langle \rho_\ell \rangle \sim \mathcal{O}(1)$ for increasing molecular size in the asymptotic limit [32, 47]. However, from our empirical results, it appears that the molecules studied here are not large enough to reach that limit, though the scaling is sublinear. There also does not appear to be a reduced scaling with respect to increased basis size. As expected, the error in the ground-state correlation energy is set by ε and is largely independent of system size.

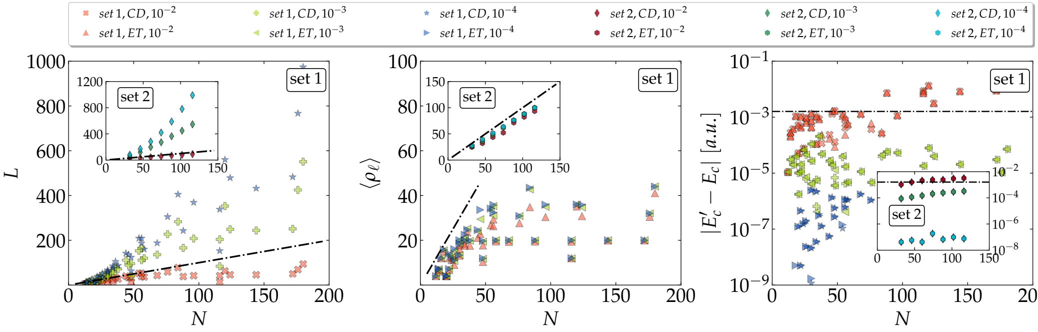

Figure 3.2: Same as Fig. 3.1, but for the uCC operator τ, with $\langle \rho_\ell \rangle$ averaged over μ.

Unitary coupled cluster operator truncation

We use the (classically computable) traditional ground state CC amplitudes to build the uCC operator. It is expected that the CC amplitudes will equal the actual uCC amplitudes in the weak-coupling limit.

For the uCC operator, truncations at both decomposition steps are performed by discarding the vectors associated with singular values smaller than ε. Again, we refer readers to the Appendix of [39] for a detailed description of the decomposition. Note that here, for the uCC operator, ε is dimensionless.

The decomposition of uCC operator τ shows worse scalings than for the Hamiltonian. Specifically, we find that $L \sim \mathcal{O}(N)$ scaling for increasing basis size and fixed molecule (see set 1) but $L \sim \mathcal{O}(N^2)$ for increasing molecular size, albeit with a small coefficient (set 2). The scaling properties of $\rho_{\ell,\mu}$ have not previously been studied, but from our empirical results it appears to scale like $\mathcal{O}(1)$ for increasing basis size (set 1) and $\mathcal{O}(N)$ for increasing molecular size (set 2). These less favorable results can be attributed to the antisymmetry of uCC operator, which prevents the separation of the two electrons in the 4-body term, so the vectors from the first decomposition step will not be as sparse as those for the Hamiltonian. Again, other decompositions that account for the antisymmetry could be considered and may potentially yield better reductions in the scaling [40, 41].

First order correction

One can obtain a better estimate of the energy of the targeted eigenstate by using a first order correction. In the traditional presentation of perturbation theory, we have the Hamiltonian

$$H(\lambda) = H^{(0)} + \lambda V \tag{3.20}$$

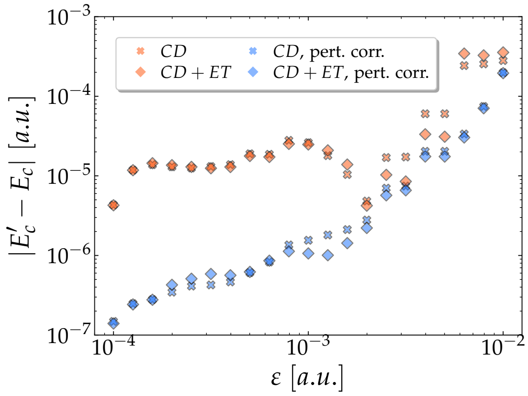

Figure 3.3: Error $|E_c' - E_c|$ for H_2O (cc-pVDZ) as a function of $\varepsilon = \varepsilon_{TH} = \varepsilon_{CD}$, with and without perturbative correction (blue and orange points, respectively) for CD and CD+ET truncation schemes (crosses, diamonds), measured using HF and CC wavefunctions. The error increases with ε, and is visibly smaller with the perturbative correction.

for some small parameter λ, and we wish to find the solutions to the Schrodinger equation

$$H(\lambda)\Psi(\lambda) = E(\lambda)\Psi(\lambda) \tag{3.21}$$

where

$$\Psi(\lambda) = \Psi^{(0)} + \lambda\Psi^{(1)} + \lambda^2\Psi^{(2)} + \dots \tag{3.22}$$

$$E(\lambda) = E^{(0)} + \lambda E^{(1)} + \lambda^2 E^{(2)} + \dots \tag{3.23}$$

We proceed by matching up powers of λ. From the λ^0 terms, we simply arrive at the zeroth order problem,

$$H^{(0)}\Psi_n^{(0)} = E_n^{(0)}\Psi_n^{(0)} \tag{3.24}$$

where the subscript n denotes the n^{th} eigenstate.

From the λ^1 terms, we have an expression for a first-order correction to the energy,

$$E_n^{(1)} = \langle\Psi_n^{(0)}|V|\Psi_n^{(0)}\rangle\ . \tag{3.25}$$

Here, we are interested in obtaining a correction to the energy of the truncated Hamiltonian H', which is within ε of the original Hamiltonian H. First, using CCSD, one can determine the ground state energy E' and the corresponding ground state ψ_0' of the approximate Hamiltonian H'. The first order correction to the energy is given by Eq. (3.25), where $V = H - H'$ and $\Psi_n^{(0)} = \psi_0'$. If ψ_0' is accurate enough, then the correlation energy (defined as $E_c' = E' - E_{HF}'$, where E_{HF}' is the ground state energy obtained using Hartree-Fock) with the first order correction is accurate to $\mathcal{O}(\varepsilon^2)$.

3.5 Quantum Resource Estimates

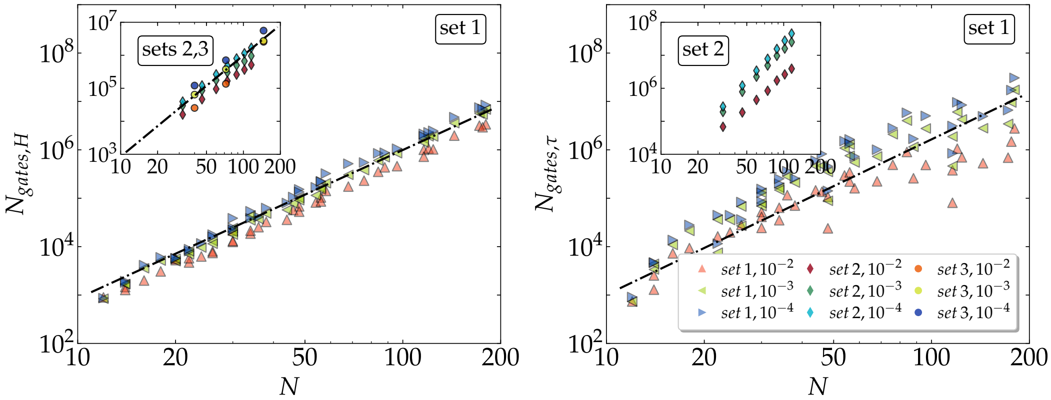

Figure 3.4: Gate counts per Trotter step of the Hamiltonian (top) and uCC operator (bottom), for $\varepsilon_{CD} = \varepsilon_{ET} = \varepsilon_{SVD} = 10^{-2}$, 10^{-3}, and 10^{-4} (red, green, blue). Black lines indicate power-law fits, with optimal exponents 3.06(3) and 3.2(1) (top, bottom). Both gate counts scale as the third power of the basis size N across a wide range of truncation thresholds, an improvement over the $\mathcal{O}(N^4)$ scaling assuming no truncation.

The first-order Trotter decomposition of the exponential of the double-factorized decomposed operator Eq. ((3.18)) can be implemented efficiently on a quantum computer with only linear connectivity. For example, the Hamiltonian Trotter step is

$$e^{i\Delta t H} = e^{i\Delta t(h+S)} U^{(1)} \prod_{\ell=1}^{L} e^{i\Delta t V^{(\ell)}} \tilde{U}^{(\ell)} + \mathcal{O}(\Delta t)^2 \ , \tag{3.26}$$

where $\tilde{U}^{(\ell)} = U^{\dagger(\ell)} U^{(\ell+1)}$. Time evolution then corresponds to a series of (single-particle) basis rotations and evolution under two-body single-particle operators $(h + S)$ and pairwise operators $(V^{(\ell)})$.

First, let us reexamine the $h + S$ term. The operator $h + S$ is currently written as a sum of two-body single-particle terms. Thus, if we define $U^{(0)}$ to be the single-particle basis rotation that diagonalizes $h + S$, then this component of the Trotter step can be implemented by applying $U^{(0)}$ followed by a simultaneous application of N single-qubit phase gates.

Next, let us consider the implementation of the basis rotations. As written, the single-particle basis changes $U^{(\ell)}$ can be implemented using $\binom{N}{2} - \binom{N-\rho_\ell}{2}$ Givens rotations [48]. (Details are given later at the end of this section.) These rotations can be implemented efficiently using two-qubit gates on a linearly connected architecture [1, 2]. If one takes S_Z spin symmetry into account, then one can perform basis rotations separately for spin-up and spin-down orbitals, requiring $2\binom{N/2}{2}$ - $2\binom{(N-\rho_\ell)/2}{2}$ Givens rotations and a circuit depth (on a linear architecture) of $(N + \rho_\ell)/2$.

Lastly, using a fermionic swap network, the component corresponding to evolution of the pairwise operator $V^{(\ell)}$ can be implemented in $\binom{\rho_\ell}{2}$ linear nearest-neighbor two-qubit gates, with a two-qubit gate depth of exactly ρ_ℓ [1].

Altogether, the gate count for implementing the full Trotterized exponentiated operator is $\binom{N}{2} + \sum_{\ell\mu} \left[\binom{N}{2} - \binom{N-\rho_{\ell,\mu}}{2}\right] + \binom{\rho_{\ell,\mu}}{2}$ for both the Hamiltonian H and the uCC cluster operator τ. Note that the sum over ℓ starts from 1 and the initial basis rotation is written explicitly. For H, the indices μ are dummy indices and can be ignored.

To realize this algorithm on a near-term device, where the critical cost model is the number of two-qubit gates, one can implement the gates directly in hardware [49], which requires $\sum_{\ell=1}^{L} \left[\frac{N\rho_\ell}{4} + \frac{\rho_\ell^2}{4} - \rho_\ell\right]$ gates on a linear nearest neighbor architecture, with circuit depth $\sum_{\ell=1}^{L} \frac{N}{2} + \frac{3\rho_\ell}{2}$. If decomposing into a standard two-qubit gate set (e.g. CZ or CNOT), the gate count would be three times the above count.

From our analysis of the decomposition steps, we expect the Trotterized Hamiltonian exponential to have a gate count of $N_{gates} \sim O(N^3)$ for fixed molecular size and increasing basis size. (We expect to see $O(N^2)$ scaling for asymptotically large molecular sizes, but none of the systems studied here reach that limit.) Furthermore, the divergence from linear scaling we saw earlier with increasing alkane chain length in $\langle \ell \rangle$ is no longer as visible due to tails in the distribution in ρ_ℓ). We expect the Trotterized uCC exponential to have a gate count of $N_{gates} \sim O(N^4)$ for increasing molecular size and $O(N^3)$ with increasing basis size. These scalings are verified in Fig. 3.4, which plots the two-body gate counts for Trotterized H' and τ' expontentials with different truncation thresholds.

For a system size of about 50 qubits (believed to roughly be the quantum computer size at which quantum supremacy can be demonstrated [50]), a single Trotter step can be implemented in roughly 4,000 layers of parallel gates, assuming a linear architecture.

Partial basis rotation

Here we will walk through implementing a partial basis rotation, which can be implemented using $\binom{N}{2} - \binom{N-\rho_\ell}{2}$ Givens rotations.

Recall that the single particle basis rotation $U^{(\ell)}$ is defined such that

$$\tilde{a}_p^\dagger = \sum_{q=1}^{N} U_{pq}^{(\ell)} a_q^\dagger \qquad \tilde{a}_p = \sum_{q=1}^{N} \left(U_{pq}^{(\ell)}\right)^* a_q \ . \tag{3.27}$$

According to the Thouless theorem [51], one can perform basis rotations of fermionic operators on quantum computers by applying a series of rotations that act on two rows (p,q) of $U^{(\ell)}$ at a time. These rotations are determined by the angles of the Givens rotations $r_{pq}(\theta_{pq})$ used to perform a QR decomposition of $U^{(\ell)}$. Because $U^{(\ell)}$ is unitary, the rotations will yield a diagonal R where the diagonal elements are of magnitude 1, and the QR decomposition only requires performing rotations on the $\binom{N}{2}$ elements below the diagonal. The number of two-body gates used to build the unitary operator is the same as the number of Givens rotations, and can be performed in linear depth on a device with linear connectivity when performed in a particular order [1]. (It is straightforward to extend this to basis rotations of bosonic systems. In fact, the necessary rotations to build the unitary operator would more closely reflect the Given's rotations.)

Here, we are interested in performing an approximation basis transformation using $O(\rho_\ell N)$ Givens rotations, where $\rho_\ell \leq N$ and is the number of eigenvalues retained after making the eigenvalue truncation low-rank approximation. Consider the eigenvalue decomposition of the auxiliary matrix used to obtain Eq. (3.17),

$$\sum_{q=1}^{N} \mathcal{L}_{pq}^{(\ell)} U_{qi}^{(\ell)} = \lambda_i^{(\ell)} U_{pi}^{(\ell)} \quad , \tag{3.28}$$

where $\mathcal{L}^{(\ell)}$ is the ℓ-th auxiliary vector reshaped into an $N \times N$ square matrix, and $\lambda^{(\ell)}$ is the diagonal matrix of the corresponding eigenvalues ordered by decreasing magnitude.

In the eigenvalue truncation of $\mathcal{L}^{(\ell)}$, we only use the ρ_ℓ largest eigenvalues or, equivalently, the eigenvectors associated with the first ρ_ℓ columns of $U^{(\ell)}$. This means the sizes of the rotation matrices are reduced, and the eigenvalue equation becomes

$$\left(\bar{U}^{(\ell)}\right)^\dagger \mathcal{L}^{(\ell)} \bar{U}^{(\ell)} = \bar{\lambda}_i^{(\ell)} \quad , \tag{3.29}$$

where $\bar{U}$ and $\bar{\lambda}$ are matrices comprising the first ρ_ℓ columns of U and diagonal elements of λ, respectively. If we perform a QR decomposition of $\bar{U}^{(\ell)}$, the top left $\rho_\ell \times \rho_\ell$ block is diagonal and the lower $(N - \rho_\ell)$ rows are zero. Since $\bar{U}^{(\ell)}$ is only an $N \times \rho_\ell$ matrix, fewer Givens rotations are needed to perform the decomposition than in the full case. Specifically, it at worst requires $\binom{N}{2} - \binom{N-\rho_\ell}{2}$ rotations. Thus, as stated in the earlier discussion, the quantum circuit needed to implement rotation also contains that same number of gates in $\rho_{(\ell)}$ layers.

In the quantum algorithm proposed in the main text, one rotates from the basis of one Cholesky vector to another. This rotation, explicitly given by $U^{\dagger(\ell)}U^{(\ell+1)}$, can be reduced into a single operation, corresponding to a $\rho^{(\ell)} \times \rho^{(\ell+1)}$ matrix. Using the same Givens rotation decomposition as above, we find that the costs are found by making the substitutions $\rho_{(\ell)} \longrightarrow \rho_{(\ell+1)}$ and $N \longrightarrow \rho_\ell$.

3.6 Discussion

In summary, we introduced a nested decomposition scheme that allows one to represent two-electron operators written as sums of 1-, 2-, and 4-body terms, such as the electronic structure Hamiltonian and uCC operator, instead as sums of 2-body terms with unitary basis rotations. This alternate form is optimized for implementation on a quantum computer. Furthermore, the decomposition scheme allows one to systematically truncate unimportant terms in the Hamiltonian. Due to the innate sparsity in the operators for physical systems that exhibit spatial locality, the number of terms in the sum can be reduced from $O(N^4)$ to $O(N^3)$. This in turn reduces the total gate count required to implement the Trotterized operator exponential, as well as the number of measurements required when measuring the expected value of the operator.

The proposed decomposition scheme performs slightly worse for the uCC operator due to its antisymmetry. One could potentially investigate alternate decomposition schemes that account for antisymmetry more efficiently [41]. For example, one recent work implements the cluster-Jastrow ansatz, which is constructed differently but has the same double-factorized form [40].

Furthermore, while the work was originally formulated in the context of implementing quantum chemistry algorithms on NISQ devices, the advantages of performing the low-rank approximation of the operators will provide benefits for fault-tolerant devices [22–25], and also classical methods such as in quantum Monte Carlo [47].

References

[1] I. D. Kivlichan, J. McClean, N. Wiebe, C. Gidney, A. Aspuru-Guzik, G. K.-L. Chan, and R. Babbush, "Quantum simulation of electronic structure with linear depth and connectivity," Phys. Rev. Lett. **120**, 110501 (2018).

[2] Z. Jiang, K. J. Sung, K. Kechedzhi, V. N. Smelyanskiy, and S. Boixo, "Quantum algorithms to simulate many-body physics of correlated fermions," Phys. Rev. Appl. **9**, 044036 (2018).

[3] R. P. Feynman, "Simulating physics with computers," International J. Theor. Phys. **21**, 467–488 (1982).

[4] R. P. Feynman, "Quantum mechanical computers," Foundations Phys. **16**, 507–531 (1986).

[5] A. Y. Kitaev, "Quantum measurements and the abelian stabilizer problem," arXiv preprint quant-ph/9511026 (1995).

[6] D. S. Abrams and S. Lloyd, "Quantum algorithm providing exponential speed increase for finding eigenvalues and eigenvectors," Phys. Rev. Lett. **83**, 5162 (1999).

[7] A. Aspuru-Guzik, A. D. Dutoi, P. J. Love, and M. Head-Gordon, "Simulated quantum computation of molecular energies," Science **309**, 1704–1707 (2005).

[8] A. Ekert and R. Jozsa, "Quantum computation and Shor's factoring algorithm," Rev. Mod. Phys. **68**, 733–753.

[9] R. Jozsa, "Quantum algorithms and the Fourier transform," Proc. R. Soc. Lond. A **454**, 323–337 (1998).

[10] M. A. Nielsen and I. Chuang, *Quantum computation and quantum information* (Cambridge U.P., 2000).

[11] D. W. Berry, A. M. Childs, R. Cleve, R. Kothari, and R. D. Somma, "Simulating Hamiltonian dynamics with a truncated Taylor series," Phys. Rev. Lett. **114**, 090502 (2015).

[12] G. H. Low and I. L. Chuang, "Hamiltonian simulation by qubitization," Quantum **3**, 163 (2019).

[13] G. H. Low and N. Wiebe, "Hamiltonian simulation in the interaction picture," arXiv preprint quant-ph/1805.00675 (2018).

[14] J. T. Seeley, M. J. Richard, and P. J. Love, "The Bravyi-Kitaev transformation for quantum computation of electronic structure," J. Chem. Phys. **137**, 224109 (2012).

[15] M. B. Hastings, D. Wecker, B. Bauer, and M. Troyer, “Improving quantum algorithms for quantum chemistry,” Quantum Info. Comput. **15**, 1–21 (2015).

[16] R. Babbush, N. Wiebe, J. McClean, J. McClain, H. Neven, and G. K.-L. Chan, “Low-depth quantum simulation of materials,” Phys. Rev. X **8**, 011044 (2018).

[17] D. Poulin, M. B. Hastings, D. Wecker, N. Wiebe, A. C. Doberty, and M. Troyer, “The Trotter step size required for accurate quantum simulation of quantum chemistry,” Quantum Info. Comput. **15**, 361–384 (2015).

[18] A. Peruzzo, J. McClean, P. Shadbolt, M.-H. Yung, X.-Q. Zhou, P. J. Love, A. Aspuru-Guzik, and J. L. O’Brien, “A variational eigenvalue solver on a photonic quantum processor,” Nature Commun. **5**, 4213 (2014).

[19] J. R. McClean, J. Romero, R. Babbush, and A. Aspuru-Guzik, “The theory of variational hybrid quantum-classical algorithms,” New J. Phys. **18**, 023023 (2016).

[20] J. Romero, R. Babbush, J. R. McClean, C. Hempel, P. J. Love, and A. Aspuru-Guzik, “Strategies for quantum computing molecular energies using the unitary coupled cluster ansatz,” Quantum Sci. Technol. **4**, 014008 (2018).

[21] S. McArdle, S. Endo, A. Aspuru-Guzik, S. C. Benjamin, and Y. Xiao, “Quantum computational chemistry,” Rev. Mod. Phys. **92**, 015003 (2020).

[22] D. W. Berry, C. Gidney, M. Motta, J. R. McClean, and R. Babbush, “Qubitization of arbitrary basis quantum chemistry leveraging sparsity and low rank factorization,” Quantum **3**, 208 (2019).

[23] V. von Burg, G. H. Low, T. Häner, D. S. Steiger, M. Reiher, M. Roetteler, and M. Troyer, “Quantum computing enhanced computational catalysis,” arXiv preprint quant-ph/2007.14460 (2020).

[24] W. J. Huggins, J. McClean, N. Rubin, Z. Jiang, N. Wiebe, *et al.*, “Efficient and noise resilient measurements for quantum chemistry on near-term quantum computers,” npj Quantum Inf. **7**, 23 (2021).

[25] T.-C. Yen and A. F. Izmaylov, “Cartan sub-algebra approach to efficient measurements of quantum observables,” arXiv preprint quant-ph/2007.01234 (2020).

[26] J. R. McClean, M. E. Kimchi-Schwartz, J. Carter, and W. A. de Jong, “Hydrid quantum-classical hierarchy for mitigation of decoherence and determination of excited states,” Phys. Rev. A **95**, 042308 (2017).

[27] O. Higgott, D. Wang, and S. Brierley, “Variational quantum computation of excited states,” Quantum **3** (2019).

[28] A. M. Childs and N. Wiebe, “Hamiltonian simulation using linear combinations of unitary operations,” Quantum Info. Comput. **12**, 901–924 (2012).

[29] G. H. Low and I. L. Chuang, “Optimal Hamiltonian simulation by quantum signal processing,” Phys. Rev. Lett. **118**, 010501 (2017).

[30] D. Wecker, M. B. Hastings, and M. Troyer, “Progress torwards practical variational algorithms,” Phys. Rev. A **92**, 042303 (2015).

[31] N. C. Rubin, R. Babbush, and J. McClean, “Application of fermionic marginal constraints to hybrid quantum algorithms,” New J. Phys. **20**, 053020 (2018).

[32] B. Peng and K. Kowalski, “Highly efficient and scalable compound decomposition of two-electron integral tensor and its application in coupled cluster calculations,” J. Chem. Theory Comput. **13**, 4179–4192 (2017).

[33] N. H. F. Beebe and J. Linderberg, “Simplifications in the generation and transformation of two-electron integrals in molecular calculations,” Int. J. of Quantum Chem. **12**, 683–705 (1977).

[34] H. Koch, A. Sánchez de Merás, and T. B. Pedersen, “Reduced scaling in electronic structure calculations using Cholesky decompositions,” J. Chem. Phys. **118**, 9481–9484 (2003).

[35] F. Aquilante, L. De Vico, N. Ferré, G. Ghigo, P.-å. Malmqvist, P. Neogrády, T. B. Pedersen, M. Pitoňák, M. Reiher, B. O. Roos, *et al.*, “MOLCAS 7: the next generation,” J. Comput. Chem. **31**, 224–247 (2010).

[36] W. Purwanto, H. Krakauer, Y. Virgus, and S. Zhang, “Assessing weak hydrogen binding on Ca^+ centers: an accurate many-body study with large basis sets,” J. Chem. Phys. **135**, 164105 (2011).

[37] M. Motta and S. Zhang, “Ab initio computations of molecular systems by the auxiliary-field quantum Monte Carlo method,” Wires. Comput. Mol. Sci. **8**, e1364 (2018).

[38] S. D. Folkestad, E. F. Kjønstad, and H. Koch, “An efficient algorithm for Cholesky decomposition of electron repulsion integrals,” J. Chem. Phys. **150**, 194112 (2019).

[39] M. Motta, E. Ye, J. McClean, Z. Li, A. J. Minnich, R. Babbush, and G. K.-L. Chan, “Low rank representations for quantum simulation of electronic structure,” arXiv preprint physics.comp-ph/1808.02625 (2018).

[40] Y. Matsuzawa and Y. Kurashige, “Jastrow-type decomposition in quantum chemistry for low-depth quantum circuits,” J. Chem. Theory Comput. **16**, 944–952 (2020).

[41] N. Shenvi, H. Van Aggelen, Y. Yang, W. Yang, C. Schwerdtfeger, and D. Mazziotti, “The tensor hypercontracted parametric reduced density matrix algorithm: Coupled-cluster accuracy with $o(r^4)$ scaling,” J. Chem. Phys. **139**, 054110 (2013).

[42] R. D. Johnson III, *NIST 101. Computational chemistry comparison and benchmark database*, Tech. Rep. (1999).

[43] Q. Sun, T. C. Berkelbach, N. S. Blunt, G. H. Booth, S. Guo, Z. Li, J. Liu, J. D. McClain, E. R. Sayfutyarova, S. Sharma, *et al.*, "PySCF: the Python-based simulations of chemistry framework," Wires. Comput. Mol. Sci. .

[44] M. Reiher, N. Wiebe, K. M. Svore, D. Wecker, and M. Troyer, "Elucidating reaction mechanisms on quantum computers," P. Natl. Acad. Sci. USA **114**, 7555–7560 (2017).

[45] S. R. White, "Density matrix formulation for quantum renormalization groups," Phys. Rev. Lett. **69**, 2863 (1992).

[46] G. K.-L. Chan and M. Head-Gordon, "Highly correlated calculations with a polynomial cost algorithm: A study of the density matrix renormalization group," J. Chem. Phys. **116**, 4462–4476 (2002).

[47] M. Motta, J. Shee, S. Zhang, and G. K.-L. Chan, "Efficient ab initio auxiliary-field quantum Monte Carlo calculations in Gaussian bases via low-rank tensor decomposition," J. Chem. Theory Comput. (2019).

[48] D. Wecker, M. B. Hastings, N. Wiebe, B. K. Clark, C. Nayak, and M. Troyer, "Solving strongly correlated electron models on a quantum computer," Phys. Rev. A **92**, 062318 (2015).

[49] M. Y. Niu, S. Boixo, V. N. Smelyanskiy, and H. Neven, "Universal quantum control through deep reinforcement learning," npj Quantum Inf. **5**, 33 (2019).

[50] F. Arute, K. Arya, R. Babbush, D. Bacon, J. C. Bardin, R. Barends, R. Biswas, S. Boixo, F. G. S. L. Brandao, D. A. Buell, *et al.*, "Quantum supremacy using a programmable superconducting processor," Nature **574**, 505–510 (2019).

[51] D. J. Thouless, "Stability conditions and nuclear rotations in the Hartree-Fock theory," Nucl. Phys. **21**, 225–232 (1960).

Chapter 4

TIME EVOLUTION USING LOW-RANK INFLUENCE FUNCTIONAL FOR GENERAL QUANTUM SYSTEMS

Obtaining long-time dynamics of a quantum system is computationally intractable due to the exponential scaling of Hilbert space with respect to system size. For example, while tensor networks (TNs) are a powerful tool for physics simulations, traditional time evolution algorithms, which involve directly computing the state at each time, often encounter issues because the entanglement of the state grows exponentially and the state can no longer be efficiently represented using a TN. Fortunately, in many cases, one is most interested in the dynamics of a small subset of the full system, and can reframe the original Hamiltonian as a system and bath problem. In this chapter, we introduce an alternative tensor network contraction scheme to compute long-time dynamics for such systems, and present results for single-site dynamics of general 1-D systems.

Specifically, we choose to contract and compress the time evolution TN in the direction of the spatial axis, such that the dynamics of the bath sites are contracted and compressed together. We show that this iterative contraction scheme is equivalent to computing a generalized influence functional, and can be used to determine the general quantum dynamics of a subsystem. We investigate its approximability in terms of the bond dimensions and time-like entanglement in the tensor network description. We study two numerical models, the spin-boson model and a model of interacting hard-core bosons in a 1D harmonic trap. We find that the influence functional and the intermediates involved in its construction can be efficiently approximated by low bond dimension tensor networks in certain dynamical regimes, which allows the quantum dynamics to be accurately computed for longer times than with direct time evolution methods. However, as one iteratively integrates out the bath, the correlations in the influence functional can first increase before decreasing, indicating that the final compressibility of the influence functional is achieved via non-trivial cancellation.

The content of this chapter is published as

E. Ye and G. K.-L. Chan. “Constructing tensor network influence functionals for general quantum dynamics,” arXiv preprint quant-ph/2101.05466 (2021).

An introduction to tensor networks is included in Appendix A.

4.1 Introduction

While computing the time evolution of a quantum state can be computationally intractable, particularly in the case of a quench where the initial state is far from an eigenstate of the Hamiltonian of interest, one typically is interested in a small fraction of the information contained in the state. For example, one might only be interested in the dynamics of a small subset of sites, such as in the case of a small quantum system coupled to a large bath. The small systems are typically referred to as open quantum systems, and the system and bath together can often described using impurity models. We argue that any observable with support on a small subset of qubits can be interpreted as such, though there might be no distinction between system and bath in the definition of the Hamiltonian. In this chapter, we present tensor network methods to compute long-time dynamics of single-site observables of general 1-D quantum systems, though the methodology can easily be extended to more general systems and observables.

Perspective from open quantum system dynamics

Many chemical and physical systems, such as a two-level system coupled to vibrational modes of a molecule or a radiation field, can be described as open quantum systems coupled to large baths. So understanding and modeling the dynamics of such systems has always been an active area of research, and there exist a wide variety of time evolution methods for open quantum systems. The key idea behind all such methods is that if one is able to determine the dynamics of the bath and its influence on the subsystem, then the original dynamics problem is now reduced to obtaining the dynamics of the subsystem.

Open quantum system time evolution methods can largely be classified into three groups: those based on direct time evolution of the the full system, those based on the quantum master equation, and those based on the influence functional.

Numerically exact direct time evolution methods include exact diagonalization; tensor network methods such as time evolution block decimation (TEBD) [1–3], time-dependent density matrix renormalization group (TD-DMRG) [4, 5] and time-dependent variational principle (TDVP) time evolution [6, 7]; and (multi-layer) multi-configuration time-dependent Hartree (ML-MCTDH) theory (though it can also be viewed as a tensor network method). However, these methods may fail at long simulation times if the entanglement of the state becomes too large. Quantum

Monte Carlo (qMC) can also be used to perform direct time evolution, though it suffers from the dynamical sign problem [8–12]. However, a qMC-based inchworm method, in which information from exact Keldysh-contour propagators for short times are reused iteratively to extend the propagator to longer times [13–15], was shown to be less susceptible to the sign problem. There also exist approximate direct time evolution methods such as self-consistent hybrid quantum-classical methods, which treat the subsystem exactly and the bath classically [16–18].

The Nakajima-Zwanzig-Mori (NZM) master equation [19, 20] provides the exact solution to the dynamics of the subsystem, and the information of the bath dynamics and its influence of the dynamics are contained in a memory kernel. However, the cost of computing the memory kernel without approximation is comparable to determining the dynamics of the full system. Two types of approximations can be made. First is to compute the kernel using approximate methods. Second is to assume that the memory kernel has some particular structure, such as a finite lifetime. In the most extreme approximation, one would assume Markovian dynamics, in which the memory kernel has no lifetime and the dynamics are completely determined by the current state. This type of dynamics are given by the Lindblad equation [21, 22] and the Bloch-Redfield master equation, which is the second-order expansion of the NZM equation with respect to the interaction Hamiltonian. However, it is known that Markovian dynamics are only sufficient for simulating a limited number of systems, such as those with weak system-bath coupling. The spin-boson model, which models a dissipative two-level system and aptly describes many chemical systems, is a widely cited example of a physically relevant system that exhibits non-Markovian dynamics [23–25]. Non-Markovian approximations of the NZM equation are still an active area of research. For example, some early methods bridged the NZM and Lindblad equations by incorporating an exponentially decaying memory kernel or by expanding the kernel perturbatively [26–28]. In contrast, the Generalized Quantum Master Equation method modifies the NZM equation by rewriting the original kernel as a series of integrals without any projectors, so that it can be computed from a variety of time evolution (even semiclassical) methods [29–33]. However, the kernels are prone to numerical instabilities, and they must be truncated after some finite time. Another idea is to write the NZM equation in a time-convolutionless form that contains no convolution integral, but instead relies on time-dependent operators to capture non-Markovian dynamics [34–40]. This method requires taking an inverse of a superoperator, which is done perturbatively. A similar concept is the non-Markovian transfer tensor method, where the transfer tensors are learned from short-time trajectories [41, 42]. These works will not be discussed in detail.

Influence functionals [43] (IFs) represent the dynamics of an arbitrary bath and its interactions with the subsystem [43], and can be viewed as a reweighting of the subsystem path integral. However, the cost of computing the IF without approximation is also comparable to determining the dynamics of the full system and the size of the IF scales exponentially with the number of time steps. Thus it is not usually possible to use the IF method without additional approximations. Furthermore, most work involving IFs has been limited to harmonic baths with linear coupling, for which an analytical form has been derived [44]. This analytical expression takes the form of the Boltzmann weight of a complex valued Hamiltonian defined in the time direction with pairwise interactions between time points [44, 45]. For many physical bath spectral densities, it is natural to assume that the pairwise time interaction is short-ranged in time, corresponding to a finite "memory" in the influence of the bath. For example, in the quasi-adiabatic propagator path integral (QUAPI) method [46], one approximates the analytical IF by only including terms acting on time steps within a finite time window. The hierarchical equation of motion (HEOM) method also utilizes the analytical solution of the harmonic bath IF, though the approximation appears in the number of hierarchies used [47–50].

In summary, there exist a variety of time evolution methods for open quantum systems that rely on simplifying the computation of the dynamics of the bath (using classical, semiclassical, or perturbative methods) to reduce computational costs.

Perspective from tensor network time evolution

The time-evolved state can be explicitly represented as a TN with an extra dimension representing the time axis. Similarly, one can write a TN describing the measurement of an observable for a time-evolved state in a similar fashion by also including the complex conjugate of the state. This network has no dangling (uncontracted) bonds, and thus returns a scalar value when all of the tensors are contracted together. Suppose the TN is written such that the time axis is vertically oriented. Then, traditional time evolution corresponds to contracting the network in an up-down fashion. However, there is no particular reason as to why the contraction must be done in that order.

This idea is first touched upon by Bañuls et al, though they limited themselves to 1-D infinite translationally invariant systems with nearest neighbor interactions [51–53]. The time evolution TN now looks like a 1+1 TN, and because of the translational invariance, all of the columns are identical. By contracting the columns iteratively, assuming some random initial boundary condition, one will obtain the left or right dominant eigenvector of the column, and one can use it to represent the contributions of all of the other sites to the left or right of the sites of interest.

Later in the chapter, we will show that contraction and compression of the columns of the time evolution TN (ie. contraction in the direction of the spatial axis) is directly related to the influence functional.

Time locality

Time locality is the idea that a quantum system's behavior in time is more dependent on its recent history rather than its state from a long time ago. One easy example of this is thermalization–regardless of the initial state, given enough time, the system thermalizes to the same thermal state. Thus, it feels natural to assume that the dynamics for large baths that dissipate information quickly are time-local. If the system does not thermalize and instead exhibits localization, at this point it is not clear if time locality is still obeyed and is an interesting question worthy of future investigation.

Time locality appears to be correlated to the complexity of computing the dynamics of an open quantum system. For example, a completely time local system would obey Markovian dynamics, which we know is easy to compute via the Lindblad equation. In the context of the NZM equation, more time-local dynamics would correspond to memory kernels with a shorter lifetime. In the context of the IFs, one might guess that the time-time correlations of the IF would be larger for shorter time ranges, and that lower weight longer-time correlations can be dropped.

Thus, the assumption of limited memory allows one to remove the exponential growth of cost of the quantum dynamics with simulation time, making long time-scale quantum dynamical simulations possible. For example, consider the analytical expression of the IF for harmonic baths with linear coupling, which takes the form of the Boltzmann weight of a complex valued Hamiltonian defined in the time direction with pairwise interactions between time points [44, 45]. A finite "memory" in the influence of the bath would mean that pairwise time interaction is short-ranged in time, and motivates approximating the analytical IF by only including terms acting on time steps within a finite time window, as done in QUAPI [46]. Similarly, the approximations made in the methods discussed above (and their extensions) can be motivated by time-locality [13, 14, 29, 30, 33, 41, 42, 46, 54–61].

One idea that has recently been gaining traction is to represent the IF as a matrix product state (MPS), a 1-D tensor network, along the time axis (although the idea is not necessarily presented in the language of IFs). Matrix product states are known to efficiently encode short-range correlations [62], and thus are a natural finite-memory ansatz for the IF. For example, recent works include the construction of the IF (or IF-like objects, such as the auxiliary density operator as defined in QUAPI, the process tensor, or the timeline reservoir network) for translationally invariant systems [63], harmonic baths with linear coupling utilizing the analytical solution [57, 64], and other systems with star geometries [65, 66]. Some works also discuss determining the IF using tomography or machine learning [67, 68]. However, none consider computing IFs for arbitrary 1-D quantum systems, which is discussed in this chapter.

Proposed tensor network influence functional algorithm

We are interested in using tensor networks and influence functionals to compute the dynamics of a general quantum subsystem. Such a subsystem may arise as part of a larger interacting problem (in which case, the subsystem may not be different from other parts of the system) or it may arise from a system-bath model. In either case, the couplings cannot be assumed to be linear and the bath cannot be assumed to be harmonic, and thus the analytical form of the IF is not known. However, the IF is simply a particular integral of the space-time dynamics that can be obtained numerically. To do this, we can use a tensor network description of the space-time dynamics. For a 1-dimensional representation of the system and bath, the tensor network is thus defined in 1+1 dimensions, and the IF corresponds to a contraction of the network to yield a final matrix product state IF defined along the time direction. Unlike the matrices appearing in a matrix decomposition of the path integral only along the spatial direction (for example, as occurring in the modular path integral procedure [69–73]) or along the time direction, the tensors in the space-time tensor network do not have an exponential dependence on system size or time. However, to avoid exponential computational cost, the contraction must be performed approximately. The proposed approximate tensor network contraction procedure is similar to that presented by Banuls et al. [51, 53] and Lerose et al. [63], assuming a translationally invariant infinite problem. However, we will describe a general procedure to construct the IF without such assumptions and explore the numerical feasibility of doing so to compute quantum dynamics in different regimes beyond linear coupling to quadratic baths.

The chapter is organized as follows. We first translate the IF into a space-time tensor network language and describe an iterative algorithm to compute it. We then investigate the compressibility of the IF and its ability to produce long-time dynamics, first for the canonical spin-boson model where the analytical IF is known, and then an interacting hard-core boson model where there is no analytical expression, which corresponds to the case of general quantum dynamics. We analyze the time-like entanglement both in the IF itself as well as the intermediates that arise as the bath is numerically integrated out. We end with a brief discussion of the implications of this work for future studies.

4.2 Theory

Definition of the influence functional

To introduce notation, we first recall the definition of the influence functional (IF) [43]. The influence functional describes how the path integral of a subsystem is reweighted, under the influence of dynamical coupling to a bath. To obtain an explicit form, we define a full system as composed of the subsystem of interest and the coupled bath. At time T, we denote the subsystem density matrix by $\rho_s(s_T)$, where s_T is a basis for the density matrix, and the bath density matrix is analogously written as $\rho_b(b_T)$. The basis of the full system is spanned by the product space $\{s\} \otimes \{b\}$. The evolution of the density matrix is given by a linear operator, the Liouville operator L, which we partition as $L = L_s + L_{bs}$ where L_s contains the component operating only on the subsystem and L_{bs} contains the component on the bath and interactions between the subsystem and bath. If we further assume the system dynamics obeys Hamiltonian evolution, then the Liouville action can be written as $L \cdot = [H, \cdot]$.

Formally, $\rho_s(s_T)$ is obtained by time evolving the entire system and tracing out the bath degrees of freedom. The path integral expression, assuming a second-order Trotter decomposition of the time evolution operator into N timesteps of length ϵ, is

$$\begin{aligned} \rho_s(s_T)\, \mathrm{Tr}_{b_T}\Bigg[& \sum_{s_{t_{N-1}}} \sum_{b_{t_{N-1}}} \cdots \sum_{s_{t_0}} \sum_{b_{t_0}} \\ & \langle\langle s_T|\, e^{-\frac{i}{2}L_s\epsilon} e^{-iL_{bs}\epsilon} e^{-iL_s\epsilon}\, |s_{t_{N-1}}, b_{t_{N-1}}\rangle\rangle \times \\ & \langle\langle s_{t_{N-1}}, b_{t_{N-1}}|\, e^{-iL_{bs}\epsilon} e^{-iL_s\epsilon}\, |s_{t_{N-2}}, b_{t_{N-2}}\rangle\rangle \times \dots \\ \times & \langle\langle s_{t_1}, b_{t_1}|\, e^{-iL_{bs}\epsilon} e^{-\frac{i}{2}L_s\epsilon}\, |s_{t_0}, b_{t_0}\rangle\rangle \times \langle\langle s_{t_0}, b_{t_0}|\rho(s_{t_0}, b_{t_0}))\rangle\rangle \Bigg] \end{aligned} \tag{4.1}$$

where $\rho(s_{t_0}, b_{t_0})$ is the initial state of the system, and the double bra/ket notation indicates we are working in Liouville space, with the density matrix being a vector in this space. For simplicity, we assume there are no correlations between the subsystem and bath initially such that $|\rho(s_{t_0}, b_{t_0})\rangle\rangle = |\rho_s(s_{t_0})\rangle\rangle\, |\rho_b(b_{t_0})\rangle\rangle$. Furthermore, L_{bs} is typically assumed to be diagonal in the basis $\{s\}$ (we lift both these restrictions below). Then Eq. (4.1) becomes

$$\begin{aligned}\rho_s(s_T) = \sum_{s_{t_{N-1}}} \cdots \sum_{s_{t_0}} \langle\langle s_T|\, e^{-\frac{i}{2}L_s\epsilon}\, |s_{t_N}\rangle\rangle \times \langle\langle s_{t_N}|\, e^{-iL_s\epsilon}\, |s_{t_{N-1}}\rangle\rangle \times \dots \\ \times \langle\langle s_{t_1}|\, e^{-\frac{i}{2}L_s\epsilon}\, |s_{t_0}\rangle\rangle\, \langle\langle s_{t_0}|\rho_s(s_{t_0})\rangle\rangle \times I(s_{t_1}, s_{t_2}, ..., s_{t_N}) \qquad (4.2)\end{aligned}$$

where $I(s_{t_1}, s_{t_2}, ..., s_{t_N})$ is the influence functional

$$I(\dots) = \mathrm{Tr}_{b_T}\left[e^{-iL_{bs}(s_{t_N})\epsilon} \dots e^{-iL_{bs}(s_{t_1})\epsilon}\, |\rho_b(b_{t_0})\rangle\rangle\right] \qquad (4.3)$$

with $L_{bs}(s) = \langle\langle s|L_{bs}|s\rangle\rangle$. The IF assigns a complex weight to each configuration of the system path integral. Consequently, the storage of the IF grows exponentially with number of time steps N.

Generalized influence functional in tensor network language

Influence functional structure

Translating Eq. (4.1) and Eq. (4.2) into the tensor network language is straightforward, and is shown in diagrams Fig. 4.1(a) and (b), respectively. The time evolution operators of the system and system-bath dynamics respectively appear as boxes with two and four legs in Fig. 4.1(a), with the legs labelled by the bra and ket basis states. The elements in the tensors are $\langle\langle s_t|e^{-iL_s\epsilon}|s_{t'}\rangle\rangle$ and $\langle\langle s_t, b_t|e^{-iL_{bs}\epsilon}|s_{t'}, b_{t'}\rangle\rangle$, respectively. In the case that L_{bs} is diagonal with respect to the subsystem basis states $\{s\}$, then the elements of the system-bath time evolution operator are $\langle\langle s_t, b_t|e^{-iL_{bs}\epsilon}|s_t, b_{t'}\rangle\rangle$ and can be depicted as a box with three legs labelled by s_t, b_t, and $b_{t'}$, as in Fig. 4.1(b). The final trace operation over the bath degrees of freedom at the last time step can be written as a vector that is contracted with the corresponding leg of the time evolution operator tensor.

The influence functional element $I(s_{t_1}, s_{t_2}, \dots, s_{t_N})$ is the object within the blue rectangle of Fig. 4.1(b), obtained after performing tensor contractions over all bath tensors as denoted by the connected lines. Within this diagrammatic picture it is easy to depict the generalization of the influence functional to a correlated initial state. In this case, the dotted line indicates a correlated initial state with entanglement

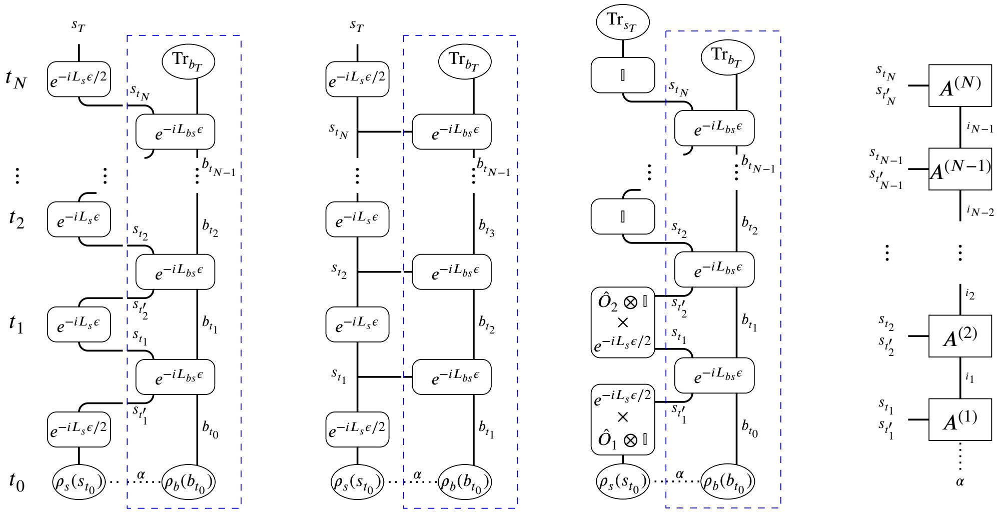

(a) (b) (c) (d)

Figure 4.1: Subsystem dynamics and the influence functional. (a) Time evolution of $\rho(s_{t_0}) = \sum_\alpha \rho_{s,\alpha}(s_{t_0}) \otimes \rho_{b,\alpha}(s_{t_0})$ in Liouville space with second order Trotter decomposition between system and interaction dynamics. (b) The same as (a) but assuming L_{bs} is diagonal with respect to subsystem basis. The boxed regions are the generalized and traditional definitions of the influence functional, respectively. (c) Measurement of the time-correlation $\langle \hat{O}_2(t_1)\, \hat{O}_1(t_0)\rangle_\rho$. (d) Matrix product state representation of influence functional. The labels $\{s_{t_m}\}$ and $\{b_{t_m}\}$ index the system and bath states at time step m, respectively. The labels $\{i_m\}$ index the virtual bonds. Lines that connect two tensors (blocks) represent tensor contraction over the labeled indices.

between the subsystem and bath,

$$\rho(s_{t_0}, b_{t_0}) = \sum_\alpha \rho_{s\alpha}(s_{t_0})\rho_{b\alpha}(b_{t_0}) \tag{4.4}$$

and the influence functional is defined with an additional index, $I(s_{t_1}, s_{t_2}, \ldots, s_{t_N}; \alpha)$. Similarly, if L_{bs} cannot be diagonalized in the subsystem basis $\{s\}$ then we can generalize the influence functional to contain two subsystem indices at each intermediate time, $I(s_{t_1}s_{t'_1}, s_{t_2}s_{t'_2}, \ldots, s_{t_N}s_{t'_N})$, and it is the object within the blue rectangle of Fig. 4.1(a). Given the influence functional, arbitrary time-correlation functions can be computed as shown in Fig. 4.1(c).

Because the influence functional has a one-dimensional structure along the time axis, it is natural to rewrite it as a matrix product state of N tensors (see Fig. 4.1(c)), i.e.

$$I(s_{t_1}, s_{t_2}, \ldots, s_{t_N}) = \sum_{\{i\}} A^{(1)}_{i_1}(s_{t_1})A^{(2)}_{i_1,i_2}(s_{t_2}) \ldots A^{(N)}_{i_{N-1}}(s_{t_N}) \tag{4.5}$$

where $A(s_t)$ denotes a matrix of dimension $D \times D$ for each element of the basis s_t, except for $A^{(1)}(s_{t_1})$ and $A^{(N)}(s_{t_N})$ which are D dimensional row and column vectors respectively. In MPS language, D is referred to as the virtual bond dimension. Although any IF can be represented as a MPS for sufficiently large D, the MPS of small bond dimension naturally capture sums of exponentially decaying time-correlations along the time axis. The key system-specific questions to understand are thus (i) is the IF itself representable by an MPS of low bond dimension, in physically relevant dynamical and interaction regimes, and (ii) can the IF be constructed with manageable cost in those regimes. It is important to note that an affirmative answer to (i) does not imply an affirmative answer to (ii).

Space-time tensor network representation

To define an approximate procedure to construct the influence functional for complex bath dynamics, we first write down a space-time representation of the full system dynamics. We first assume that the bath Hilbert space is a product space over K modes,

$$\{b\} = \{b^1\} \otimes \{b^1\} \otimes \ldots \otimes \{b^K\} \ . \tag{4.6}$$

We can then formally express the system density matrix at any time as a matrix product state

$$\rho(s_t, b_t) = \sum_{\{i\}} C^{(0)}_{i_0}(s_t) C^{(1)}_{i_0,i_1}(b^1) \ldots C^{(K)}_{i_{K-1}}(b^K) \tag{4.7}$$

with a bond dimension denoted D_ρ.

Similarly, the Liouville evolution operator can be written as a matrix product operator

$$\begin{aligned}\langle\langle s_t, b_t | e^{-iL_{bs}\epsilon} | s_{t'}, b_{t'} \rangle\rangle = \\ \sum_{\{i\}} M^{(0)}_{i_0}(s_t, s_{t'}) M^{(1)}_{i_0,i_1}(b^1_t, b^1_{t'}) \ldots M^{(K)}_{i_{K-1}}(b^K_t, b^K_{t'})\end{aligned} \tag{4.8}$$

and has a bond dimension of D_L. Note that since the Liouville operator is assumed time-independent, D_L is fixed. At last the time step, the bath degrees of freedom are traced out so the bath sites are now in MPS form,

$$\begin{aligned}\langle\langle s_{t_N} | \, \mathrm{Tr}_{b_T} \left[e^{-iL_{bs}\epsilon} \right] | \, s_{t'_N}, b_{t_{N-1}} \rangle\rangle = \\ \sum_{\{i\}} M^{(0)}_{i_0}(s_{t_N}, s'_{t_N}) \tilde{M}^{(1)}_{i_0,i_1}(b^1_{t_{N-1}}) \ldots \tilde{M}^{(K)}_{i_{K-1}}(b^K_{t_{N-1}})\end{aligned} \tag{4.9}$$

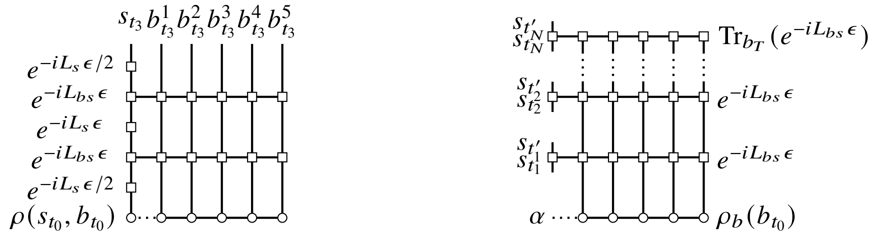

(a) time evolution TN

(b) influence functional TN

Figure 4.2: Space-time tensor network representation of (a) time evolution and (b) the influence functional. The system coupled to five bath sites is represented as a 1D MPS (row of circles), and time evolution is performed using second order Trotter decomposition between the system and interaction dynamics. The diagrams contain only two time steps. The semicircles represent the trace operation, and the trace over all bath sites can be written as a MPS of bond dimension 1.

where $\tilde{M} = \mathrm{Tr}_{b_T}(M)$ with M as defined in Eq. (4.8).

If the Hamiltonian consists of only nearest neighbor interactions, one can obtain the operator using a Trotter-Suzuki decomposition of nearest neighbour gates and then directly map them onto a matrix product operator. Otherwise, for more general interactions one can use a 4th-order Runge-Kutta expansion [74]. In this case, the matrix product operator can have large bond dimension, but can be compressed by allowing for truncation errors of $O(\epsilon^5)$. In the cases studied here, the subsystem is small enough such that $e^{-iL_s\epsilon}$ can be obtained exactly.

The full time evolution of the system with K bath modes and N time steps thus corresponds to the two-dimensional tensor network diagram shown in Fig. 4.2(a). Correspondingly, the space-time representation of the influence functional is shown in Fig. 4.2(b).

Transverse contraction scheme

The most common way to contract a 2D space-time tensor network is from bottom to top, i.e. in the direction of increasing time. [1–6, 75, 76]. We refer to this as direct time evolution. For example, contracting the network in Fig. 4.2(a) row by row yields the system density matrix at each time step as an MPS. The cost of contracting two rows is $O(KD_L^2 D_\rho^2 d_\rho^2)$ where d_ρ is the dimension of the density matrices represented at each MPS site, and D_ρ is the bond dimension of the density matrix MPS. For *exact* time evolution D_ρ grows by a factor of D_L at each time step. This means that in the worst case, D_ρ grows exponentially with time.

However, if the time-correlations in the influence functional decay with long time, then this implies that the influence functional ultimately can be represented by a matrix product with low bond dimension along the time axis. This suggests that a more efficient contraction strategy is to contract column wise (in the transverse direction to time). The cost of contracting columns together in the process of construct the final influence functional is $O(ND_L^2 D_I^2 d_\rho^2)$ where D_I is the bond dimension of the column bath MPS (defined along the time direction). For *exact* contraction, D_I will grow by d_ρ at each contraction step and thus in the worst case scales exponentially with K. But, it need not have a dependence on the total simulation time.

In practice, due to the exponential growth of the bond dimension, exact contraction of the 2D tensor network (in either direction) is often too expensive. In Banuls et al [51, 53], the explicit transverse contraction of the 2D tensor network was avoided by assuming that the system is infinite and translationally invariant, in which case the result of the infinite contraction of columns is proportional to the maximal eigenvector of the column transfer operator.

Alternatively, one may use standard matrix product state techniques to compress the intermediates that arise during the contraction to restrict bond dimensions D_ρ or D_I to some constant value [1, 3, 75]. In this case, the cost of the algorithm is dominated by the cost of the MPS compression (which requires performing a series of singular value decompositions), and scales like $O(KD_\rho^3 D_L^3 d_\rho)$ for the direct time evolution case (upward contraction by row), and $O(ND_I^3 d_\rho^3 D_L)$ for the IF time evolution procedure (sideways contraction by column). In this paper, we use such an approximate transverse contraction scheme (compressing to a fixed bond dimension of the contraction intermediates) to compute the IF (Fig. 4.2(b)) for systems with arbitrary baths. The algorithm is to iteratively contract and compress the columns from the edges of the bath inwards to the sites connected to the subsystem (Fig. 4.3). Assuming the subsystem is defined as the leftmost site, we start from the rightmost boundary column, and then the column is absorbed leftward to make a new boundary column, which is compressed using standard MPS compression to a pre-specified maximum bond dimension D_I. This is the standard "boundary contraction" algorithm of 2D tensor networks [77]. Key to the success of the algorithm and the quality of the compression is the choice in gauge (a redundant degree of freedom in all tensor networks). We choose the gauge as shown in Fig. 4.3.. In the case where the bath extends both to the left and right of the site of interest, we compute the IFs

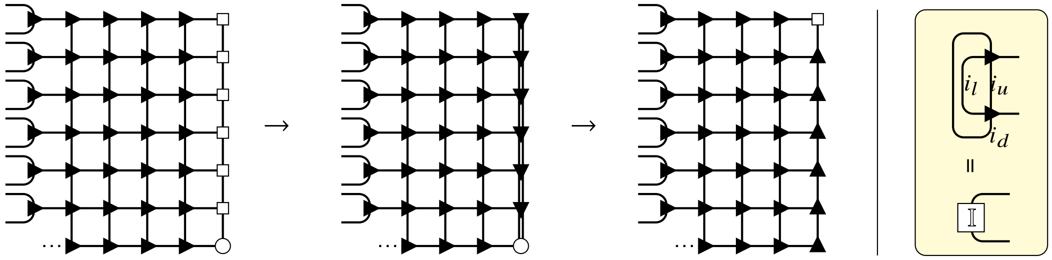

initialize contract + canonicalize compress

Figure 4.3: Iteration of transverse contraction scheme to compute IF tensor network. The time evolution operators $e^{-iL_{bs}\epsilon}$ at each time step are the rows of the grid and are each represented as an MPO, and the subsystem of interest is at the left-most site. Before contraction, we first canonicalize each row into left canonical form as indicated by the right pointing triangles along the rows. The rightmost two columns are then contracted and compressed to fixed bond dimension D_I using the standard MPS compression algorithm, where the column is first converted into a canonical form (here, top canonical form) and then compressed by singular value decomposition in the reverse direction (leaving it in bottom canonical form). The canonical form implies that the tensors satisfy an isometric condition (see diagram on the right); e.g. the right pointing arrow implies contraction of a tensor with its complex conjugate over the left, up, and down indices yields the identity matrix. The procedure is repeated until all columns have been contracted.

corresponding to the left and right bath sites separately. This contraction scheme was implemented within the Quimb tensor network library [78].

For purposes of comparison, we will also present reference dynamics generated by standard MPS time evolution (ie. contracting the space-time tensor network in the usual time direction) [1, 74, 75, 79]. Because the underlying full system dynamics is governed by Hamiltonian evolution in the problems that we study, we have the option to apply $e^{-iH\epsilon}$ as a commutator to the square root of the density matrix ($[e^{-iH\epsilon}\rho^{1/2}][\rho^{1/2\dagger}e^{iH\epsilon}]$) or via $e^{-iL\epsilon}$ directly. We refer to the former as Hilbert time evolution (HTE) and the latter as Liouville time evolution (LTE). In HTE, the compressed tensor network dynamics is carried out for the pseudowavefunction $\psi = e^{-iH\epsilon}\rho^{1/2}$ [80–82]. HTE has the advantage that the compressed density matrix is always positive definite, although correlations between the bra and ket sides of the density matrix are less compressible. In existing literature, this is sometimes referred to as purification-based time evolution. In the case that ρ is a pure state, this method is equivalent to traditional MPS Hilbert space time evolution.

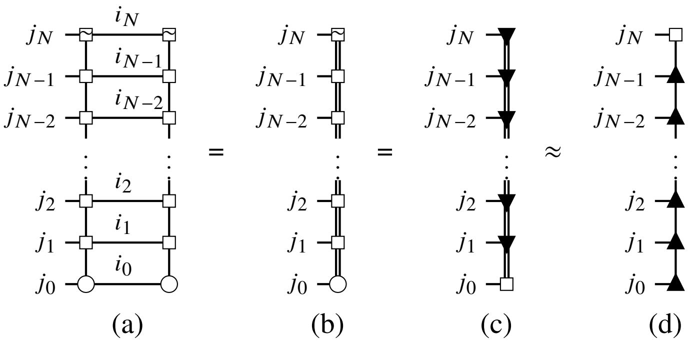

Figure 4.4: Tensor network diagrams depicting the contraction and compression of an MPO-MPS product. (a) The MPO and MPS columns to be contracted together. (b) The resulting MPS after exactly contracting the network along the horizontal bonds indexed by $\{i\}$. We use a double line to represent the merging of the two original vertical lines, as in Eq. (4.15). (c) The new MPS put into right canonical form. (d) The MPS is compressed to a smaller bond dimension starting from the left-most tensor and moving to the right, and the final MPS is now in left canonical form. The double line is reduced to a single line to signify the size reduction of the large vertical bonds down to the desired bond dimension.

Explicit description of transverse MPO-MPS contraction algorithm

We describe a single step of the transverse contraction procedure, which in essence is performing an MPO-MPS contraction and then compressing the resulting MPS to the desired bond dimension D, described in detail in Ref. [75]. We assume that all tensors have been prepared in the appropriate gauge (discussed later) as shown in Fig. 4.3. This algorithm is also the standard boundary contraction algorithm for 2D tensor networks, as described in Ref. [77].

For simplicity, consider the influence functional tensor network for K bath sites, as discussed in the main text. We start with the farthest boundary column MPS (the column for the K^{th} bath site) which is given by

$$P_K(i_0, ..., i_N) = \sum_{\{a\}} A^{(0)}_{a_0}(i_0) A^{(1)}_{a_0,a_1}(i_1) \dots A^{(N)}_{a_{N-1}}(i_N) \tag{4.10}$$

with

$$A^{(0)}_{a}(i) = C^{(K)}_i(a) \tag{4.11a}$$

$$A^{(n)}_{a,a'}(i) = M^{(K)}_i(a', a) \qquad \text{for } n = 1, ..., N-1 \tag{4.11b}$$

$$A^{(N)}_{a}(i) = \tilde{M}^{(K)}_i(a) \tag{4.11c}$$

where $C^{(K)}$ and $M^{(K)}$ are the right-most tensors of the density matrix MPS (Eq. (4.7)) and Liouville evolution operator (Eq. (4.8)), respectively, and $\tilde{M}^{(K)}$ denotes the Liouville evolution operator with traced out bath degrees of freedom.

The next column can be interpreted as an MPO, given by

$$\begin{aligned} &P_{K-1}(j_0, ..., j_N; i_0, ..., i_N) \\ &\qquad = \sum_{\{b\}} B^{(0)}_{b_0}(j_0, i_0)\, B^{(1)}_{b_0,b_1}(j_1, i_1) \ldots B^{(N)}_{b_{N-1}}(j_N, i_N)\ . \end{aligned} \tag{4.12}$$

with

$$B^{(0)}_{b}(j, i) = C^{(K-1)}_{j,i}(b) \tag{4.13a}$$

$$B^{(n)}_{b,b'}(j, i) = M^{(K-1)}_{j,i}(b', b) \qquad \text{for } n = 1, ..., N-1 \tag{4.13b}$$

$$B^{(N)}_{b}(j, i) = \tilde{M}^{(K-1)}_{j,i}(b) \tag{4.13c}$$

Contracting the two columns yields a new MPS,

$$\begin{aligned} &\sum_{\{i_{K-1}\}} P_{K-1}(j_0, ..., j_N; i_0, ..., i_N)\ \times\ P_K(i_0, ..., i_N) \\ &\qquad = \sum_{\{c\}} F^{(0)}_{c_0}(i_0) F^{(1)}_{c_0,c_1}(i_1) \ldots F^{(N)}_{c_{N-1}}(i_N) \end{aligned} \tag{4.14}$$

where the sum over c indicates sums over all (a, b), and

$$F^{(n)}_{c,c'}(i) = \sum_{i} B^{(n)}_{b,b'}(j, i)\, A^{(n)}_{a,a'}(i) \tag{4.15}$$

for all n indexing the tensors in the MPO and MPS. Thus, if the MPS was of bond dimension D_K and the MPO was of bond dimension D_{K-1}, the new MPS has a bond dimension of $D_K D_{K-1}$. We then must compress this new MPS back to one of a lower bond dimension D (again, see Ref. [75] for a more in depth discussion). To do so, we first put the MPS in right or left canonical form.

In left canonical form, all tensors in the MPS (except for the rightmost one) satisfies

$$\sum_{l,u} L_{l,r}(u)\ \ L^*_{l,r'}(u) = \delta_{r,r'} \tag{4.16}$$

where δ is the Kronecker delta. The tensor network diagram depicting Eq. (4.16) is

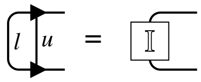

In our tensor network diagrams, we denote tensors in canonical form using triangles, pointing in the direction of the uncontracted leg.

Similarly, in right canonical form, all tensors (except for the leftmost one) satisfies

$$\sum_{r,u} R_{l,r}(u) \;\; R^*_{l',r}(u) = \delta_{l,l'} \tag{4.17}$$

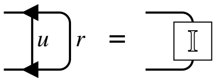

We are able to define canonical forms because tensor networks have a gauge degree of freedom. This means that the choice of tensors in the network is not unique. One can see this by introducing a set of matrices X, X^{-1}, which clearly satisfy $XX^{-1} = \mathbb{I}$, along any line connecting two tensors.

Canonicalization can be performed using singular value decomposition (SVD). Suppose that we are interested in written the MPS in left canonical form, and that all tensors left of the n^{th} tensor are already in left canonical form. We then take the SVD of the n^{th} tensor,

$$F^{(n)}_{c,c'}(i) = \sum_{\sigma} U_{c,\sigma}(i)\, \Sigma_{\sigma} V^{\dagger}_{\sigma,c'} \tag{4.18}$$

where Σ are the singular values from the decomposition of the tensor. Note that by definition, U is left canonical, as desired, and thus will be used as the new n^{th} tensor. The remaining matrices are then pushed into the $(n+1)^{\text{th}}$ tensor,

$$F^{(n)}_{c,\sigma}(i) \leftarrow U_{c,\sigma}(i) \tag{4.19}$$

$$F^{(n+1)}_{\sigma,c''}(i) \leftarrow \sum_{c'} \Sigma_{\sigma} V^{\dagger}_{\sigma,c'} F^{(n+1)}_{c',c''}(i) \;\; . \tag{4.20}$$

By iteratively performing this operation starting from the left-most tensor all the way to the right end of the MPS, the MPS is put into left canonical form. The procedure for expressing the MPS in right canonical form is analogous.

MPS compression is performed in the same way, except only the largest D singular values are retained, generating some error. For minimal compression errors, the MPS must be in left (right) canonical form prior to performing the iterative compression procedure starting from the right (left) end.

In Fig. 4.3 we depict the contraction of the columns of the (1+1)D influence functional tensor network. The rows are initialized in left canonical form. After the two right-most columns are contracted, the product is canonicalized and the compressed using the procedure discussed above. Because of the vertical orientation, the left and right canonical forms are depicted by triangles pointing upwards and downwards along the column.

Influence functional transverse contraction around an arbitrary site

Sometimes the site whose dynamics we are interested in may be at the middle of the MPS representation of the system (e.g. in the hardcore boson model). Thus, we need to generalize the tensor network diagrams presented in the main text to consider IFs for subsystems at arbitrary lattice site i.

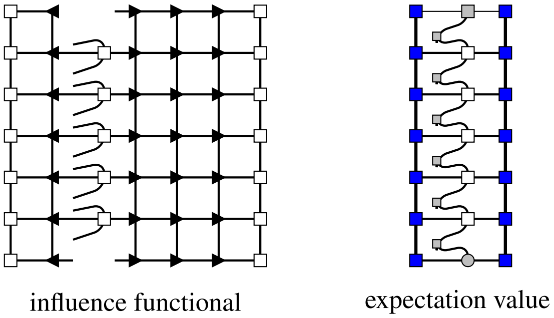

Figure 4.5: Influence functional methods for dynamics of arbitrary site in 1-D chain. (left) Tensor network showing generalized IF isolating dynamics at the $i = 3$ lattice site. Triangles denote gauging of tensors along the row, as defined in Fig. 4.3 in the main text. (right) Tensor network computing expectation value using [blue] left and right environment columns obtained separately using the iterative contraction scheme described above, [white] original tensors at site i dictating interactions of both environment columns with the site itself and the environments with each other, and [gray] on-site terms including [circle] the initial state and [square] time evolution operators and the observable of interest (see Fig. 4.1). It is cheapest to contract this network vertically from the row at one end and continuing to the other end. Note that in using this method, one does not explicitly compute the IF itself.

If the Hamiltonian only consists of nearest-neighbor interactions, the IFs from the two sides of site i are separable and can be computed independently. Otherwise, the tensor network can be initialized as shown in Fig. 4.5, and one contracts inwards from the outer columns separately. Once only the column corresponding to the isolated site is left, one can now include on-site terms (initial state, on-site time evolution operators, observable) such that the network now corresponds to the expectation value of the observable at the desired time step (a scalar). The cost of contracting this network scales like $O(D_I^3)$, which is much cheaper than explicitly computing the full IF first and using it to compute the observable expectation values.

4.3 Results

Spin-boson model

First, we consider the well-studied spin-boson model, in which a single spin is linearly coupled to a bath of non-interacting harmonic oscillators,

$$H_{SB} = \Delta S_X + \int d\omega \left[S_Z(g(\omega)a_\omega + g(\omega)^* a_\omega^\dagger) + \omega a_\omega^\dagger a_\omega \right] \tag{4.21}$$

where Δ is the tunneling strength between the two subsystem states, and the system-bath coupling strength $g(\omega)$ is determined from the bath spectral density function $J(\omega)$ by

$$|g(\omega)|^2 = \frac{1}{\pi} J(\omega) \ . \tag{4.22}$$

In the case of an Ohmic bath with exponential cut-off,

$$J(\omega) = \frac{\pi}{2} \alpha \omega e^{-\omega/\omega_c} \ , \tag{4.23}$$

where α is the Kondo parameter and ω_c is the cut-off frequency. Typically one computes the dynamics from a factorized initial state $|\rho_s(s_{t_0})\rangle\rangle\, |\rho_b(b_{t_0};\beta)\rangle\rangle$, where $|\rho_b(b_{t_0};\beta)\rangle\rangle$ is the Gibbs thermal state of the isolated bath at finite temperature β. In this paper, we set $\Delta = 1.0$, $\omega_c = 7.5$, and $\beta = 5.0$.

The spin-boson model exhibits a dynamical phase transition from thermalizing to localizing behavior at $\alpha = 1.0 + O(\Delta/\omega_c)$ [83], and is often cited as an example of physically relevant non-Markovian dynamics [23, 25]. Because of the linear coupling and harmonic bath, the IF may be computed via an analytical expression. There already exist several methods of obtaining accurate dynamics for various bath coupling strengths and spectral densities [46, 55, 56, 83, 84]. We thus use this model as a benchmark to understand the properties of the influence functional, its compressibility, and the accuracy of the tensor network contraction approximation.

MPS of analytical IF

We first write the analytical expression of the influence functional for the spin-boson model as matrix product state (MPS). Denoting the system basis $|s\rangle\rangle \equiv |s^+\rangle \langle s^-|$ where $|s^\pm\rangle \in \{|1\rangle, |-1\rangle\}$ and $|1\rangle, |-1\rangle$ are the eigenstates of the S_Z operator, the influence functional can be written as

$$I_{SB} = \exp\left\{ -\sum_{k=1}^{N} \sum_{k'=1}^{k} (s_{t_k}^{+} - s_{t_k}^{-})(\eta_{kk'} s_{t_{k'}}^{+} - \eta_{kk'}^{*} s_{t_{k'}}^{-}) \right\} . \tag{4.24}$$

This explicitly shows the form of the influence functional as the Boltzmann weight of a complex spin Hamiltonian with the spins interacting along the time axis via the long-range pairwise "interaction" $\eta_{kk'}$. We can further factorize the weights into contributions for times (t_1), $(t_1, t_2), \ldots, (t_1, t_N)$, giving

$$\begin{aligned} I_{SB} = &\prod_{k=1}^{N} I_0(s_{t_k}^{\pm}) \prod_{k=1}^{N-1} I_1(s_{t_k}^{\pm}, s_{t_{k+1}}^{\pm}) \ \ldots \\ &\prod_{k=1}^{N-m} I_m(s_{t_k}^{\pm}, s_{t_{k+m}}^{\pm}) \cdots \prod_{k=1}^{1} I_N(s_{t_k}^{\pm}, s_{t_{k+N-1}}^{\pm}) \end{aligned} \tag{4.25}$$

where

$$I_m = \exp\left\{ -(s_{t_{k+m}}^{+} - s_{t_{k+m}}^{-})(\eta_{k+m,k} s_{t_k}^{+} - \eta_{k+m,k} s_{t_k}^{-}) \right\} . \tag{4.26}$$

The $\eta_{kk'}$ interaction terms can be derived from the spectral density of the bosonic bath. Expressions for $\eta_{kk'}$ are given in Eq. (12) of Ref. [46], where they use Δt instead of ϵ to denote the timestep. For many smooth spectral densities, $\eta_{k,k+m}$ decays quickly with respect to m.

In QuAPI, one considers interactions $\eta_{kk'}$ for times k, k' within $m_{\max}$ of each other, where $m_{\max}$ is treated as a convergence parameter [46]. Then, one can evaluate the influence functional (or its effect on the dynamics [56, 85]) with a computational cost exponential in $m_{\max}$. Since QuAPI often converges rapidly with $m_{\max}$, one also expects the matrix product state representation of the IF (Eq. (4.5)) to be compressible to small bond dimension. One way to verify this would be to construct the large influence functional object as an exact tensor, and then compress it into a matrix product state. Because of the exponential storage of the tensor with time, this is possible only for a small number of time points N. Alternatively, one could build the influence functional iteratively (i.e. piece by piece in Eq. (4.25)) and compress it at each step. This is the idea behind TEMPO and related methods [64, 83] which exploit the compressibility of the augmented density matrix, the influence functional applied to the subsystem density matrix, i.e.

$$A(s_{t_1}, \ldots, s_{t_{m_{\max}}}) = \sum_{s_{t_0}} I(s_{t_0}, \ldots, s_{t_{m_{\max}}}) \rho_s(s_{t_0}) , \tag{4.27}$$

Note that because I is composed of commuting pieces, there are many possible decompositions and thus sequences of iterative constructions.

In this work, we construct the analytical IF MPS in a naive fashion and include terms in the order $I = I_0 I_1 \dots I_{N-1}$. More specifically, we start with the I_0 terms in the form of a product state (MPS with bond dimension 1), multiply it by each of the subsequent I_m, and then compress it into an MPS after each one is applied. Multiplying by I_m can be viewed as multiplication by an MPO where the tensors are very sparse. The two-body terms I_m for $m > 1$ are long-range operators, and must be padded with identities to skip over the times in the middle. More explicitly, the MPOs are

$$I_m(s_{t_k}, s_{t_{k+m}}) = \sum_v \left[I_m^{(0)}(s_{t_k})\right]_v \left[I_m^{(1)}(s_{t_{k+m}})\right]_v \tag{4.28}$$

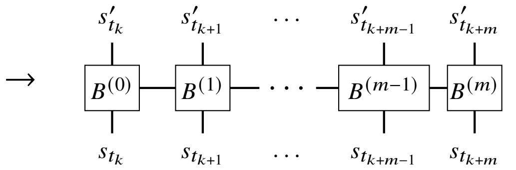

where we first decompose I_m into two tensors (eg. via SVD or QR decomposition) and then define the tensors in the MPO as

$$B_v^{(0)}(s', s) = \sum_j \left(\delta_{s,s'}\delta_{s,v}\right) \left[I_m^{(0)}(s)\right]_v \tag{4.29}$$

$$B_v^{(m)}(s', s) = \sum_j \left(\delta_{s,s'}\delta_{s,v}\right) \left[I_m^{(1)}(s')\right]_v \tag{4.30}$$

$$B_{v,v'}^{(i)}(s', s) = \delta_{v,v'}\delta_{s,s'} \quad \forall i \in [1, ..., m-1] \ . \tag{4.31}$$

In diagrammatic form, the MPS for an IF with 6 time steps is

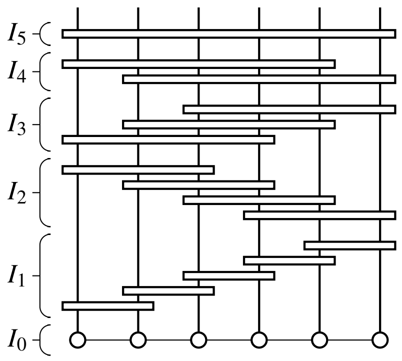

In our contraction scheme, we start from the bottom row and contract upwards. However, because each I_m factor commutes with the rest, other choices of ordering are possible and are the basis of algorithms such as TEMPO [64, 83].

Compressibility of analytical IF

To verify the compressibility of the IF itself, we approximate I_{SB} as an MPS of bond dimension D_I using an iterative scheme (see Appendix) and determine the error in the resulting on-site dynamics, using the $D_I = 128$ result as reference. Here and throughout the paper, the error is computed as the r.m.s. deviation of the dynamics of an observable with respect to some reference over the time interval of the plot. The results are shown in Fig. 4.6, and compares convergence with respect to D_I for infinite m_{max}, as well as convergence with respect to m_{max} for fixed $D_I = 128$. We find that the analytical influence functional is relatively compressible, regardless of coupling strength. Even at a small bond dimension of $D_I = 16$, the correct behavior of the dynamics in both the thermalization and localization regimes is captured. Compared to results for small m_{max}, the MPS algorithm yields slightly more accurate dynamics near the localization transition. The key advantage of using a compressed matrix representation, as opposed to truncating $\eta_{k,k+m}$ at some m_{max} as in QUAPI, is that this does not eliminate the effects of long-range memory [83]. Overall, this result confirms that for certain spectral densities, the influence functional can be efficiently written as a low-rank MPS, consistent with the findings from TEMPO [64, 83].

Finite size harmonic bath

We now use the spin-boson model to examine if the IF can be constructed efficiently from our tensor network contraction scheme. To do so, we consider a finite size harmonic bath with K sites, where the bosons are capped to some finite number of states. For small baths and small boson cap, the transverse contraction can be performed without compression, allowing a numerical test of the compression procedure. The analytical IF, assuming bosons with infinite boson cap, can also be computed. The bath is characterized by the discretized spectral density,

$$J_D(\omega) = \sum_j \frac{J(\omega)}{\rho(\omega)} \delta(\omega - \omega_j) \ .$$

We use a linear discretization of the bath sites, such that the bath density is $\rho(\omega) = K/\omega_m$, where ω_m is the maximum boson frequency used. Here, we set $\omega_m = 10$.

The discretized Hamiltonian (in the star geometry) is given by

$$H_{SB} = \Delta S_X + \sum_{j=1}^{K} \left[S_Z (g_j a_j + g_j^* a_j^\dagger) + \omega_j a_j^\dagger a_j \right] \tag{4.32}$$

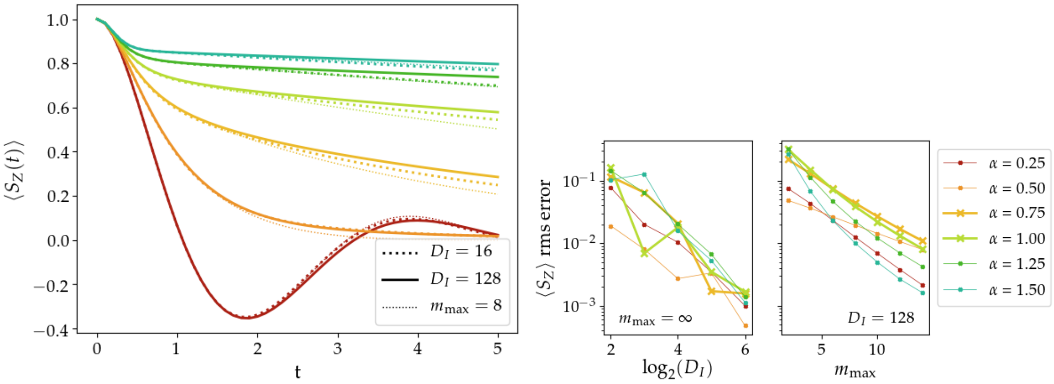

Figure 4.6: Spin dynamics of spin-boson model using the analytical IF and errors from IF compression. (top) Dynamics obtained using the analytical IF capped to $m_{\max}$ and compressed to bond dimension D where (thick dotted) $D = 16, m_{\max} = \infty$, (thin dotted) $D = 128$, $m_{\max} = 8$, and (solid) $D = 128$, $m_{\max} = \infty$, for various coupling strengths α. (bottom, left) R.m.s. error for the analytical IF with respect to D. (bottom, right) R.m.s error for capped IFs with respect to $m_{\max}$ computed using $D = 128$. The errors are obtained using dynamics from the IF with no cap ($m_{\max} = \infty$) and $D = 128$ as reference. The error of the complete IF with respect to D is independent of coupling strength. In contrast, the error for finite $m_{\max}$ is larger near the localization transition. These calculations are for $N = 50$ time steps of size $\epsilon = 0.1$. The system parameters are $\Delta = 1.0$, bath inverse temperature $\beta = 5.0$, and an Ohmic bath spectral density with exponential cut-off $\omega_c = 7.5$.

where g_j is the coupling strength, ω_j is the frequency, and $a_j, a_j^\dagger$ are the creation and annihilation operators of the jth phonon in the discretized bath, and can be represented using the matrix product operator of bond dimension $D_W = 3$

$$\begin{bmatrix}\Delta S_X & S_Z & \mathbb{I}\end{bmatrix}\begin{bmatrix}\mathbb{I} & 0 & 0\\ g_1a_1+g_1^*a_1^\dagger & \mathbb{I} & 0\\ \omega_1 a_1^\dagger a_1 & 0 & \mathbb{I}\end{bmatrix}\quad\cdots\quad\begin{bmatrix}\mathbb{I}\\ g_Ka_K+g_K^*a_K^\dagger\\ \omega_K a_K^\dagger a_K\end{bmatrix} \tag{4.33}$$

First, we consider a system with only 2 bath modes (in the number basis) each with a maximum boson number of 2, for $N = 100$ time steps of size $\epsilon = 0.05$. For this small system, we use the exact time evolution operator of L_{bs} and compute the IF by exact transverse contraction, applying compression only to the final IF object. Fig. 4.7(a) shows the error of the exact IF compressed to bond dimension D_I. As expected, the IF is much less compressible than with the continuous bath density in the last section, due to the small bath size. The error decreases only slightly until it drops suddenly once the bond dimension is large enough to capture the IF exactly, and further, the compression error increases with α. We then perform the same

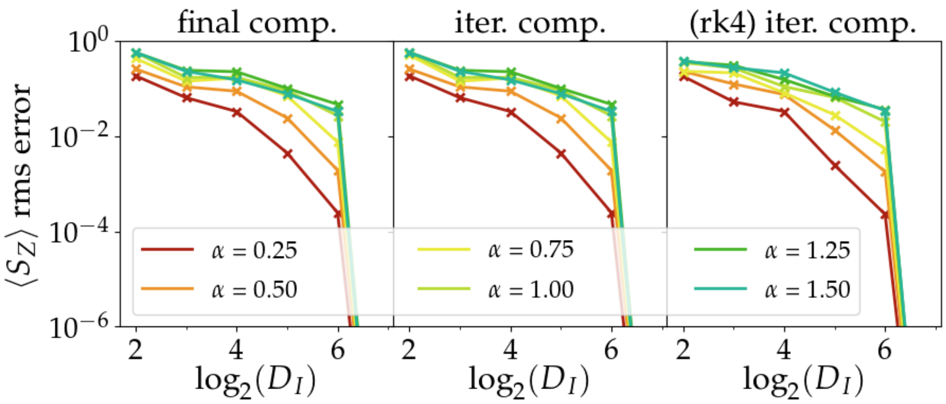

Figure 4.7: Comparisons of average error in $\langle S_Z(t) \rangle$ with respect to reference direct time evolution results for the IF where the IF is (left) constructed using exact time evolution, contracted exactly, and finally compressed to bond dimension D_I at the end, and where the IF is constructed with (middle) exact time evolution and (right) RK4 time evolution, but iteratively contracted and compressed using the transverse compression scheme. In these calculations, we use $\Delta = 1.0$, bath inverse temperature $\beta = 5.0$, cut-off frequency $\omega_c = 7.5$, and assume a discrete Ohmic bath with 2 modes at $\omega = [5.0, 10.]$. The bosonic bath sites are approximated to have only a maximum boson number of 2. Time evolution is performed using $N = 100$ time steps with a time step of $\epsilon = 0.05$. The plots show that for small bath sizes, the error in the iterative compression scheme is dominated by the lack of compressibility of the final IF.

comparison but for IFs computed by transverse contraction with compression, for both exact and RK4 time evolution. As seen in Fig. 4.7, the errors are comparable to those obtained when compressing the final exact IF. This indicates that for this small problem, there is little additional error added by the iterative contraction, and that the time-step error is negligible: the error is dominated by the compressibility of the final IF itself (which is low when the bath size is small).

Next, we investigate systems with larger bath sizes in Fig. 4.8(a). We first examine the time-dynamics of the analytical IF (i.e. without any boson cap, and without transverse contraction) for a discretized spectral density with 11 bath sites, as well as the IF computed by transverse contraction, using a boson cap of 2. Because the system size is so small, the exact reference dynamics for a boson cap of 2 can be generated by direct MPS time evolution (here, we use $D_\rho = 64$ and Hamiltonian time evolution). From this comparison, we observe two things. First, compared to using the continuous bath density, the error of the analytical IF dynamics is increased, although it is still somewhat compressible. For the same D_I, the errors

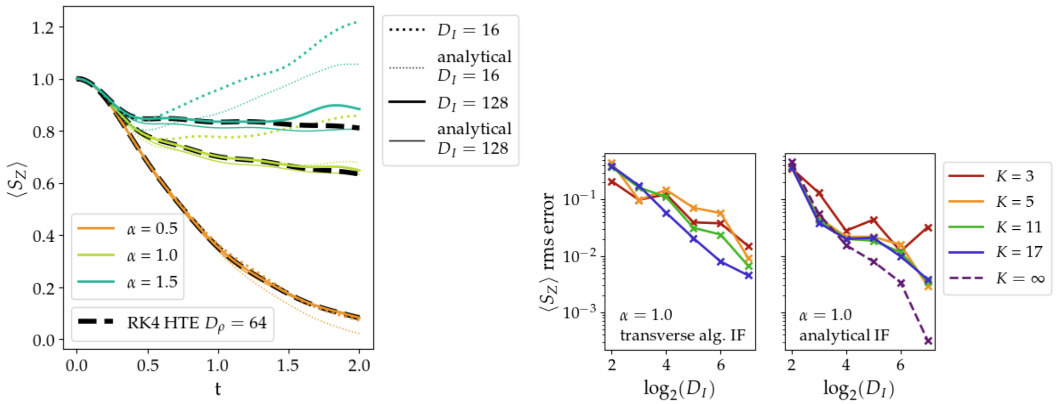

Figure 4.8: Spin dynamics of spin-boson model using IF obtained using tensor network methods. (top) Expectation values $\langle S_Z(t) \rangle$ obtained from the analytical IF (thinner colored lines) and IF from transverse contraction (thicker colored lines) for bath size $K = 11$ with $\alpha = 0.5$, 1.0, and 1.5. The thick dashed line corresponds to reference dynamics from direct time evolution of the density matrix. The transverse contraction scheme introduces an additional error with respect to the analytical result, which increases with α. (bottom) Time-averaged error in IF dynamics with respect to $D_I = 128$ results, obtained using (left) the transverse contraction scheme and (right) the analytical IF for the finite bath of size K, respectively. The $K = \infty$ bath size corresponds to the continuous bath.

using transverse contraction are larger, suggesting that at intermediate points in the transverse contraction, there is more time-like entanglement than in the final IF itself. In Fig. 4.8(b), we show the time-averaged error of the IF dynamics as a function of the number of bath sites. We see that this error decreases as the number of bath sites increases, both for the analytical IF and the transverse contraction. This is consistent with the idea that smoother bath densities are more "compressible".

1-D hard-core boson model

We next study dynamics of a 1D hard-core boson (HCB) lattice model, in which each lattice site is either unoccupied ($|0\rangle$) or occupied ($|1\rangle$) by a single bosonic particle. We consider the Hamiltonian

$$H_{HCB} = \sum_j \left[-J(a_j^\dagger a_{j+1} + h.c.) + U n_j n_{j+1} + \frac{K}{2} n_j j^2 \right] \tag{4.34}$$

where $a_j^\dagger = |1\rangle \langle 0|$, $a_j = |0\rangle \langle 1|$ are hard-core boson creation and annihilation operators at the j^{th} lattice site, and $n_j = a_j^\dagger a_j$ is the number operator. This Hamiltonian is intended to mimic the Bose-Hubbard model dynamics often simulated by cold-atom experiments, which was shown to be difficult to compute using direct time evolution

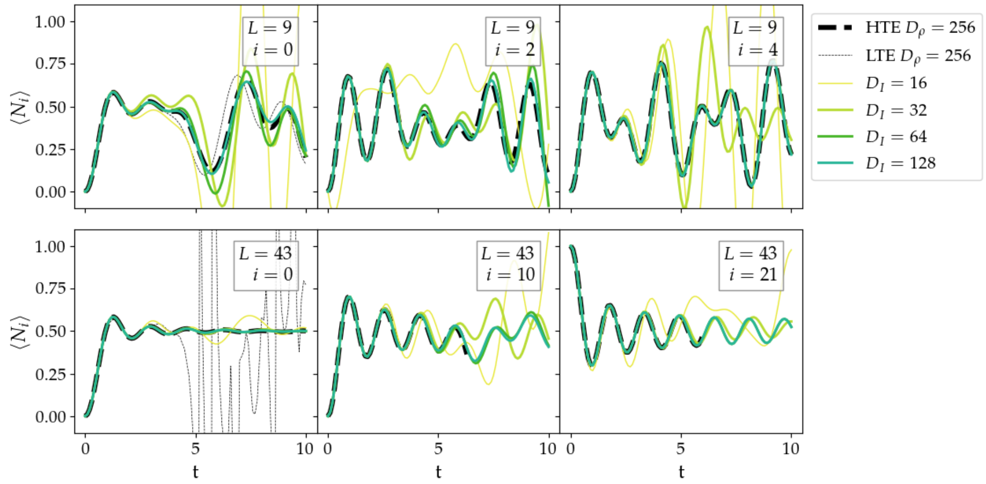

Figure 4.9: Expectation values $\langle N_i(t) \rangle$ for the hard-core boson model with $U = 0$ for system sizes (top) $L = 9$ and (bottom) $L = 43$ for sites $i = \{0, L/2, L/4\}$ obtained using the iterative contraction scheme with bond dimension D_I as labeled. The thick dashed line is the dynamics obtained by direct Hilbert-space time evolution, compressed to bond dimension $D_\rho = 256$, only shown for times where the results are converged. The thin dashed line, shown only in the left-most plots but with similar behavior for all, is the dynamics obtained by direct time evolution of the full density matrix. Unphysical behavior suggests loss of positivity of the density matrix. For these calculations, the initial state is a pure product state with alternating spins, $|0, 1, 0, 1, \ldots\rangle$. Time evolution is performed using Trotter steps with a $N = 100$ time steps of $\Delta t = 0.1$. Consistent with earlier observations, larger D_I is needed to accurately capture the IF for smaller bath sizes. However, as shown in the $L = 43, i = 21$ simulation, the IF of comparable bond dimension can simulate dynamics for longer times than direct HTE.

methods [86], where the on-site interaction term is replaced by a nearest-neighbor interaction term. We also include a harmonic potential term to emulate a cold atom trap.

The corresponding matrix product operator of bond dimension $D_W = 4$ is

$$
\begin{aligned}
H_{HCB} = &\begin{bmatrix} \frac{K}{2} n(-M)^2 & n_{-M} & a^\dagger_{-M} & a_{-M} & \mathbb{I} \end{bmatrix} \times \\
&\times \begin{bmatrix} \mathbb{I} & 0 & 0 & 0 & 0 \\ U n_{-M+1} & 0 & 0 & 0 & 0 \\ -J a_{-M+1} & 0 & 0 & 0 & 0 \\ -J a^\dagger_{-M+1} & 0 & 0 & 0 & 0 \\ \frac{K}{2} n(-M+1)^2 & n_{-M+1} & a^\dagger_{-M+1} & a_{-M+1} & \mathbb{I} \end{bmatrix} \ldots \begin{bmatrix} \mathbb{I} \\ U n_M \\ -J a_M \\ -J a^\dagger_M \\ \frac{K}{2} n(M)^2 \end{bmatrix}
\end{aligned}
\tag{4.35}
$$

We assume a pure initial state $|0, 1, 0, \ldots\rangle$ such that there is one particle at every other lattice site, and set the parameters $J = 1$ and $K = 10^{-2}$ while varying U. For non-zero interaction term U, there is no analytical form for the IF.

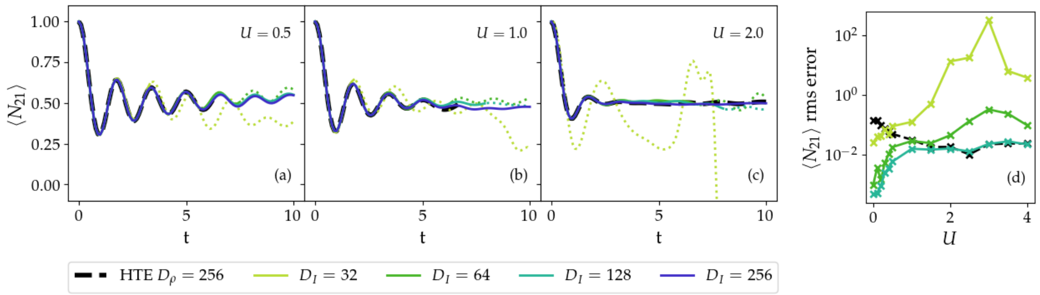

Figure 4.10: Results for hard-core boson model for nonzero U. (a,b,c) Expectation values of the site-occupancy $\langle N_i(t) \rangle$ for the hard-core boson model of length $L = 43$ at lattice site $i = 21$ for different coupling strengths $U = 0.5$, 1.0, and 2.0. Lines become dotted after divergence of >0.03 with respect to the $D_I = 256$ IF results. (d) The r.m.s. errors with respect to the $D_I = 256$ IF results as a function of U. Simulation parameters are otherwise the same as in Fig. 4.9. Compared to the $U = 0$ case, a larger bond dimension is needed, particularly at around $U = 3.0$ where the r.m.s. error peaks. In contrast, the HTE dynamics converge more quickly with increasing U.

We compute the dynamics of $\langle N_i(t) \rangle$ at lattice sites $i = \{0, L/4, L/2\}$, where L is the length of the 1-D chain. For longer chains, the rapid growth of entanglement means that direct MPS time evolution (either using Hamiltonian evolution, denoted HTE or Liouvillian evolution, denoted LTE) with a finite D_ρ can only obtain converged dynamics up to a finite time. We consider two chain lengths: $L = 9$ where the converged HTE MPS dynamics can be used as a reference, and $L = 43$, where the HTE MPS dynamics appear to be not fully converged (no longer within 0.03 of $D_\rho = 512$ results) for the full simulated time. To obtain the dynamics using the influence functional method, we partition the lattice such that site i is the subsystem of interest and the remaining sites are the bath.

The $U = 0$ dynamics for $L = 9$ and $L = 43$ is shown in Fig. 4.9. Direct MPS LTE shows unphysical behavior for large system sizes, presumably because of the loss of positivity at some point in the dynamics. In contrast, the dynamics obtained using the iteratively contracted IF are more stable, highlighting the innate compressibility of the time evolution tensor network along the time axis as opposed to the spatial axis. For $L = 9$, the IF dynamics only appears to begin to converge by $D_I = 128$ with respect to the (exact) HTE dynamics, having less than 0.03 r.m.s error in $\langle N_i(t) \rangle$ over the simulated time interval and deviations within 0.08. Thus, there appears to be no significant advantage to using the IF method over direct HTE for small system sizes. Conversely, for the $L = 43$ system, the IF dynamics are converged with respect to $D_I = 256$ results by $D_I = 64$, with less than 0.02 r.m.s error and a maximum deviation of 0.04 for $i = 10$ and less than 0.001 r.m.s error and a maximum deviation of 0.004 for $i = 21$. Note that the $i = 10$ dynamics converge more slowly because effectively the site is coupled to two separate baths, one of which is small. However, the IF method still outperforms direct HTE.

For $U > 0$, as shown in Fig. 4.10, the $D_I = 64$ results appear less converged than the non-interacting case, but the $D_I = 128$ results are converged (r.m.s. errors of the $D_I = 128$ observable dynamics with respect to the $D_I = 256$ results, for times longer than that accessible by direct time evolution, are less than 0.03). This shows that the IF-based dynamics can produce the correct oscillatory behavior of the density as a function of time, which is not captured by the direct MPS time evolution despite using a larger bond dimension (this difficulty with the long time oscillatory tail has previously been noted in other cold atom simulations [86]). However, while the IF method notably outperforms direct HTE at small U, the two methods become comparable at larger $U \approx 1.5$ once the oscillatory tail is sufficiently dampened.

Entanglement spectrum

The accuracy of the transverse contraction scheme depends on the entanglement in the time-like direction. Recall that our contraction algorithm starts with the farthest column (an MPS), and at each iteration another column is contracted into this boundary. Thus, as the iteration number increases, the boundary column represents more of the bath. For both the spin-boson model and HCB model, we measure the singular values at the middle of the boundary "bath" MPS during each step of the iterative contraction scheme. The entanglement entropy (EE) and spectrum of the singular values (normalized so that $\sum_i |s_i|^2 = 1$) are plotted in Fig. 4.11. For the spin-boson model, only results for $\alpha = 1.0$ are shown; the only notable difference for other α is that the EE increases with α. Consistent with the observations in our simulations above, the EE decreases as one increases bath size. For the SB model, the EE decreases with increased number of bath sites in the discretization until convergence. For the HCB model, *only if* sufficiently large enough bond dimension is used does the EE decrease with increasing iteration number. Otherwise, the EE stays at a large value throughout the contraction scheme and the gap between the

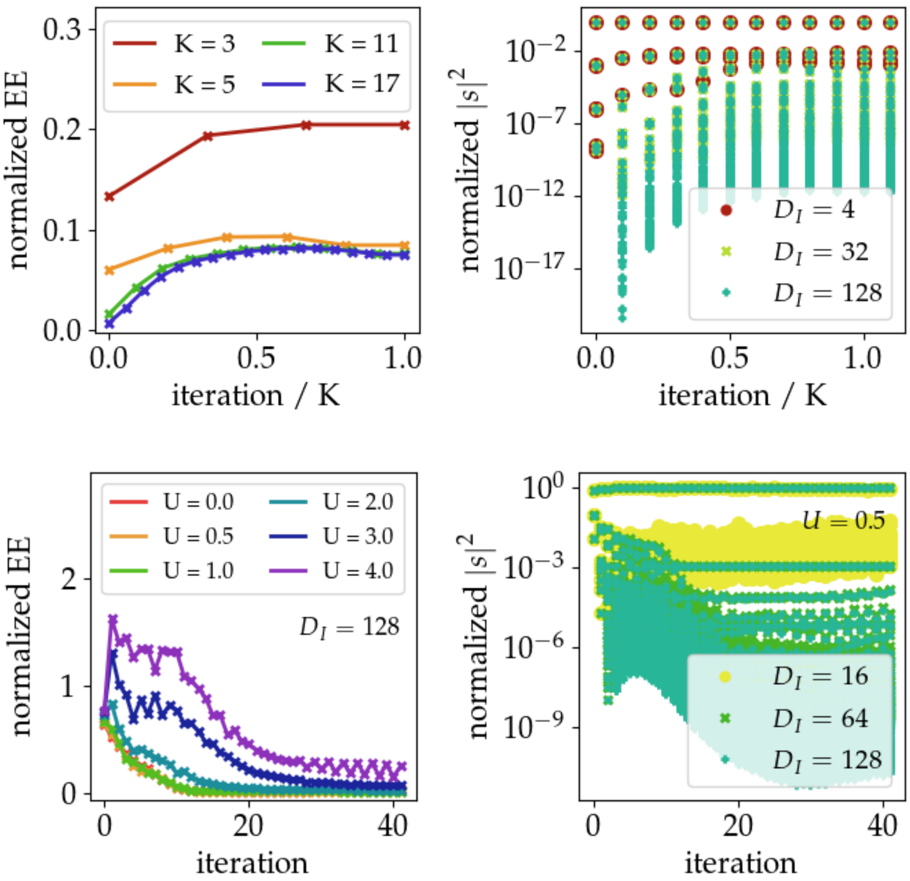

Figure 4.11: Measurements of entanglement at the middle of the "bath" boundary column MPS at each step of the iterative IF contraction scheme. (Top left) Normalized entanglement entropy for the SB model ($\alpha = 1.0$) for various bath sizes. As bath size increases, the EE of the IF decreases, converging to some finite value. (Top right) Normalized singular values for bath size $K = 11$ for various bond dimensions D_I used in the contraction scheme. (Bottom left) Normalized entanglement entropy for the hard-core boson model with $L = 43$, with the IF contractions starting from the right edge, plotted for different values of U. The decrease in EE with respect to iteration shows that EE decreases with system size. (Bottom right) Normalized singular values for the hardcore-boson model with $L = 43$ and $U = 0.5$. Surprisingly, for insufficient D_I, the singular values take on large and incorrect values, yielding an artificially large EE.

dominant and non-dominant singular values decreases; this makes the EE of the smaller D_I approximation larger than that of the larger D_I approximation. Overall, this suggests that the final compressibility of the IF emerges from the cancellation of many different correlations as one iteratively contracts out the bath.

4.4 Conclusions

In this work, similar to some other recent contributions [63, 66], we have used the representation of the influence functional within the tensor network language, motivated by the limitations of modeling spatial entanglement growth in quantum dynamics. We have discussed a transverse tensor network contraction algorithm that allows us to compute the influence functional in cases where the analytical form is not known. We have applied this algorithm to study both the canonical spin-boson model as well as an interacting hard-core boson chain where the bath is not quadratic (i.e. interacting). We find that the compressibility of the influence functional is controlled by several factors, principally the size of the bath, as well as the nature of the interactions. In addition, although the time-like correlations may ultimately be short-ranged in the final influence functional, during the transverse tensor network contraction to construct it, it is possible to proceed through intermediate quantities with larger time-like entanglement. This suggests a complicated picture where time-like correlations first accumulate as the bath is integrated out before finally cancelling out in the influence functional itself. In the regimes where the influence functional and all intermediate quantities are compressible, as in some interaction regimes in the interacting hardcore boson model we have studied, it is possible to outperform conventional tensor network time evolution methods at longer times.

There are many possible directions for further investigation. For example, there are natural extensions to higher-dimensional interacting problems and fermionic systems, as well as more complicated correlation functions. Also, a better theoretical understanding of how correlations grow and cancel out in the transverse contraction scheme may lead to a deeper understanding of the generation of memory in quantum dynamics, the master equation formalism [29], improved contraction schemes, and ultimately new algorithms to carry out longer time dynamical simulations.

References

[1] G. Vidal, “Efficient simulation of one-dimensional quantum many-body systems,” Phys. Rev. Lett. **03**, 040502 (2004).

[2] S. White and A. E. Feiguin, “Real-time evolution using the density matrix renormalization group,” Phys. Rev. Lett. **93**, 076401 (2004).

[3] A. J. Daley, C. Kollath, U. Schollwock, and G. Vidal, “Time-dependent density-matrix renormalization-group using adaptive effective Hilbert spaces,” J. Stat. Mech.: Theor. Exp. , P04005 (2004).

[4] U. Schollwöck and S. R. White, "Methods for time dependence in DMRG," AIP Conference Proc. **816**, 155 (2006).

[5] E. Ronca, Z. Li, C. Jimenez-Hoyos, and G. K.-L. Chan, "Time-step targeting time-dependent and dynamical density matrix renormalization group algorithms with ab initio Hamiltonians," J. Chem. Theory Comput. **13**, 5560–5571 (2017).

[6] J. Haegeman, C. Lubich, I. Oseledets, B. Vandereycken, and F. Verstraete, "Unifying time evolution and optimization with matrix product states," Phys. Rev. B **94**, 165116 (2016).

[7] E. Leviatan, F. Pollmann, J. H. Bardarson, D. A. Huse, and E. Altman, "Quantum thermalization dynamics with matrix product states," arXiv preprint cond-mat.stat-mech/1702:088942 (2017).

[8] C. H. Mak and D. Chandler, "Solving the sign problem in quantum Monte Carlo dynamics," Phys. Rev. A **41**, 5709–5712 (1998).

[9] P. Werner, T. Oka, and A. J. Millis, "Diagrammatic Monte Carlo simulation of nonequilibrium systems," Phys. Rev. B **79**, 035320 (2009).

[10] L. Mühlbacher and E. Rabani, "Real-time path integral approach to nonequilibrium many-body quantum systems," Phys. Rev. Lett. **100**, 176403 (2008).

[11] M. Schirò and M. Fabrizio, "Real-time diagrammatic Monte Carlo for nonequilibrium quantum transport," Phys. Rev. B **79**, 153302 (2009).

[12] F. Rossi, A. D. Carlo, and P. Lugli, "Microscopic theory of quantum-transport phenomena in mesoscopic systems: A Monte Carlo approach," Phys. Rev. Lett. **80**, 3348 – 3351 (1998).

[13] G. Cohen, E. Gull, D. R. Reichman, and A. J. Millis, "Taming the dynamical sign problem in real-time evolution of quantum many-body problems," Phys. Rev. Lett. **115**, 266802 (2015).

[14] H.-T. Chen, G. Cohen, and D. R. Reichman, "Inchworm Monte Carlo for exact nonadiabatic dynamics. I. Theory and algorithms," J. Chem. Phys. **146**, 054105 (2017).

[15] H.-T. Chen, G. Cohen, and D. R. Reichman, "Inchworm Monte Carlo for exact nonadiabatic dynamics. II. Benchmarks and comparison with established methods," J. Chem. Phys. **146**, 054106 (2017).

[16] H. Wang, M. Thoss, and W. H. Miller, "Systematic convergence in the dynamical hybrid approach for complex systems: A numerically exact methodology," J. Chem. Phys. **115**, 2979 (2001).

[17] M. Thoss, H. Wang, and W. H. Miller, "Self-consistent hybrid approach for complex systems: Application to the spin-boson model with Debye spectral density," J. Chem. Phys. **115**, 2991 (2001).

[18] T. C. Berkelbach, D. R. Reichman, and T. E. Markland, "Reduced density matrix hybrid approach: An efficient and accurate method for adiabatic and non-adiabatic quantum dynamics," J. Chem. Phys. **136**, 034113 (2012).

[19] S. Nakajima, "On quantum theory of transport phenomena: Steady diffusion," Progress Theor. Phys. **20**, 948–959 (1958).

[20] R. Zwanzig, "Ensemble method in the theory of irreversibility," J. Chem. Phys. **33**, 1338–1341 (1960).

[21] G. Lindblad, "On the generators of dynamical semigroups," Commun. Math. Phys. **48**, 119–130 (1976).

[22] V. Gorini, A. Kossakowski, and E. Sudarshan, "Completely positive dynamical semigroups of n-level systems," J. Math. Phys. **17**, 821–825 (1976).

[23] H. Breuer and F. Petruccione, *The Theory of Open Quantum Systems* (Oxford University Press, 2002).

[24] G. Clos and H.-P. Breuer, "Quantification of memory effects in the spin-boson model," Phys. Rev. A **86**, 012115 (2012).

[25] I. D. Vega and D. Alonso, "Dynamics of non-Markovian open quantum systems," Rev. Mod. Phys. **89**, 015001 (2017).

[26] A. Shabani and D. A. Lidar, "Completely positive post-Markovian master equation via a measurement approach," Phys. Rev. A **71**, 020101 (2005).

[27] S. Maniscalco and F. Petruccione, "Non-Markovian dynamics of a qubit," Phys. Rev. A **73**, 012111 (2006).

[28] S. Barnett and S. Stenholm, "Hazards of reservoir memory," Phys. Rev. A **64**, 033808 (2001).

[29] Q. Shi and E. Geva, "A new approach to calculating the memory kernel of the generalized master equation for an arbitrary system-bath coupling," J. Chem. Phys. **119**, 12063 (2003).

[30] A. Kelly, A. Montoya-Castillo, L. Wang, and T. E. Markland, "Generalized quantum master equations in and out of equilibrium: when can one win?" J. Chem. Phys. **144**, 184105 (2016).

[31] E. Mulvihill, X. Gao, Y. Liu, A. Schubert, B. D. Dunietz, and E. Geva, "Combining the mapping Hamiltonian linearized semiclassical approach with the generalized quantum master equation to simulate electronically nonadiabatic molecular dynamics," J. Chem. Phys. **151**, 074103 (2019).

[32] E. Mulvihill, A. Schubert, X. Sun, B. D. Dunietz, and E. Geva, “A modified approach for simulating electronically nonadiabatic dynamics via the generalized quantum master equation,” J. Chem. Phys. **150**, 034101 (2019).

[33] G. Cohen and E. Rabani, “Memory effects in nonequilibrium quantum impurity models,” Phys. Rev. B **84**, 075150 (2011).

[34] S. Chaturvedi and F. Shibata, “Time-convolutionless projection operator formalism for elimination of fast variables. Applications to Brownian motion,” Zeitschrift für Physik B Condensed Matter **75**, 297–308 (1979).

[35] F. Shibata, Y. Takahashi, and N. Hashistume, “A generalized stochastic Liouville equation. Non-Markovian versus memoryless master equations,” J. Stat. Phys. **75**, 171–187 (1977).

[36] F. Shibata and T. Arimitsu, “Expansion formulas in nonequilibrium statistical mechanics,” J. Phys. Soc. Jpn. **49**, 891–897 (1980).

[37] C. Uchiyama and F. Shibata, “Unified projection operator formalism in nonequilibrium statistical mechanics,” Phys. Rev. E **60**, 2636 (1999).

[38] A. Royer, “Combining projection superoperators and cumulant expansions in open quantum dynamics with initial correlations and fluctuating Hamiltonians and environments,” Phys. Lett. A **315**, 335–351 (2003).

[39] H. P. Breuer, B. Kappler, and F. Petruccione, “The time-convolutionless projection operator technique in the quantum theory of dissipation and decoherence,” Ann. Phys. **291**, 36–70 (2001).

[40] H. P. Breuer, “Genuine quantum trajectories for non-Markovian processes,” Phys. Rev. A **70**, 012106 (2004).

[41] J. Cerrillo and J. Cao, “Non-Markovian dynamical maps: numerical processing of open quantum trajectories,” Phys. Rev. Lett. **112**, 110401 (2014).

[42] R. Rosenbach, J. Cerrillo, S. F. Huelga, J. Cao, and M. B. Plenio, “Efficient simulation of non-Markovian system-environment interaction,” New J. Phys. **18**, 023035 (2016).

[43] R. P. Feynman, “Space-time approach to non-relativistic quantum mechanics,” Rev. Mod. Phys. **20**, 367–387 (1948).

[44] R. P. Feynman and F. L. Vernon, “The theory of a general quantum system interacting with a linear dissipative system,” Annals Phys. **24**, 118–173 (1963).

[45] F. L. Vernon, *The Theory of a General Quantum System Interacting with a Linear Dissipative System*, Ph.D. thesis, California Institute of Technology (1959).

[46] N. Makri and D. E. Makarov, “Tensor propagator for iterative quantum time evolution of reduced density matrices. I. Theory,” J. Chem. Phys **102**, 2600 (1995).

[47] A. Ishizaki and Y. Tanimura, “Quantum dynamics of system strongly coupled to low-temperature colored noise bath: Reduced hierarchy equations approach,” J. Phys. Soc. Jpn. **74**, 3131–3134 (2005).

[48] Y. Tanimura, “Stochastic Liouville, Langevin, Fokker-Plank, and master equation approaches to quantum dissipative systems,” J. Phys. Soc. Jpn. **75**, 082001 (2006).

[49] Y. Tanimura, “Reduced hierarchical equations of motion in real and imaginary time: Correlated initial states and thermodynamic quantities,” J. Chem. Phys. **141**, 04414 (2014).

[50] Y. Tanimura, “Numerically "exact" approach to open quantum dynamics: The hierarchical equations of motion (HEOM),” J. Chem. Phys. **153**, 020901 (2020).

[51] M. C. Bañuls, M. B. Hastings, F. Verstraete, and J. I. Cirac, “Matrix product states for dynamical simulation of infinite chains,” Phys. Rev. Lett. **102**, 240603 (2009).

[52] M. C. Bañuls, J. I. Cirac, and M. B. Hastings, “Strong and weak thermalization of infinite nonintegrable quantum systems,” Phys. Rev. Lett. **106**, 050405 (2011).

[53] A. Müller-Hermes, J. I. Cirac, and M. C. Bañuls, “Tensor network techniques for the computation of dynamical observables in one-dimensional quantum spin systems,” New J. Phys. **14**, 075003 (2012).

[54] N. Makri, “Iterative evaluation of the path integral for a system coupled to an anharmonic bath,” J. Chem. Phys. **111**, 6164 (1999).

[55] N. Makri, “Blip decomposition of the path integral: Exponential acceleration of real-time calculations on quantum dissipative systems,” J. Chem. Phys. **141**, 134117 (2014).

[56] N. Makri, “Small matrix path integral for system-bath dynamics,” J. Chem. Theory Comput. **16**, 4038–4049 (2020).

[57] A. Strathearn, B. W. Lovett, and P. Kirton, “Efficient real-time path integrals for non-Markovian spin-boson models,” New J. Phys. **19**, 093009 (2017).

[58] S. Weiss, J. Eckel, M. Thorwart, and R. Egger, “Iterative real-time path integral approach to non-equilibrium quantum transport,” Phys. Rev. B **77**, 195316 (2008).

[59] D. Segal, A. J. Millis, and D. R. Reichman, "Numerically exact path-integral simulation of nonequilibrium quantum transport and dissipation," Phys. Rev. B **82**, 205323 (2010).

[60] L. Kidon, H. Wang, M. Thoss, and E. Rabani, "On the memory kernel and the reduced system propagator," J. Chem. Phys. **149**, 104105 (2018).

[61] S. Chatterjee and N. Makri, "Real-time path integral methods, quantum master equations, and classical vs quantum memory," J. Phys. Chem. B **123**, 10470–10482 (2019).

[62] M. B. Hastings, "An area law for one-dimensional quantum systems," J. Stat. Mech: Theory and Experiment , P08024 (2007).

[63] A. Lerose, M. Sonner, and D. A. Abanin, "Influence matrix approach to many-body Floquet dynamics," arXiv preprint cond-mat.str-el/2009.10105 (2020).

[64] M. R. Jorgensen and F. A. Pollock, "Exploiting the causal tensor network structure of quantum processes to efficiently simulate non-Markovian path integrals," Phys. Rev. Lett. **123**, 240602 (2019).

[65] I. A. Luchnikov, S. V. Vintskevich, H. Ouerdane, and S. N. Filippov, "Simulation complexity of open quantum dynamics: Connections with tensor networks," Phys. Rev. Lett. **122**, 160401 (2019).

[66] M. Cygorek, M. Cosacchi, A. Vagov, V. M. Axt, B. W. Lovett, J. Keeling, and E. M. Gauger, "Numerically-exact simulations of arbitrary open quantum systems using automated compression of environments," arXiv preprint quant-ph/2101.01653 (2021).

[67] F. A. Pollock, C. Rodriguez-Rosario, T. Frauenheim, M. Paternostro, and K. Modi, "Non-Markovian processes: Complete framework and efficient characterization," Phys. Rev. A **97**, 012127 (2018).

[68] I. A. Luchnikov, S. V. Vintskevich, D. A. Grigoriev, and S. N. Filippov, "Machine learning non-Markovian dynamics," Phys. Rev. Lett. **124**, 140502 (2020).

[69] N. Makri, "Modular path integral methodology or real-time quantum dynamics," J. Chem. Phys. **149**, 214108 (2018).

[70] S. Kundu and N. Makri, "Modular path integral for discrete systems with non-diagonal couplings," J. Chem. Phys. **151**, 074110 (2019).

[71] S. Kundu and N. Makri, "Exciton-vibration dynamics in J-aggregates of a perylene bisimide from real-time path integral calculations," J. Phys. Chem. C **125**, 201–210 (2021).

[72] N. Makri, "Modular path integral: Quantum dynamics via sequential necklace linking," J. Chem. Phys. **148**, 101101 (2018).

[73] S. Kundu and N. Makri, "Efficient matrix factorisation of the modular path integral for extended systems," Molecular Physics (2020).

[74] J. J. García-Ripoll, "Time evolution of matrix product states," New J. Phys. **8**, 305 (2006).

[75] U. Schollwöck, "The density-matrix renormalization group in the age of matrix product states," Ann. Phys. **326**, 96–192 (2011).

[76] C. D. White, M. Zalatel, R. S. K. Mong, and G. Refael, "Quantum dynamics of thermalizing systems," Phys. Rev. B **97**, 035127 (2018).

[77] V. Murg, F. Verstraete, and J. I. Cirac, "Variational study of hard-core bosons in a two-dimensional optical lattice using projected entangled pair states," Phys. Rev. A **75**, 033605 (2007).

[78] J. Gray, "quimb: A python library for quantum information and many-body calculations," Journal of Open Source Software **3**, 819 (2018).

[79] M. Zwolak and G. Vidal, "Mixed-state dynamics in one-dimensional quantum lattice systems: A time-dependent superoperator renormalization algorithm," Phys. Rev. Lett. **93**, 207205 (2004).

[80] F. Verstraete, J. J. Garcia-Ripoll, and J. I. Cirac, "Matrix product density operators: Simulation of finite-temperature and dissipative systems," Phys. Rev. Lett. **93**, 207204 (2004).

[81] T. Barthel, U. Schollwöck, and S. R. White, "Spectral functions in one-dimensional quantum systems at finite temperature using the density matrix renormalization group," Phys. Rev. B **79**, 245101 (2009).

[82] C. Karrasch, J. H. Bardarson, and J. E. Moore, "Finite-temperature dynamical density matrix renormalization group and the drude weight of spin-1/2 chains," Phys. Rev. Lett. **108**, 227206 (2012).

[83] A. Strathearn, P. Kirton, D. Kilda, J. Keeling, and B. W. Lovett, "Efficient non-Markovian quantum dynamics using time-evolving matrix product operators," Nature Communications **9**, 3322 (2018).

[84] H. Wang and M. Thoss, "From coherent motion to localization: Dynamics of the spin-boson model at zero temperature," New J. Phys. **10**, 115005 (2008).

[85] N. Makri, "Small matrix disentanglement of the path integral: Overcoming the exponential tensor scaling with memory length," J. Chem. Phys. **152**, 041104 (2020).

[86] S. Trotzky, Y.-A. Chen, A. Flesch, I. P. McCulloch, U. Schollwock, J. Eisert, and I. Bloch, "Probing the relaxation towards equilibrium in an isolated strongly correlated one-dimensional bose gas," Nature Phys. **8**, 325–330 (2012).

Appendix A

INTRODUCTION TO TENSOR NETWORKS

Motivation for Using Tensor Networks

The phrase "quantum supremacy" is often thrown around to describe the ambiguous point at which quantum computers outperform classical computers. Depending on the algorithm and its potential quantum speed up, "quantum supremacy" can provide targets for decoherence and dephasing lifetimes, as well as quantum computer size. However, there are always some caveats when making this comparison. As evidenced in the Google-IBM spat, depending on the classical algorithm used, there can be significant reduction in computational cost, making a problem that seemed to take tens of thousands of years can instead take a matter of a few days or even minutes [1–3]. Note that this does not mean the hardware developments presented by the Google team are not important or not interesting–in the end, if the quantum algorithm truly provides exponential speed-up, eventually the quantum computer will exhibit quantum supremacy.

In addition to intelligently identifying the correct classical algorithm, if the problem tolerates some degree of error, one should also consider potential speed-ups obtained from allowing for approximations. It should not be unreasonable to allow the classical algorithm to only be accurate within some small error. After all, quantum computers are inherently probabilistic—obtaining expectation values of observables requires measuring the quantum system many times. (Also, since taking the measurement collapses the quantum state, the quantum state must be prepared again that many times.) This in and of itself produces a statistical error on the final value, though the variance can be reduced by taking more samples.

Some examples of such approximate classical algorithms include 'quantum-inspired classical algorithms' for common linear algebra problems [4, 5]. Another notable example (used in Chapter 4 of this work) are Matrix Product States (and tensor networks), which are an extremely popular framework in the physics community for performing simulations of 1-D (and arbitrary geometry) quantum systems. These algorithms capitalize on the low-rank nature of the problem, and revolve around compressing the information contained in high dimensional tensors. In this section, we will introduce basic concepts of tensor networks.

A.1 High-dimensional Tensors

Review of linear algebra

A d-dimensional vector space is one that is spanned by d orthonormal basis vectors. The standard basis vectors $\{e_1, e_2, ...e_d\}$ are vectors where only the $(i-1)^{\text{th}}$ element is 1 and the rest are 0's. Therefore, any real/complex vector of length d exists in this d-dimensional real/complex vector space.

A Hilbert space is a vector space with an appropriate definition of an inner product that allows for the measurement of distance and angles of vectors. (In technical speak, this means the space is a complete metric space in which every Cauchy sequence is convergent.) For example, Euclidean space is a 3-dimensional Hilbert space. A d-dimensional generalization of Euclidean space is the ℓ^2-space for which the inner product is defined as the dot product

$$\langle \mathbf{x}, \mathbf{y} \rangle = \sum_{i=1}^{d} x_i^* y_i \ .$$

In this field, a tensor is simply defined as a multi-dimensional array. For example, a scalar, vector, and matrix are 0, 1, and 2-dimensional tensors, respectively. If each axis of the tensor is of size d, then an n-dimensional tensor occupies d^n-dimensional space. The inner product between tensors A and B can be generalized from the vector inner product definition,

$$\langle A, B \rangle = \sum_{i_1=1}^{d_1} \cdots \sum_{i_n}^{d_n} a^*_{i_1,\ldots,i_n} b_{i_1,\ldots,i_n}$$

where each i_α indexes elements along the α-th axis of the tensor, and d_α is the dimension of that axis. This definition is equivalent to first vectorizing the tensors (ie. reshaping them into a 1-D array) and then taking the vector inner product.

Given this definition of the inner product, the norm of an arbitrary n-dimensional tensor A is given by the Frobenius norm,

$$||A||^2 = \sum_{i_1=1}^{d_1} \cdots \sum_{i_n}^{d_n} |a_{i_1,\ldots,i_n}|^2 \ .$$

Diagrammatic notation

We represent n-dimensional tensors using shapes with n 'legs' sticking out of it, with each leg representing one axis of the tensor. The size of each leg, also called the **bond dimension**, is the size of the tensor along the corresponding axis. For clarity, we will refer to the dimension of the tensor by the number of its legs. Also, sometimes, for shorthand, the shapes are omitted.


(a) scalar

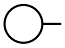
(b) vector

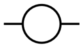
(c) matrix

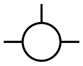
(d) 3-D tensor

Connecting two legs together denotes contractions of the tensors. For example, shown below are diagrams representing traditional matrix-vector and matrix-matrix multiplications, which return vectors and matrices, respectively. We can also show the trace operation, which is a single tensor operation that returns a scalar.

$$b_i = \sum_j A_{ij} x_j$$

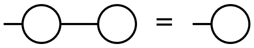
(a) matrix-vector mult.

$$b_{ik} = \sum_j A_{ij} B_{jk}$$

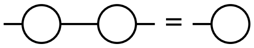
(b) matrix-matrix mult.

$$c = \sum_i A_{ij} \delta_{ij}$$

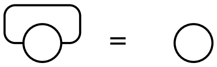
(c) trace operation

It is easy to generalize to contraction between higher dimensional tensors. For example, contraction between two 3-legged tensors along the first and third legs looks like

$$T_{abjk} = \sum_i A_{abi} B_{ijk}$$

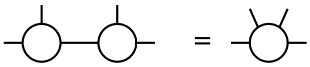

The inner product between two tensors is simply the contraction of all of their legs.

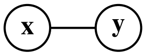

(a) vector inner product

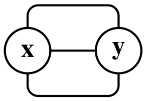

(b) tensor inner product

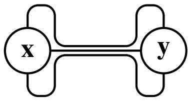

(c) vectorized tensor inner product

In the diagram (c), we group together the three legs of the tensor together into a single leg. This represents vectorizing the tensors into a vector whose size is the product of all of the dimensions of the original legs.

Tensor decomposition

First, let us consider the decomposition of a vector that lives in a $(d_1 d_2)$-dimensional Hilbert space H, with the corresponding standard basis vectors $E = \{e_1, ..., e_{d_1 d_2}\}$.

Then, let $\mathbb{H}_1$ be a Hilbert space of dimension d_1 with standard basis vectors $\{\mathbf{e}_1^{(1)}, ..., \mathbf{e}_{d_1}^{(1)}\}$. Similarly define a d_2-dimensional Hilbert space $\mathbb{H}_2$. We claim that $\mathbb{H}$ is isomorphic to the outer product of $\mathbb{H}_1$ and $\mathbb{H}_2$, which has standard basis vectors

$$E' = \{\mathbf{e}_i^{(1)} \otimes \mathbf{e}_j^{(2)}\} \quad \text{where} \quad i \in [1, d_1],\ j \in [1, d_2]\ .$$

Because this set contains $d_1 d_2$ orthonormal vectors, we can perform a one-to-one mapping from E to E'. Thus, $\mathbb{H} \cong \mathbb{H}_1 \otimes \mathbb{H}_2$.

Using the decomposed standard basis vectors, we can express the original array as a 2-D object,

$$T = \sum_{i=1}^{d_1 d_2} b_i\, \mathbf{e}_i \cong \sum_{i=1}^{d_1} \sum_{j=1}^{d_2} c_{ij}\, \mathbf{e}_i^{(1)} \otimes \mathbf{e}_j^{(2)} \tag{A.1}$$

where b_i, c_{ij} are scalars corresponding to the elements in the tensor. Reshaping a vector into any number of legs follows the same idea, but it is required that the original dimension of the leg be equal to the product of the dimensions of the new legs. This is because the reshaping operation does not change the dimension of Hilbert space that the tensor resides in.

Now, suppose we wish to decompose T into two tensors contracted with each other. We can do so by reshaping T into a 2-D tensor (ie. matrix), and then performing singular value decomposition (SVD).

$$\mathbf{T} = \mathbf{U}\sigma\mathbf{V}^T = \sum_{ij} \sum_{s} \sigma_s \left(U_{is} \left|e_i\right\rangle\right) \otimes \left(V_{js} \left|e_j\right\rangle\right)$$

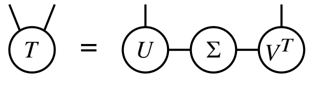

For higher dimensional tensors, depending on the desired connectivity of the decomposed tensors, there is no generally optimal decomposition algorithm.

The work in our thesis will utilize two tensor decompositions. The first is the decomposition of a 4-legged tensor, which will be explained more carefully in Chapter 3. In short, a nested decomposition is performed, such that the original 4-legged tensor is first split into two tensors with 2 dangling legs each, which are then decomposed further.

The second is the decomposition of an n-legged tensor into a 1D chain of n tensors. This is called a tensor train (TT) in computer science, or a Matrix Product State (MPS) in physics if the tensor represents a quantum state. The TT/MPS can be obtained from the original tensor using the Schmidt decomposition algorithm, which calls for performing SVD iteratively. This is shown below diagrammatically for a 3-legged tensor.

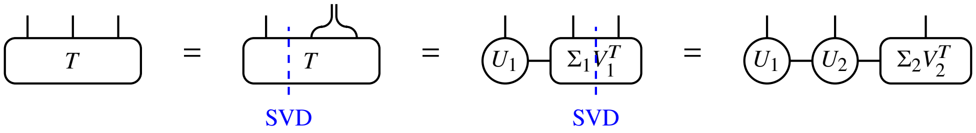

In the first step, the last two legs are grouped together to look like a single index. In the second step, SVD is performed at the blue line to separate T into two tensors by introducing a leg that will be contracted over. In the third step, SVD is performed on the new 3-legged block at the blue line, introducing another contracted leg. With that, we have decomposed the original 3-legged tensor into a chain of 3 tensors.

Other decomposition methods include CP and Tucker decomposition, which rely on alternating least squares (ALS) to minimize the error of the decomposition with respect to the original tensor. However we will not be talking about or using these methods.

A.2 Many-body Quantum States

In quantum physics, the state of a single d-dimensional particle, such as a particle with d energy levels, can be represented as a vector in a d-dimensional Hilbert space $\mathbb{H}$. One choice of basis vectors is $\{|e_j\rangle : j \in [1, d]\}$ where each vector represents the occupation of the j^{th} energy level. Then, in physics bra-ket notation, an arbitrary state can be written as

$$|\psi\rangle = \sum_{j=1}^{d} c_j |e_j\rangle$$

where c_j are scalar coefficients.

If we consider a system that contains two of these particles, the system now resides in the d^2-dimensional Hilbert space $\mathbb{H}^{\otimes 2}$. An arbitrary state is some superposition of all possible combinations of two particle states, and can be written as

$$|\psi\rangle = \sum_{i,j=1}^{d} c_{ij} |e_i\rangle \otimes |e_j\rangle$$

where c_{ij} again are scalar coefficients. Comparing it to Eq. A.1, it is clear that one can represent many-body quantum states using high-dimensional tensors.

Entangled states

Quantum entanglement is a property of many-body quantum states in which the state of one particle depends on the state of the others. The classic examples are

Bell states, which are maximally entangled states of two qubits (A and B). One of the four states is

$$\Phi^+ = \frac{1}{\sqrt{2}} \left(|0\rangle_A \otimes |0\rangle_B \; + \; |1\rangle_A \otimes |1\rangle_B \right) \; .$$

If one measures qubit B, then depending on the outcome (0 or 1), the state of A is also known–the states of the qubits are perfectly correlated with each other.

Entanglement entropy is a measure of quantum entanglement between two parts A and B of a quantum state. Consider a pure state $\rho_{AB} = |\Phi\rangle_{AB} \langle\Phi|_{AB}$, where

$$|\Phi\rangle_{AB} = \sum_i \sigma_i \, |a_i\rangle \otimes |b_i\rangle \; =$$ 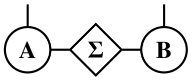 .

In the mathematical expression, $\{|a_i\rangle\}$ and $\{|b_i\rangle\}$ are orthonormal vectors spanning the Hilbert spaces of particles A and B, respectively. In the diagram, tensors **A** and **B** contain the vectors $\{|a_i\rangle\}$ and $\{|b_i\rangle\}$ along its columns and rows, respectively, and matrix $\boldsymbol{\Sigma}$ contains the $\{\sigma_i\}$ along its diagonal. (We use the diamond to denote that it is a diagonal matrix.) If the state is normalized, then $\mathrm{Tr}(\rho) = \sum_i |\sigma_i|^2 = 1$.

The reduced density matrices of particles A and B are

$$\rho_A = \mathrm{Tr}_B(\rho_{AB})$$

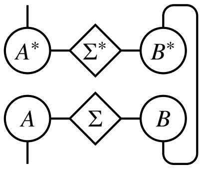

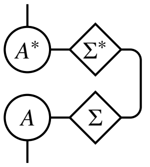

$$\rho_B = \mathrm{Tr}_A(\rho_{AB})$$

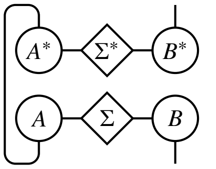

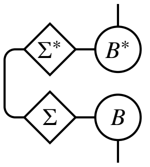

The von Neumann entanglement entropy is given by

$$S(\rho_{A/B}) = -\mathrm{Tr}(\rho_{A/B} \log \rho_{A/B}) = -\sum_i |\sigma_i|^2 \log(|\sigma_i|^2) \; . \qquad \text{(A.2)}$$

In the case of the Bell state Φ^+, the entanglement entropy $S = 2(\frac{1}{2}\log 2) = 0.693$, which is the maximum for the 2-qubit system.

In contrast, let us consider the state $|\Psi_x\rangle$, which can be represented using matrix M

$$|\Psi_x\rangle = \frac{1}{2} \left(|00\rangle + |01\rangle + |10\rangle + |11\rangle \right) \quad \Rightarrow \quad M = \frac{1}{2} \begin{array}{cc} \begin{array}{cc} |0\rangle_A & |1\rangle_A \end{array} & \\ \begin{bmatrix} 1 & 1 \\ 1 & 1 \end{bmatrix} & \begin{array}{c} |0\rangle_B \\ |1\rangle_B \end{array} \end{array}$$

where the indices of the rows/columns of M correspond to the states of qubit A/B. Decomposing this tensor via SVD, we get

$$M = \overbrace{\begin{bmatrix} \frac{1}{\sqrt{2}} \\ \frac{1}{\sqrt{2}} \end{bmatrix}}^{A} \begin{bmatrix} 1 \end{bmatrix} \overbrace{\begin{bmatrix} \frac{1}{\sqrt{2}} & \frac{1}{\sqrt{2}} \end{bmatrix}}^{B}$$

where the first and last matrices correspond to the states of particle A and B, respectively. The matrix is only of rank one, which means that $|\Psi_x\rangle$ actually is just a product of one-qubit states of A and B,

$$|\Psi_x\rangle = \frac{1}{2} \overbrace{(|0\rangle + |1\rangle)}^{A} \otimes \overbrace{(|0\rangle + |1\rangle)}^{B} \ .$$

The entanglement entropy for product states is 0, which means that it actually is a classical state.

A brief side note: entangled states are different from mixed states. Mixed states are summations of pure states, $\rho_{AB} = \sum_i \alpha_i |\psi_i\rangle_{AB} \langle\psi_i|_{AB}$, assuming proper normalization. Unrelated to that is the correlations between parts A and B of the system, which is what entanglement refers to. The pure states $|\psi_i\rangle_{AB}$ that build up the mixed state may exhibit entanglement themselves. From a linear algebra perspective, one can understand the difference between the two as performing decompositions along different axes of the tensor.

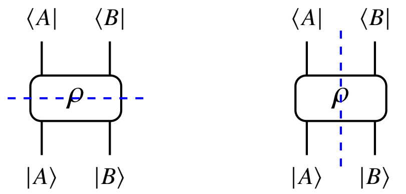

(a) state purity (b) entanglement

A.3 Tensor Networks

Tensor networks (TNs) are simply networks of multiple tensors that are contracted with each other in some fashion. Common TN geometries used for representing quantum states include a 1-D chain (Matrix Product States (MPS)), a 2-D lattice (Projected Entangled Pair States (PEPS)), and a renormalizing network (Multiscale Entanglement Renormalization Ansatz (MERA)). Most of the work in this thesis is focused on 1D systems which we represent with MPS.

TNs can be used to represent quantum states, as well as the operations acting on the states, such as time evolution or measuring the expected value of an operator.

Below is a non-traditional introduction to TNs (specifically MPS). For beginners, looking at Ref. [6] is recommended.

Matrix product states (MPSs)

At this point, we have presented a mathematical framework for representing quantum states. However, on its own, it does not provide any computational advantages for working with many-body systems.

Consider a system consisting of n d-dimensional particles. This system spans a Hilbert space of dimension d^n, and the state can be represented using an n-legged tensor where each leg has a dimension of d. It is clear that the memory associated with representing the state of the system scales exponentially with system size n. Operators acting on the full system, such as the Hamiltonian, would look like a $d^n \times d^n$ operator. The Hamiltonian defines the system properties–its eigenvectors form the set of orthonormal basis vectors corresponding to a particular energy (the eigenvalues). Computing the dynamics of a state requires exponentiation of the Hamiltonian, which is equivalent to performing an eigenvalue decomposition. The computational cost of performing eigenvalue decomposition of an $m \times m$ matrix is naively $O(m^3)$ (though there are speed ups using recursive algorithms, resulting in computational costs of $O(m^{2.67})$ [7]) Therefore, the computational cost of performing an eigenvalue decomposition on the Hamiltonian is of $O(d^{3n})$. In other words, the cost of the algorithm scales exponentially with respect to system size (a result that holds true regardless if the more advanced algorithm is used.)

Previously, we discussed decomposing these larger tensors into a network of smaller tensors. Here we will specifically consider representing the quantum state as a 1D chain of n 3-legged tensors, a Matrix Product State (MPS). At first glance, it might not be obvious what the dimension of the legs connecting the tensors (virtual bonds) are. However, if we explicitly perform Schmidt decomposition on the original n-legged tensor to obtain the MPS, we find that the maximum virtual bond dimension is $d^{n/2}$.

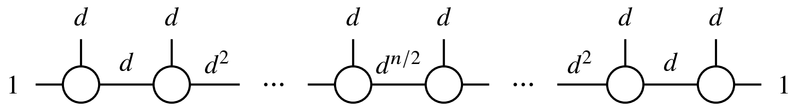

Thus, as one might have expected, representing the multi-legged tensor as an MPS does not remove the exponential scaling in memory and computational cost. It only hides it in the dimensions of the virtual legs.

However, the key advantage of the MPS ansatz is that one can artificially limit the virtual bond dimension to some finite value D, thus making it tractable to work with. The result is a low-rank approximation of the original tensor. This ansatz is systematically improvable—by increasing D, one will obtain a better approximation of the true network. In the next section, we discuss how to obtain the optimal low rank approximation for 1D systems.

Compression of MPS

Given matrix $A = \mathbf{U\Sigma V}^T$, we would like to find a rank D approximation such that $||A - A_{(D)}||^2$ is minimal. According to the Eckart-Young-Mirski theorem [8], the optimal solution is

$$A_{(D)} = \sum_{i=1}^{D} \sigma_i \left|u_i\right\rangle \left\langle v_i\right| \quad = \tag{A.3}$$

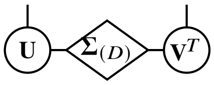

where the singular values σ_i are ordered in decreasing magnitude such that only the largest D values are included in the sum. These singular values are contained in the diagonal matrix $\mathbf{\Sigma}_{(D)}$. The vectors $\left|u_i\right\rangle$ and $\left\langle v_i\right|$ are the columns/rows of U and V^T corresponding to the i^{th} singular value.

However, when finding a low-rank approximation for a single tensor in a network, one has to account for the other tensors (the environment). Otherwise, it may lead to a non-optimal approximation of the full TN. How to best account for the environment for arbitrary geometries is unclear. However, for MPS, it is straightforward to 'canonicalize' the MPS such that the environment tensors look like the identity, allowing one to approximate the tensor in question in isolation.

In TNs, because the tensors are connected to each other, the definition of each tensor can vary while the state as a whole stays the same. This is referred to as the gauge degree of freedom. A simple example is simply multiplying and dividing two tensors in the TN with the same scalar.

For MPS, we define the left and right canonical forms as the choice in gauge such that

$$\sum_{ld} L^*_{ldr} L_{ldr'} = I_{rr'} \qquad\qquad \sum_{dr} R^*_{ldr} R_{l'dr} = I_{ll'}$$

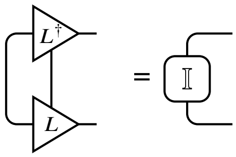

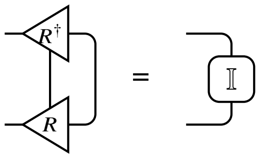

Note that we use triangles instead of circles to explicitly denote the canonicalization.

Now consider an MPS of the form

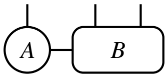

We wish to replace B with a low-rank approximation B'. To do so, we must minimize

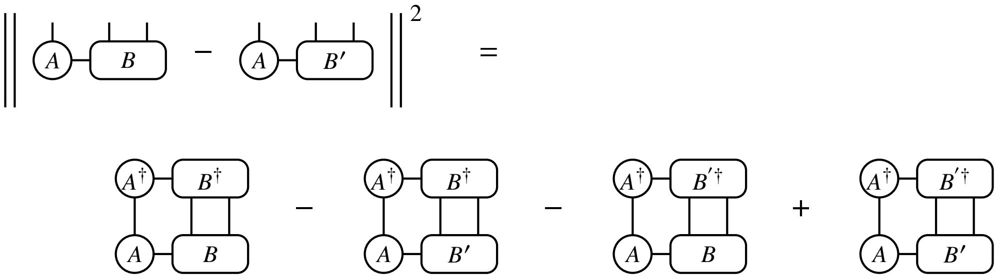

When computing the overlaps, we can insert a gauge XX^{-1} such that AX is left canonical. Then

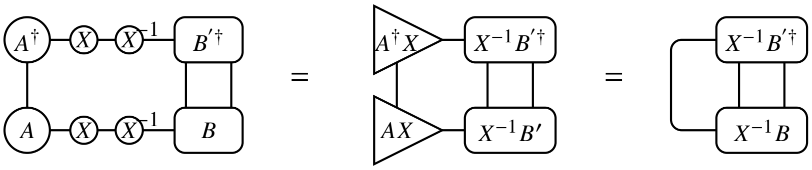

and likewise for all other terms in the sum. With this choice in gauge, optimizing the MPS becomes equivalent to finding the D-rank approximation to $\tilde{B} = X^{-1}B$, which is simply $\tilde{B}_{(D)}$, as defined above in Eq. A.3. The computational cost is the cost of performing SVD on just $\tilde{B}$ instead of the full MPS. Note that if no compression of rank is performed (ie. $B' = B$), then the MPS gauge does not actually matter.

Instead of trying to find the gauge X explicitly, typically one uses SVD or QR decomposition to put the MPS in canonical form, since the reshaped unitaries obey the conditions for left or right canonicalization.

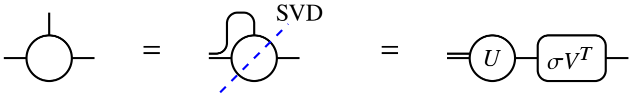

where

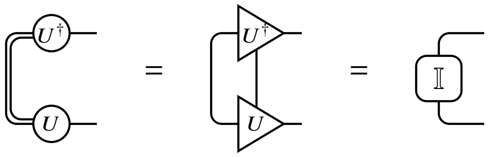

By definition, the full unitary U obeys $U^{\dagger}U = UU^{\dagger} = \mathbb{I}$. However, the reduced unitary U' obtained after removing the columns associated with the discarded singular values only satisfies $U'^{\dagger}U' = \mathbb{I}$, while $U'U'^{\dagger} \neq \mathbb{I}$ (which makes it an isometry). In any case, both U and U' are left canonical. Similar logic can be applied to find that V^T and its reduced form are both right canonical.

The algorithm for compressing an MPS is as follows. First one must ensure that the MPS is in the proper canonical form. To **left/right canonicalize** a finite length MPS, one starts at the left/right end and then performs QR or SVD to put each tensor in left/right canonical form. If the MPS is normalized, then it is possible to gauge the MPS such that all tensors are left/right canonical. Once the MPS is fully left/right canonical, then one can **compress** the MPS using SVD starting from the right/left end and sweeping left/right. After compression, the MPS is now in right/left canonical form. Typically, canonicalization and compression are the most expensive operations in MPS algorithms, since the computational cost of the SVD operation scales like $O(D^3)$.

Matrix product operators (MPOs)

In order to use MPS for quantum systems, we also need to be able to represent the Hamiltonian H in matrix product form. Constructing the matrix product operator (MPO) for H is typically done by hand, and varies depending on the Hamiltonian's structure. In general, the MPO can be written out as a chain of 4-legged tensors,

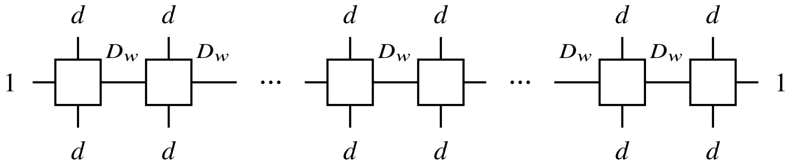

where the lower legs correspond to the 'input' and the upper legs correspond to the 'output' of the full operator H. The virtual bond dimension D_w is determined by the structure of the Hamiltonian, and is a constant for Hamiltonians whose structure is translationally invariant. Typically square shapes are used to denote MPOs.

For example, the MPO for the nearest neighbor Hamiltonian $H = \sum_i H_i + O_i O_{i+1}$ is

$$H = \begin{bmatrix} H_1 & O_1 & \mathbb{I} \end{bmatrix} \begin{bmatrix} \mathbb{I} & 0 & 0 \\ O_2 & 0 & 0 \\ H_2 & O_2 & \mathbb{I} \end{bmatrix} \begin{bmatrix} \mathbb{I} & 0 & 0 \\ O_3 & 0 & 0 \\ H_3 & O_3 & \mathbb{I} \end{bmatrix} \quad \cdots \quad \begin{bmatrix} \mathbb{I} \\ O_L \\ H_L \end{bmatrix} .$$

Note that the elements in the matrices are operators instead of scalars, thus making each one actually a 4-legged tensor. This MPO has virtual bond dimension $D_w = 3$. Ref. [6] has some examples of MPOs for other Hamiltonians, such as one with exponential long range interactions.

Time evolution

In physics, oftentimes one is interested in knowing how a system state $|\psi\rangle$ evolves in time under some Hamiltonian H as dictated by the time-dependent Schrodinger equation

$$i\frac{\partial}{\partial t}|\psi\rangle = H|\psi\rangle \ . \tag{A.4}$$

The state at time t is thus

$$|\psi(t)\rangle = e^{-iHt}|\psi(0)\rangle \ . \tag{A.5}$$

To perform time evolution, one needs to exponentiate the Hamiltonian. For the above nearest neighbor Hamiltonian, one can separate it into terms acting on even or odd bonds, $H = H_e + H_o$, where

$$\begin{aligned} H_e &= \sum_{i\,\in\,\text{even}} \frac{1}{2}(H_i + H_{i+1}) + O_i O_{i+1} \\ H_o &= \sum_{i\,\in\,\text{odd}} \frac{1}{2}(H_i + H_{i+1}) + O_i O_{i+1} \end{aligned}$$

Because all the terms in H_e and H_o commute,

$$\begin{aligned} \exp(-iH_e t) &= \prod_{i\,\in\,\text{even}} \exp\left(-it\left(\frac{1}{2}(H_i + H_{i+1}) + O_i O_{i+1}\right)\right) \\ \exp(-iH_o t) &= \prod_{i\,\in\,\text{odd}} \exp\left(-it\left(\frac{1}{2}(H_i + H_{i+1}) + O_i O_{i+1}\right)\right) \ . \end{aligned}$$

Note that one has to be careful in the definition of H_e and H_o at the boundaries of the chain, which we did not explicitly shown in the above equations. Then one can approximate the exponential using the first-order Suzuki-Trotter decomposition,

$$\begin{aligned} e^{-iHt} = \left(e^{-iHt/n}\right)^n &= \left(e^{-i(H_e+H_o)t/n}\right)^n \\ &\approx \left(e^{-iH_e t/n} e^{-iH_o t/n}\right)^n + O(t/n) \ . \end{aligned}$$

The tensor network diagram for a single time step, with $\Delta t = t/n$, is

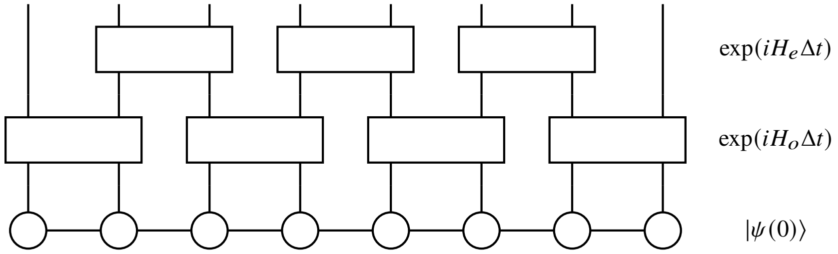

Note that applying an operator to the MPS increases its bond dimension.

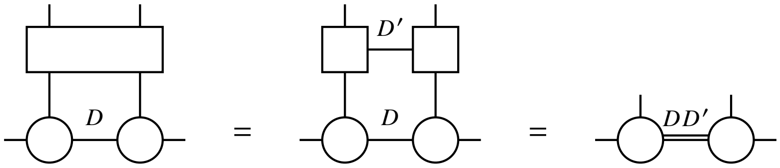

Thus, at each time evolution step, the MPS must be compressed back to the desired bond dimension D.

In the Time Evolution Block Decimation algorithm (TEBD) [9], the tensors of each row are applied to the MPS from one edge to another. After applying one block, the updated part of the MPS is compressed to bond dimension D and is put in the proper left/right canonical form as one sweeps to the right/left. The next row is applied in the same fashion, but in the opposite sweep direction.

If one is unable to decompose the exponential into nearest neighbor blocks as above, then one can expand the exponential using the Taylor series. We use the 4th order expansion,

$$\exp(-iH\Delta t) = \mathbb{I} + (-i\Delta t)H + \frac{(-i\Delta t)^2}{2}H^2 + \frac{(-i\Delta t)^3}{6}H^3 + \frac{(-i\Delta t)^4}{24}H^4 + \mathcal{O}(\Delta t^5)$$

$$\approx \frac{1}{24}\prod_{i=1}^{4}(-iH\Delta t - \alpha_i) \quad \text{where} \quad \begin{aligned} \alpha_1,\, \alpha_2 &= -1.72944 \pm 0.88897i \\ \alpha_3,\, \alpha_3 &= -0.270556 \pm 2.50478i \end{aligned}$$

which is equivalent to using 4th order Runge-Kutta (RK4). For convergence, the norm of the approximate exponential must be less than or equal to one. This means that the time step Δt must satisfy $\lambda_{max} \cdot \Delta t < 2.828$ for real time propagation or $\lambda_{max} \cdot \Delta t < 2.785$ for imaginary time propagation, where λ_{max} is the maximal eigenvalue of H [10].

The tensor network for a single time step is then

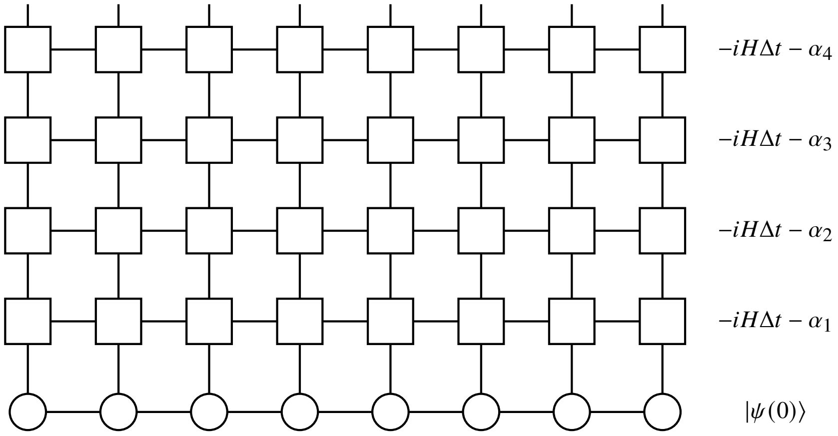

One can use a straightforward method to contract this network to obtain the state at the next time step: first, the bottoms rows are contracted together into a single MPS, which is then canonicalized and compressed. This is repeated for each of the four MPOs. The canonicalization step is the most computationally expensive step, scaling like $\mathcal{O}(d(D_w D)^3)$.

It is possible to develop a scheme similar to TEBD in which the contraction and compression are performed within the same sweep. However, the accuracy of this method has not been studied extensively, so it is not used in this thesis.

In the time-dependent DMRG (TD-DMRG) algorithm, one also performs time evolution using RK4. However, the update algorithm is notably different. We do not cover it here, and instead refer readers to [11–14]. A related algorithm is the time-dependent variational principle (TDVP) algorithm, but a notable difference is that the MPS is confined to the tangent space defined by the Dirac-Frenkel equation to enforce conservation of energy [15, 16].

Another time evolution algorithm is the multi-layer multi-configuration time-dependent Hartree theory (ML-MCTDH) method [17–19]. Though originally developed not in the tensor network framework, it seems to be equivalent to a tree tensor network geometry. It also utilizes the Dirac-Frenkel equation. This method has seen great success for obtaining long-time dynamics for a wide range of problem types. Again, we do not discuss the details here.

Representability of MPS

If we limit the MPS to have finite bond dimension D, the MPS can only accurately capture low rank tensors. Assuming normalization of the state, the maximum entanglement entropy (Eq. A.2) the MPS can have is $S_{max} = \log(D)$. Thus, higher D allows the MPS to represent more highly entangled states.

For local and gapped 1-D Hamiltonians, it has been proven that the entanglement entropy of the ground state obeys **area law** scaling [20]. This means that it scales with the boundary area (which is a constant in 1D systems). It was later shown that if the energy gap is ϵ, then the entanglement entropy scales like $S \sim \mathcal{O}(1/\epsilon)$ [21, 22]. Separately, it has also been proven that the ground states of these Hamiltonians have correlation lengths ξ that scale like $\xi \sim \mathcal{O}(1/\epsilon)$ [23–25]. Combining the two results suggests (but does not prove) that $S \sim \mathcal{O}(\xi)$, which is consistent with the intuition that the entanglement across some boundary should only depend on $\mathcal{O}(\xi)$ sites in the neighborhood of the boundary. However, rigorous proofs have only obtained loose bounds $S \sim \exp(O(\xi))$ [20, 26]. Investigations from an MPS perspective have also had limited success in defining tight bounds on the approximability of the state due to the area law [27].

However, it was also found that the bond dimensions only needs to scale polynomially with number of spins to represent ground states, even for critical systems [28]. This is consistent with the great success of using MPS to find and represent ground states of local Hamiltonians in practice. To find the ground state, one can perform imaginary time evolution from a random initial state, or one can use a local optimization technique equivalent to Density Matrix Renormalization Group (DMRG), modulo differences in implementation [6, 29–34]. In essence, one finds the MPS wavefunction that minimizes the energy of the Hamiltonian by locally optimizing each tensor in a sweeping fashion. Typically MPS had been used to investigate 1-D spin chains, such as the transverse Ising model and the Heisenberg model. However, it has been successfully applied to quantum chemistry electronic structure calculations, performing similarly if not better than other computational chemistry methods [35, 36]. Furthermore, though there are no known bounds on the entanglement entropy of excited states, MPS have also been used successfully to represent low-lying excited states [37–39].

On the other hand, if the state exhibits volume law entanglement, which means that the entanglement entropy scales with the volume of the system (increases linearly for 1D systems), then it cannot be efficiently represented using MPS. It is believed that such states include most excited states, which might be accessed when performing real-time time evolution. As such, real-time dynamics is often cited as the prime example for which quantum computers will show a quantum advantage [27].

With regards to real-time dynamics, systems are typically classified as integrable, thermalizing, or localizing [40]. Integrable systems are very particular in that the trajectory of a state is closed, resulting in periodic dynamics. However, slight perturbations to such systems will yield non-integrable dynamics. The majority of physically relevant systems are non-integrable, which are then coarsely classified as either thermalizing or localizing.

Thermalizing systems are those for which all initial states, even those far from equilibrium, will eventually evolve to a state that appears to be in thermal equilibrium [40–42]. It is believed that thermalization dynamics obeys the volume law. Intuition suggests that thermalization requires the information of one particle to be spread across the entire system, resulting in entanglement that scales with system volume.

Alternatively, one can argue that due to ergodicity, real-time evolution allows one to access the entirety of Hilbert space, including those with volume law entanglement. Recently, it was analytically derived that these thermalized pure quantum states themselves obey the volume law [43]. Furthermore, the authors found that other pure states with enough scrambling, such as excited eigenstates or states after quenches, exhibited similar entanglement behaviors.

There do seem to be a few cases in which computing the dynamics is feasible. For example, in Ref. [44], the space-time correlation functions for a 1-D spin-1 Heisenberg chain were computed using TD-DMRG. The computed dynamics was essentially evolving a single particle excitation in time, and the system was large enough that finite-size effects could be neglected. In Fig. 3 of that paper, the authors plotted the bond dimension required to represent the state (after ignoring singular values less than some small threshold value) as a function of time. The curve quickly increased, became flat once the maximum allowed bond dimension was reached, and then, interestingly, decreased at long times. Additionally, in Ref. [45], the long-time thermalizing dynamics of the transverse-field Ising model at higher temperatures was computed using TDVP. As mentioned earlier, TDVP utilizes the Dirac-Frenkel constraint (conservation of energy), which projects the dynamics onto a manifold within the original Hilbert space. This guarantees the hydrodynamic behavior at long-times. The bond dimension required to ensure the correctness of the transport coefficients is determined by the quantum processes generating the chaos. Both these works suggest that perhaps the dynamical behavior of thermalizing systems at long times can be obtained, if the error at intermediate times is small enough. This observation is also satisfying in that one expects thermalization to yield relatively straightforward dynamics as one approaches the thermal equilibrium.

Localization dynamics is an active area of research [46, 47]. Intuition might lead us to believe that localized states will exhibit area law entanglement due to the finite range of interactions. It appears that there can be localized states that exhibit volume law entanglement, though the entanglement saturation only occurs at times exponentially long in L [48]. The distinction appears to be the type of localization—either non-interacting Anderson-localized particles or many-body localized states.

In summary, MPS of finite bond dimension D cannot generally capture all time-evolved states. However, there are certain systems (that exhibit localization) for which it may be feasible, or systems in which the error is small enough to be ignored.

Further Developments

Over the years, extensions to these algorithms have been made to allow one to consider other systems like infinite chains [49], chains with periodic boundary conditions [50], mixed states [51, 52], continuous states [53], and higher dimensional systems [54, 55].

However, these further developments for higher dimensions and mixed states are fundamentally limited by the virtual bond dimension.

References

[1] F. Arute, J. Martinis, and G. Q. AI, "Quantum supremacy using a programmable superconducting processor," Nature **574**, 505–510 (2019).

[2] E. Pednault, J. A. Gunnels, G. Nannicini, L. Horesh, and R. Wisnieff, "Leveraging secondary storage to simulate deep 54-qubit sycamore circuits," arXiv , 1910.09534v2.

[3] C. Huang, F. Zhang, M. Newman, J. Cai, X. Gao, Z. Tian, J. Wu, H. Xu, H. Yu, B. Yuan, M. Szegedy, Y. Shi, and J. Chen, "Classical simulation of quantum supremacy circuits," arXiv , 2005.06787.

[4] E. Tang, "A quantum-inspired classical algorithm for recommendation systems," in *Proceedings of the 51st Annual ACM SIGACT Symposium on Theory of Computing*, STOC 2019 (Association for Computing Machinery, New York, NY, USA, 2019) pp. 217—-228.

[5] A. Gilyén, Z. Song, and E. Tang, "An improved quantum-inspired algorithm for linear regression," arXiv , 2009.07268 (2020).

[6] U. Schollwöck, "The density-matrix renormalization group in the age of matrix product states," Ann. Phys. **326**, 96–192 (2011).

[7] J. Demmel, I. Dumitriu, and O. Holtz, "Fast linear algebra is stable," Numerische Mathematik **108**, 59–91 (2007).

[8] C. Eckart and G. Young, "The approximation of one matrix by another of lower rank," Psychometrika **1**, 211–218 (1936).

[9] G. Vidal, "Efficient simulation of one-dimensional quantum many-body systems," Phys. Rev. Lett. **03**, 040502 (2004).

[10] J. Ren, Z. Shuai, and G. K.-L. Chan, "Supplementary information of time-dependent density matrix renormalization group algorithms for nearly exact absorption and flourescene spectra of molecular aggregates at both zero and finite temperature," J. Chem. Theory Comput. **14**, 5027 – 5039 (2018).

[11] S. White and A. E. Feiguin, “Real-time evolution using the density matrix renormalization group,” Phys. Rev. Lett. **93**, 076401 (2004).

[12] U. Schollwöck and S. R. White, “Methods for Time Dependence in DMRG,” AIP Conference Proc. **816**, 155 (2006).

[13] E. Ronca, Z. Li, C. Jimenez-Hoyos, and G. K.-L. Chan, “Time-step targeting time-dependent and dynamical density matrix renormalization group algorithms with ab initio Hamiltonians,” J. Chem. Theory Comput. **13**, 5560–5571 (2017).

[14] J. J. García-Ripoll, “Time evolution of matrix product states,” New J. Phys. **8**, 305 (2006).

[15] J. Haegeman, J. I. Cirac, T. J. Osborne, I. Pižorn, H. Verschelde, and F. Verstraete, “Time-dependent variational principle for quantum lattices,” Phys. Rev. Lett. **107**, 070601 (2011).

[16] J. Haegeman, C. Lubich, I. Oseledets, B. Vandereycken, and F. Verstraete, “Unifying time evolution and optimization with matrix product states,” Phys. Rev. B **94**, 165116 (2016).

[17] H. Wang and M. Thoss, “Multilayer formulation of the multiconfiguration time-dependent Hartree theory,” J. Chem. Phys. **119**, 1289 (2003).

[18] H. Wang and M. Thoss, “From coherent motion to localization: Dynamics of the spin-boson model at zero temperature,” New J. Phys. **10**, 115005 (2008).

[19] H. Wang, “Multilayer multiconfiguration time-dependent Hartree theory,” J. Chem. Phys. A **119**, 7951–7965 (2015).

[20] M. B. Hastings, “An area law for one-dimensional quantum systems,” J. Stat. Mech. , P08024 (2007).

[21] I. Arad, A. Kitaev, Z. Landau, and U. Vazirani, “An area law and subexponential algorithm for 1D systems,” arXiv , 1301.1162 (2013).

[22] Y. Huang, “Area law in one dimension: Degenerate ground states and Renyi entanglement entropy,” arXiv , 1403.0327 (2014).

[23] M. B. Hastings, “Lieb-Schultz-Mattis in higher dimensions,” Phys. Rev. B **69**, 104431 (2004).

[24] M. B. Hastings and T. Koma, “Spectral gap and exponential decay of correlations,” Comm. Math. Phys. **265**, 781–804 (2006).

[25] B. Nachtergale and R. Sims, “Lieb-Robinson bounds on the exponential clustering theorem,” Comm. Math. Phys. **265**, 119–130 (2006).

[26] F. G. S. L. Brandao and M. Horodecki, "An area law for entanglement from exponential decay of correlations," Nature Phys. **9**, 721–726 (2013).

[27] N. Schuch, M. M. Wolf, F. Verstraete, and J. I. Cirac, "Entropy scaling and simulability by matrix product states," Phys. Rev. Lett. **100**, 030504 (2008).

[28] F. Verstraete and J. I. Cirac, "Matrix product states represent ground states faithfully," Phys. Rev. B **73**, 094423 (2006).

[29] S. R. White, "Density matrix formulation for quantum renormalization groups," Phys. Rev. Lett. **69**, 2863 (1992).

[30] S. R. White, "Density matrix algorithms for quantum renormalization groups," Phys. Rev. B **48**, 10345 (1993).

[31] S. Östlund and S. Rommer, "Thermodynamic limit of density matrix renormalization," Phys. Rev. Lett. **75**, 3537 (1995).

[32] J. Dukelsky, M. A. Martín-Delgado, T. Nishino, and G. Sierra, "Equivalence of the variational matrix product state method and the density matrix renormalization group applied to spin chains," Europhys. Lett. **43**, 457–462 (1998).

[33] S. R. White, "Density matrix renormalization group algorithms with a single center site," Phys. Rev. B **72**, 180403(R) (2005).

[34] T. Hiroshi, T. Hikihara, and T. Nishino, "Fixed point of finite system dmrg," J. Phys. Soc. Jpn. **68**, 1537–1540 (1999).

[35] G. K.-L. Chan and M. Head-Gordon, "Highly correlated calculations with polynomial cost algorithm: A study of the density matrix renormalization group," J. Chem. Phys. **116**, 4462 (2002).

[36] G. K.-L. Chan and S. Sharma, "The density matrix renormalization group in quantum chemistry," Annu. Rev. Phys. Chem. **62**, 465–481 (2011).

[37] N. Nakatani, S. Wouters, D. Van Neck, and G. K.-L. Chan, "Linear response theory for the density matrix renormalization group: Efficient algorithms for strongly correlated excited states," J. Chem. Phys. **140**, 024108 (2014).

[38] X. Yu, D. Pekker, and B. K. Clark, "Finding matrix product state representations of highly excited eigenstates of many-body localized Hamiltonians," Phys. Rev. Lett. **118**, 017201 (2017).

[39] A. Baiardi, C. J. Stein, V. Barone, and M. Reiher, "Optimization of highly excited matrix product states with an application to vibrational spectroscopy," J. Chem. Phys. **150**, 094113 (2019).

[40] J. M. Deutsch, "Eigenstate thermalization hypothesis," Rep. Prog. Phys. **81**, 082001 (2018).

[41] J. M. Deutsch, "Quantum statistical mechanics in a closed system," Phys. Rev. A **43**, 2046–2049 (1991).

[42] M. Srednicki, "Chaos and quantum thermalization," Phys. Rev. E **50**, 888–900 (1994).

[43] Y. O. Nakagawa, M. Watanabe, H. Fujita, and S. Sugiura, "Universality in volume-law entanglement of scrambled pure quantum states," Nature Commun. **9**, 1635 (2018).

[44] S. White, "Spectral function for the S=1 Heisenberg antiferromagnetic chain," Phys. Rev. B **77**, 134437 (2008).

[45] E. Leviatan, F. Pollmann, J. H. Bardarson, D. A. Huse, and E. Altman, "Quantum thermalization dynamics with matrix product states," arXiv , 1702:088942v2 (2017).

[46] R. Nandkishore and D. A. Huse, "Many-body localization and thermalization in quantum system dynamics," Ann. REv. Condens. Matter Phys. **6**, 15–38 (2015).

[47] E. Altman and R. Vosk, "Universal dynamics and renormalization in many-body localized systems," Ann. Rev. Condens. Matter Phys. .

[48] J. H. Bardarson, F. Pollman, and J. E. Moore, "Unbounded growth of entanglement in models of many-body localization," Phys. Rev. Lett. **109**, 017202 (2012).

[49] G. Vidal, "Classical simulation of infinite-size quantum lattice systems in one spatial dimension," Phys. Rev. Lett. **98**, 070201 (2007).

[50] F. Verstraete, D. Porras, and J. Cirac, "Density matrix renormalization group and periodic boundary conditions: A quantum information perspective," Phys. Rev. Lett. **93**, 227205 (2004).

[51] M. Zwolak and G. Vidal, "Mixed-state dynamics in one-dimensional quantum lattice systems: A time-dependent superoperator renormalization algorithm," Phys. Rev. Lett. **93**, 207205 (2004).

[52] F. Verstraete, J. J. García-Ripoll, and J. I. Cirac, "Matrix product density operators: Simulation of finite-temperature and dissipative systems," Phys. Rev. Lett. **93**, 207204 (2004).

[53] F. Verstraete and J. I. Cirac, "Continuous matrix product states for quantum fields," Phys. Rev. Lett. **104**, 190405 (2010).

[54] F. Verstraete and J. I. Cirac, "Renormalization algorithms for quantum many-body systems in two and higher dimensions," arXiv , 0407066 (2004).

[55] F. Verstraete, V. Murg, and J. Cirac, "Matrix product states, projected entangled pair states, and variational renormalization group methods for quantum spin systems," Advances Phys. **57**, 143–224 (2008).